EVALUATION OF BALL MILL PERFORMANCE AND ENERGY CONSUMPTION THROUGH THE DISCRETE ELEMENT METHOD

MATHEW NDETO KYALO

DOCTOR OF PHILOSOPHY IN
MECHANICAL ENGINEERING

JOMO KENYATTA UNIVERSITY
OF
AGRICULTURE AND TECHNOLOGY

2026

Evaluation of Ball Mill Performance and Energy Consumption through the Discrete Element Method

Mathew Ndeto Kyalo

A Thesis Submitted in Partial Fulfillment of the Requirements for the Degree of Doctor of Philosophy in Mechanical Engineering of the Jomo Kenyatta University of Agriculture and Technology

2026

DECLARATION

This thesis is my original work and has not been presented for a degree in any other University

Signature..... Date …….....

Mathew Ndeto Kyalo

This thesis has been submitted for examination with our approval as the University Supervisors

Signature..... Date …….....

Dr. Ing. James Kuria Kimotho, PhD

JKUAT, Kenya

Signature..... Date …….....

Prof. (Eng.) Hiram Muriithi Ndiritu, PhD

JKUAT, Kenya

DEDICATION

To my wife, children, and parents.

ACKNOWLEDGEMENT

I would like to express my sincere gratitude to my supervisors Dr. Ing. James K. Kimotho and Prof. (Eng.) Hiram M. Ndiritu, for their invaluable guidance, mentorship, and outstanding leadership throughout my research journey. The technical team at the JKUAT mechanical engineering workshops provided great assistance, and I extend my special thanks to Mr. Michael Mwai and Mr. Nderi of Foundry workshop for their invaluable support. I also extend my gratitude to Mr. Dadson Mwangi and Amos Kinyunye for their assistance in ore sampling, characterization and grinding. I am also deeply grateful to African Development Bank (AfDB) for awarding me the scholarship that enabled me to study at JKAUT. Additionally, I would like to express my appreciation to Japan International Cooperation Agency (JICA) through AFRICA-ai-JAPAN Project (Year - 2018/2019; iPIC/05/18) for their financial support in fabrication of the experimental ball mill and acquisition of Altair EDEM software. Lastly, I would like to express my heartfelt thanks to my parents and siblings for their unwavering support throughout my academic journey. A special appreciation goes to my wife for her patience and understanding during the entire period of my study. Finally, I would like to acknowledge my children for their unconditional love and unwavering support.

TABLE OF CONTENTS

LIST OF TABLES

LIST OF FIGURES

LIST OF APPENDICES

ACRONYMS AND ABBREVIATIONS

AAS	Atomic Absorption Spectroscopy
ANFO	Ammonium Nitrate/Fuel Oil
ANOVA	Analysis of Variance
API	Application Programming Interface
ASGM	Artisanal And Small-Scale Gold Mining
ASM	Artisanal and Small-Scale Mining
BPM	Bonded Particle Method
CAD	Computer-Aided Design
CCD	Central Composite Design
CFD	Computational Fluid Dynamics
CV	Coefficient of Variation
DEM	Discrete Element Method
DOE	Design of Experiments
EDEM	Event-Driven Execution Model
LSM	Large-Scale Mining
UCM	Unified Comminution Model
PBM	The Population Balance Model
PPL	Plane-Polarized Light
PSD	Particle Size distribution
ROM	Run of Mines
RMSE	Root Mean Square Error
STEP	Standard for the Exchange of Product Data
VFD	Variable Frequency Drive
XPL	Crossed Polarized Light
XRF	X-ray Fluorescence

LIST OF NOTATIONS

$\boldsymbol{a}$	Population Balance Scaling Parameter [s^{-1}]
$\boldsymbol{b_{ij}}$	Population Balance Breakage Function
$\boldsymbol{C}$	Mill Critical Speed [rpm]
$\boldsymbol{C_d}$	Dashpot Damping Coefficient
$\boldsymbol{d}$	Characteristic Top Limit of the Material Size [mm]
$\boldsymbol{d_{b\,max}}$	Maximum Ball Diameter in a Charge [mm]
$\boldsymbol{d_o}$	Particle Overlap [mm]
$\boldsymbol{dt}$	Time Step of the Simulation [s]
$\boldsymbol{D}$	Effective Diameter of the Mill *m])*
$\boldsymbol{e}$	Coefficient of restitution
$\boldsymbol{E}$	Net Specific Energy [J]
$\boldsymbol{F_i(eE)}$	Distribution of Fracture Energies of Particles in Size Class i
$\boldsymbol{f_c}$	Powder Filling (%)
$\boldsymbol{F_i}$	Particle Size Distribution of the Mill Product (%)
$\boldsymbol{G}$	Bulk Modulus [N/m^2]
$\boldsymbol{g}$	Acceleration due to Gravity [m/s^2]
$\boldsymbol{I_i}$	Moment of Inertia [kg/m^2]
$\boldsymbol{J}$	Ball Filling Volume [m^3]
$\boldsymbol{K}$	Contact Stiffness [N/m^3]
$\boldsymbol{K_s}$	Particle Stiffness [N/m^3]
$\boldsymbol{K_1}$	Constant in Theories of Comminution
$\boldsymbol{K_2}$	Empirical Constant linked to Mill Type and Grinding Duty
$\boldsymbol{K_k}$	Kick's constant
$\boldsymbol{K_R}$	Rittinger's constant
$\boldsymbol{m}$	Mass Particle [kg]
$\boldsymbol{m_i(t)}$	Mass Fraction of the Particles [kg]
$\boldsymbol{m^*}$	Effective Mass [kg]

$\boldsymbol{n}$	Exponent Relating Media Size and Mill Size
$\boldsymbol{Ps}$	Particle Size $[mm]$
$\boldsymbol{P(E)}$	Collision Energy $[J]$
$\boldsymbol{p(e)}$	Energy Partition $[J]$
$\boldsymbol{R}$	Average Particle radius $[m]$
$\boldsymbol{R_i}$	A vector running from the centre of the particle to the contact point with its magnitude equal to the particle radius
$\boldsymbol{S_i}$	Population Balance Selection Function $[s^{-1}]$
$\boldsymbol{U}$	Interstitial Filling
$\boldsymbol{V_i}$	Translational velocity $[m^2]$
$\boldsymbol{V_b}$	Volume of Solid Balls $[m^3]$
$\boldsymbol{V_m}$	Mill Volume $[m^3]$
$\boldsymbol{V_p}$	Volume of Solid Powder $[m^3]$
$\boldsymbol{x_i}$	Particle Size in Class i $[mm]$
$\boldsymbol{x_j}$	Feed Material Top size $[mm]$
$\boldsymbol{x_f}$	Material Product Size $[mm]$
$\boldsymbol{x_p}$	Material Feed Size $[mm]$
$\boldsymbol{v_r}$	Relative Velocity of the Particles $[m/s]$

LIST OF GREEK SYMBOLS

$\boldsymbol{\alpha}$	Size Sensitivity Exponent
$\boldsymbol{\beta}$	Shape Exponent
$\boldsymbol{\gamma}$	Steepness Exponent
$\boldsymbol{\varepsilon}$	Bed Porosity of Balls and Powder
$\boldsymbol{\epsilon}$	Coefficient of Restitution
$\boldsymbol{\lambda_i(E)}$	Net Breakage Frequency at Energy $[J]$
$\boldsymbol{\lambda_i^{DEM}(E)}$	DEM Collision Frequency at Energy $[J]$
$\boldsymbol{\lambda_i^{exp}(E)}$	Mean Number of Collisions
$\boldsymbol{\Lambda}$	Curvature Exponent
$\boldsymbol{\mu}$	Optimum Particle Size for Particular Mill Conditions $[mm]$
$\boldsymbol{\mu_r}$	Coefficient of Rolling Friction
$\boldsymbol{\mu_s}$	Coefficient of Static Friction
$\forall$	Charge Shoulder Toe Angle [°]
$\boldsymbol{\rho}$	Particle Density $[j]$
$\boldsymbol{\nu}$	Poisson Ratio
$\boldsymbol{\Phi_j}$	Fine Fraction Parameter
$\boldsymbol{\omega}$	Angular Velocity $[\mathrm{m}/s]$

ABSTRACT

Ball mills are a frequently used technology for comminution in the chemical and mineral processing industries, yet their characteristically low energy efficiency presents a persistent operational challenge; even marginal improvements can yield substantial economic and environmental benefits. This research investigates the relationship between mill geometry, operational parameters, and grinding efficiency by employing an integrated computational and experimental framework. The study compares the performance of two distinct mill designs - polygonal and cylindrical geometries—under varied configurations (with and without lifters). The Discrete Element Method (DEM) was used to simulate particle dynamics, charge motion, and wear, while a Population Balance Model (PBM) was applied to determine ore-specific breakage parameters and predict product size distributions. Simulations were validated against experimental data obtained from a custom-designed milling setup capable of precise speed control and in-line torque monitoring. Key findings from the DEM analysis demonstrate that geometry fundamentally alters charge behavior. At 75% of critical speed, a polygonal mill without lifters increased effective interparticle interactions by 10% and minimized particle centrifuging compared to a lifter-less cylindrical mill. The introduction of lifters further optimized performance: in the polygonal design, lifter addition enhanced collision frequency, resulting in a significant 26% reduction in power draw and a reduced Archard wear rate of $1.18 \times 10^{-3} m$. The cylindrical mill equipped with lifters achieved high collision intensity similar to the polygonal design but exhibited superior operational stability and about 30% lower wear rate. The developed DEM model demonstrated strong predictive capability, achieving a high Pearson correlation coefficient (>0.9) between simulated and experimental results. Predictions showed excellent quantitative agreement with experimental data, with root mean square errors (RMSE) of 2.3 W for power draw and 2.1° for shoulder angle. The grinding kinetics of two ore types, a gold ore and a malachite copper ore (averaging 4.7% Cu), were characterized using the PBM. The specific breakage rate (S_i) for the malachite ore increased with particle size, reaching a maximum of $2.892\ min^{-1}$ at $2\ mm$, a phenomenon attributed to the reduced agglomeration tendency and lower surface energy of larger particles. Breakage distribution functions and the optimum feed size for efficient milling were established. Furthermore, investigations into binary ore blends revealed that overall grindability is non-linear and disproportionately influenced by the harder ore component, potentially leading to a broader product size distribution when ores of differing hardness are combined. The DEM-calibrated parameters and PBM-derived kinetic models generated in this study provide a robust, scalable foundation for the design and optimization of industrial grinding circuits, directly linking particle-scale mechanics to full-circuit performance.

Keywords: Ball mill, Discrete Element Method, Population Balance Model, Milling kinetics.

CHAPTER ONE

INTRODUCTION

1.1 Background

In the ore processing sector, size reduction or comminution is typically performed to enhance the surface area for reactions that liberate valuable minerals from the host (Gottheil, 2021). The size at which liberation occurs usually falls within the range of to 10 microns (Semsari et al., 2020). A typical comminution circuit as shown in

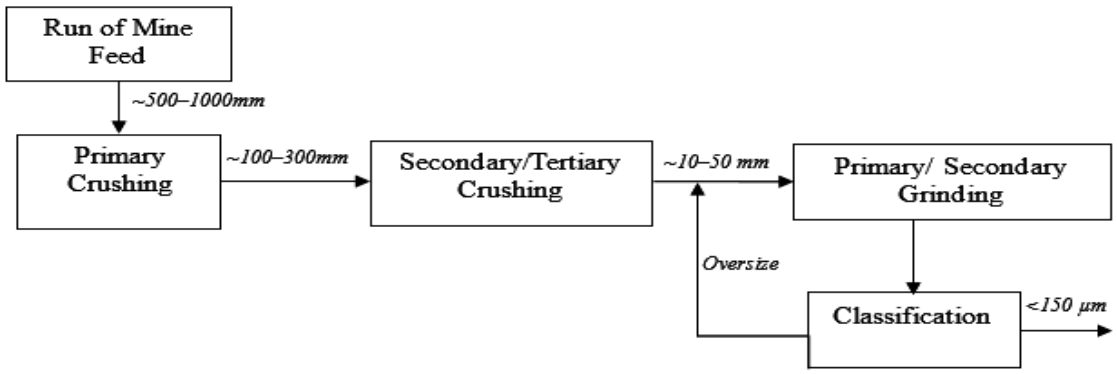

Figure 0.1, consists of crushing and grinding operations. Crushing generally takes place by compressing a rock between two metal plates, like in jaw, gyratory, or cone crushers, or by striking a rock with a metal surface, as it occurs in a hammer mill (Vasilyeva et al., 2023). Primary crushing is commonly done using jaw crushers due to their affordability and energy efficiency. Although a gyratory crusher has a greater capacity per unit area of the grinding surface, it is limited in terms of feed size compared to jaw crushers (Xiao'Ou, 2024). Cone crushers offer certain advantages that make them well-suited for size reduction and shaping in downstream crushing circuits, as they allow for adjustments in feed and discharge openings (Fang et al., 2024). Other types of crushers used in comminution circuits include high-pressure rolling mills. Size reduction through crushing is limited $\sim 20mm$ below which the process becomes uneconomical.

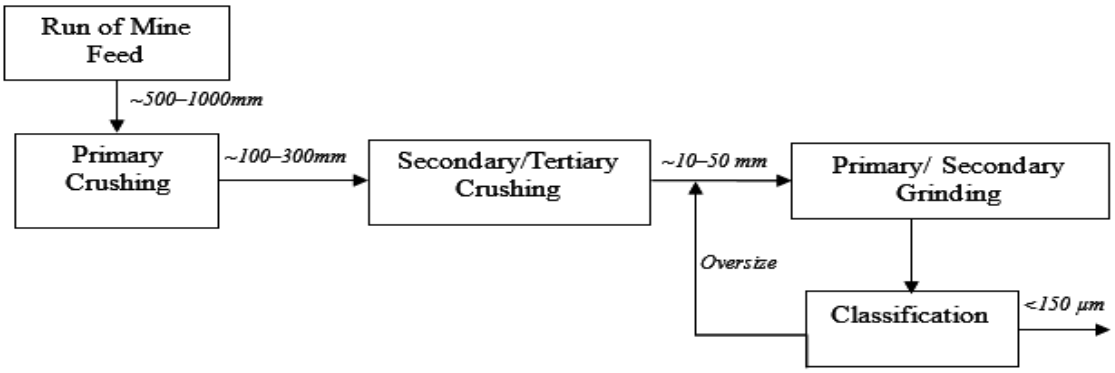

Figure 0.1: A Typical Gold Ore Comminution Circuit

The grinding process becomes necessary when further size reduction, such as below 20 mm, is needed (Pereira et al., 2023). Grinding mills are machines designed for size reduction that typically follow crushers in processes where finer products are required. The primary objective of grinding is to generate fines from mineral fractions by increasing the specific surface area (Tavares, 2007). Grinding involves a pulverizing or powdering process that employs mechanical forces such as impact, compression, shearing, and attrition (Fuerstenau et al., 2003). A diverse array of mills has been created for specific applications. Some mills are capable of grinding a broad range of materials, while others cater to particular grinding needs. Grinding mills are broadly grouped into several major categories, each suited to specific size-reduction needs. Tumbling mills, including ball, rod, and SAG/AG mills, remain the most widely used for general coarse to fine grinding, relying on impact and abrasion within a rotating cylindrical shell (Wills & Finch, 2016). Vertical roller mills (VRMs) provide higher energy efficiency by combining grinding, drying, and classification in a single compact system, making them popular in cement and industrial mineral processing (Kirsch, 2018). High-pressure grinding rolls (HPGR) achieve very high throughput by compressing ore between two counter-rotating rollers (Anticoi et al., 2018). For ultrafine grinding (up to 5 microns) or highly specialized applications, jet mills use high-velocity gas streams to induce particle-on-particle breakage, while attrition or stirred mills employ intense media agitation to produce extremely fine product sizes (Roufail, 2011).

Ball mills are highly adaptable grinding machines in the category of tumbling mills, frequently used in both the chemical and mineral processing industries. These mills are available in various sizes, ranging from compact batch models to large-scale units capable of processing up to 200 tons per hour. Due to their exceptional size reduction efficiency up to 20:1 in open circuits, ball mills remain the preferred choice for grinding operations (Napier-Munn et al., 1999). As the mill rotates, energy is imparted to the charge, creating a complex environment where particles are sized down through impact and attrition. Conventional rotating mills lined with wear-resistant materials integrated with lifters are applied in the industry. In addition to the conventional designs, polygon-shaped mills have been adopted by artisanal and small-scale miners (ASM) due to their potential for local manufacturing at mining sites without the need for heavy industrial machinery. The emergence of polygonal mills has replaced manual methods of ore particle size reduction. The mills encounter challenges such as short operational lifespans due to wear and high-power consumption. Addressing these challenges necessitates a thorough evaluation of operating conditions to optimize efficiency. In the grinding process, achieving fine grinding can be particularly difficult due to the tendency of certain materials to form aggregates or clumps, which can disrupt the grinding efficiency and lead to uneven particle size distribution (Chhabra & Shankar, 2019).

The efficiency of the grinding process is fundamentally influenced by two key factors: the characteristics of the material to be ground and the intensity of the applied load (Tavares, 2022). The characteristics of the material encompass the physical and mineralogical properties including; particle size distribution, hardness, density, moisture content, and breakage resistance. These properties determine how the ore responds to mechanical impacts and abrasive forces inside the mill. On the other hand, the applied intensity, refers to the magnitude and frequency of the mechanical energy delivered to the particles, which is governed by mill speed, liner and lifter geometry, grinding media size and distribution, and the presence or absence of slurry. Higher applied intensity increases collision forces and promotes particle breakage; however, excessive intensity may lead to energy losses through particle cushioning, media wear, or centrifuging (Semsari et al., 2020). The

interplay between material characteristics and applied energy determines the rate of breakage, particle motion regimes, and ultimately the overall energy efficiency of the grinding system. If the force applied does not exceed the elastic limit and the material is compressed, energy is stored within the particle (Tavares, 2022). After a load is lifted, the particle goes back to its initial state without performing any meaningful work. The energy stored in this process turns into heat, leaving the particle unchanged in size. Applying a slightly greater force can cause the particle to break. For efficient energy use, the force should be just above the material's crushing strength. The four main mechanisms of action are: impact, which occurs when a particle hits a single rigid surface; compression, which involves the breakdown of particles between two rigid forces; shear, caused by interactions with fluids or other particles; and attrition, resulting from particles rubbing against one another or a hard surface (Kalman, 2000).

Comminution efficiency can be enhanced through the adoption of new, cost-effective technologies and gradual advancements in technology application (Vasilyeva et al., 2023). Improvements in the operating conditions of comminution equipment aim to optimize processing parameters. This can result in lower operating costs, increased throughput, and enhanced downstream processes due to better particle size results. The energy needed to achieve size reduction relates to the material's internal structure, and the process involves two phases: first, opening any existing small fissures, and second, creating a new surface (Wang et al., 2021). While it's impossible to precisely gauge the energy needed for the size reduction of a specific material, various empirical laws have been introduced over time.

Theories emerged to forecast the association between comminution energy and the resulting particle sizes. The classical laws of comminution, formulated by Rittinger, Kick, and Bond, are known as the three theories of comminution (Austin, 1973). Generally, empirical laws do not factor in the effects of particle shape and size distribution. Moreover, they overlook certain material properties, such as toughness and fracture patterns, and tend to oversimplify energy losses resulting from heat, noise, and mechanical inefficiencies (Rumpf, 1973).

Population balance mode (PBM) has emerged as a second-generation tool for estimating energy needs and particle size reduction in comminution processes (Sogani et al., 2016). In population balance modeling (PBM) of grinding processes, two fundamental parameters govern the comminution dynamics: (1) the specific breakage rate function (S_i) and (2) the breakage distribution function (b_{ij}) or its cumulative form (B_{ij}) (Datta & Rajamani, 2002). The S_i function quantifies the probability of particles in a given size class undergoing fracture per unit time, while the b_{ij} function describes the progeny size distribution resulting from parent particle fragmentation (Lee et al., 2019). Together, these functions provide a mechanistic framework for analyzing particle size reduction kinetics and the underlying breakage phenomena. Once these parameters are determined, they enable simulations for both batch and continuous milling processes. Population balance models necessitate experimental calibration to ensure precise predictions operating under the assumption of uniform breakage behavior, which may not always apply (Gupta, 2022).

An alternative approach to predicting the behavior of granular assemblies is the discrete element method (DEM), which models particle interactions directly rather than relying on population balance formulations. These methods allow researchers to efficiently explore various scenarios at lower costs. The discrete element method (DEM) has emerged as a preferred computational technique for modelling granular materials, as it explicitly simulates the motion, collision, and interaction of individual particles within a granular assembly. This technique treats particles as distinct entities and determines their motion based on Newton's second law of motion, using suitable contact models for interactions between particles and between particles and geometries (Guo & Xia, 2023). It takes into account particle motion, impact forces, and energy dissipation, enabling a detailed examination of grinding efficiency (Gao & Sun, 2003). DEM proves to be an effective tool for comprehending and optimizing ball mills. Although it is computationally intensive, it offers valuable insights into particle interactions, grinding efficiency, and wear patterns, contributing to enhanced mill performance and energy efficiency (AmanNejad & Barani, 2020). Recent advances in DEM, such as improved contact models, GPU-accelerated computation, machine-learning-enhanced calibration, and

coupling with CFD or FEM, have further strengthened its reliability (Doan et al., 2025; Pezo et al., 2025; Toledo M. et al., 2025). Despite these advances, a significant gap remains in accurately linking particle-scale DEM predictions to bulk-scale behavior under realistic industrial conditions. Current DEM models still struggle with high computational cost for large systems, limited accuracy in representing complex particle breakage mechanisms, challenges in calibrating material parameters for non-spherical or cohesive particles, and uncertainties when coupling DEM with continuum methods such as CFD or FEM.

This study first aimed to identify the optimal operating conditions for ball milling using discrete element method (DEM) simulations. The operating parameters considered included mill configuration, power consumption, operational stability, and liner wear. Altair EDEM software, coupled with the Archard wear model, was employed to simulate and evaluate wear behavior across different mill profiles. The optimized operating conditions obtained from the DEM analysis were subsequently used to predict the particle size distribution within the ball mill using a population balance model (PBM). This integrated framework leverages the complementary strengths of DEM and PBM by linking the milling collision energy environment with grinding kinetics. The mineral systems investigated in this study comprised gold and copper ores..

1.2 Problem Statement

The current contribution of the mining sector to the gross domestic product in Kenya is less than 1% (KNBS, 2025). The country aims to increase the share to 10% by the year 2030 by exploiting more minerals and through value addition (Republic of Kenya, 2007). The enactment of a mining and minerals policy outlines a 20-year mining strategy in the sector (Ministry of Mining, 2016). Although large-scale mining (LSM) companies have operations in the country, the Artisanal and Small-Scale Mining (ASM) sector offers more employment, thus having the potential to improve communities' livelihoods (Yager, 2013). A major drawback in the formalization of ASM is technological limitations. Ball mills play a key role in the final particle size reduction of gold and copper ores. There are

approximately 3,000 ball mills used by artisanal and small-scale gold miners in the Western region of Kenya (Barreto et al., 2018). This number has increased due to formalization adoption of technology over the years among the estimated 40,000 ASM in Kenya (Republic of Kenya, 2022b). The common types of ball mills are polygonal-shaped primarily used in dry batch grinding. The polygonal mills have a lifespan of less than one year due to wear and consume relatively large power, which leads to low profits. Studies on the significance of mill shape are not available in the literature, yet polygonal-shaped mills are widely used by ASM. Optimization of ball mill operation would be the center stage of these activities since ores require size reduction. In the minerals industry, it is relevant to understand how mills will respond to blends of ores with different grindability from different parts of the deposit. In gold mining, the metallurgical performance of ore blends is commonly assumed to be additive, i.e. equal to the weighted average of the performances of the constituent ores. In copper ore processing, while extensive research has addressed the grinding of copper sulfide ores, there remains a significant gap in studies concerning the comminution behavior of copper oxide ores, such as malachite, a knowledge gap this thesis aims to address. Although the Discrete Element Method (DEM) has become a powerful and widely used tool for modeling particle motion and interactions in mining operations, its practical application remains limited by high computational demands and the simplified breakage models typically employed. These limitations hinder DEM's ability to fully capture the complex fragmentation behavior observed in real milling systems. As a result, there is a need for a more robust and computationally efficient approach to accurately model particle breakage. Population Balance Models (PBMs) offer a promising alternative, as they can incorporate detailed breakage and selection functions while reducing computational cost. However, the integration of PBM with DEM is still underdeveloped, despite its potential to optimize milling performance, minimize energy consumption, and reduce losses associated with excessive production of ultrafines. Therefore, a research gap exists in integrating DEM data to PBM framework capable of capturing realistic breakage behavior.

1.3 Research Objectives

The main objective of this research is to investigate the effect of mill design and process parameters on mill performance and energy consumption. The main objective will be achieved through the following specific objectives;

1. To develop and validate a simulation model of the ball milling process using the discrete method.
2. To evaluate and compare the performance of cylindrical and polygonal ball mills under varying operating and design conditions based on DEM simulations.
3. To apply the milling conditions to obtain particle breakage parameters for copper and gold ores.

1.4 Justification of Study

Ball mills are widely used and have a very low energy efficiency, as much of the energy is dissipated as heat and sound (Tavares & de Carvalho, 2009). A modest improvement of their energy efficiency can lead to significant economic and environmental benefits. Although a ball mill is a simple piece of equipment, a wide range of breakage mechanisms occur in the mill, making the processes very challenging to understand and model. Understanding the processing conditions will lead to reduced liner wear, minimizing replacement costs and lost production. The wear experienced in a ball mill represents a significant operating expense. In the past, it has been challenging to understand the exact processes occurring inside a grinding mill during its operation. The implementation of 3D discrete element modeling (DEM) simulations, along with wear-progression models, allows for highly precise predictions regarding the performance of a lining. By calibrating the wear model in DEM with wear-monitoring data, the design of the liner can be optimized even further. Producing a certain particle size and distribution for a given ore will lead to increased downstream recoveries. The characteristics of these ores are dependent on the geological formation of a certain area. More so, the ore body characteristics vary due to varied weathering environments. A comprehensive

understanding of particle breakage in the milling process is quite essential to attain optimal size reduction and equipment selection. The ball milling data will be used for simulation and optimization purposes, which will lead to reduced energy consumption and improved productivity. General information on the milling characteristics of gold and copper ores will also be provided. The mineralogical characteristics of ores influence their breakage behavior and the subsequent separation and extraction processes of the minerals. Thus, it is essential to identify the physical and chemical properties of gangue minerals that could compromise the quality of the final product. This research will address part of the technological gap between small-scale miners and large-scale miners in the processing of gold and copper ores. The grinding kinetics data can be used in the development of a pilot plant comprising all the processes of liberation of copper from malachite ore. The adoption of improved ball milling technologies has the potential to significantly enhance the ore processing capabilities of artisanal and small-scale miners. By increasing the efficiency of comminution, these advancements can lead to better resource utilization, higher recovery rates, and greater value addition, ultimately contributing to increased production output and improved economic returns for small-scale operations.

1.5 Outline of Thesis

This thesis is organized into five chapters. Chapter One provides the background of the research, focusing on particle size reduction through crushing and grinding. It outlines the problem statement, justifies the significance of the research, and states the objectives of the study. Chapter Two provides an in-depth literature review, outlining the classical laws of comminution, the population balance model (PBM), and the discrete element method (DEM). It also critically examines prior research to identify inconsistencies and gaps that require further investigation. Chapter Three details the materials and methods used in this study, including a description of the experimental setup, the calibration procedure for the DEM simulations, and the approaches taken for ore characterization and grinding tests. Chapter Four presents the results and discussions of numerical simulations, experimental tests, parameter identification, model application and validation. Additionally, the results of batch grinding tests are discussed. Finally, Chapter Five

summarizes the conclusions drawn from the research findings and offers recommendations for future work. Supplementary information is provided in the appendices.

CHAPTER TWO

LITERATURE REVIEW

2.1 Overview

In this section, an overview of ball milling as applied in mineral processing is introduced, followed by theories of comminution, population balance models, and the methods used for the estimation of power draw in ball milling. The Discrete Element Method (DEM) is discussed as a numerical approach for modeling the mechanical behavior of individual particles, which move independently and interact through contact forces. Finally, the occurrence of copper ores and gold ores used in grinding tests is discussed.

2.2 Theory of Ball Milling

Ball milling is widely applied in the mineral and chemical processing industries. In mineral processing, ore is reduced to the required size to liberate valuable Impact and abrasion cause the formation of a large number of fine particles. Ball consume more than 30% of the total energy in a comminution circuit (Jeswiet & 2016). Typical specific energy consumption of a ball mill for mineral liberation to size <75 µm is 20–40 kWh/t (Shabana, 2010). Manufacturers of ball mills desire to achieve high mineral recovery at low cost (Vasilyeva et al., 2023). To achieve this, the main focus is usually on energy consumption and product size (Chimwani, 2014). grinding results in low mineral recovery, while over-grinding leads to unnecessary consumption (Panjipour & Barani, 2018). The processing conditions are highly on the particular plant. Based on operation, ball mills can be categorized into batch grinding and continuous grinding (Mill & Panicles, 2016). In batch production, the grinding material is loaded and retained inside the mill for the appropriate time to

energy-efficient size reduction and then unloaded.

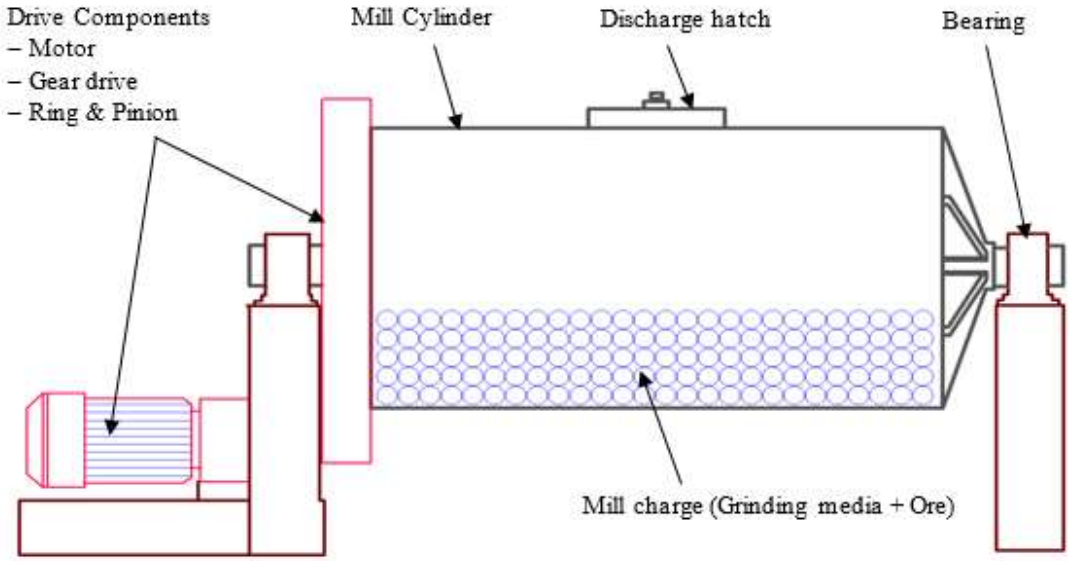

Figure 0.1 illustrates a representation of a batch ball mill, commonly used in industrial applications. The ball mill charge refers to the contents inside a ball mill, specifically, the grinding media, the material being milled, and any other additive used to enhance milling. Batch ball mills are suitable for small-scale production or processing of high-value materials like medical powders. Batch ball mills have been used widely in the optimization of milling since their parameters can be controlled realistically, and the output results can be upscaled for the design of large mills. This type of mill has been used almost entirely by artisanal and small-scale gold miners in the processing of gold ore.

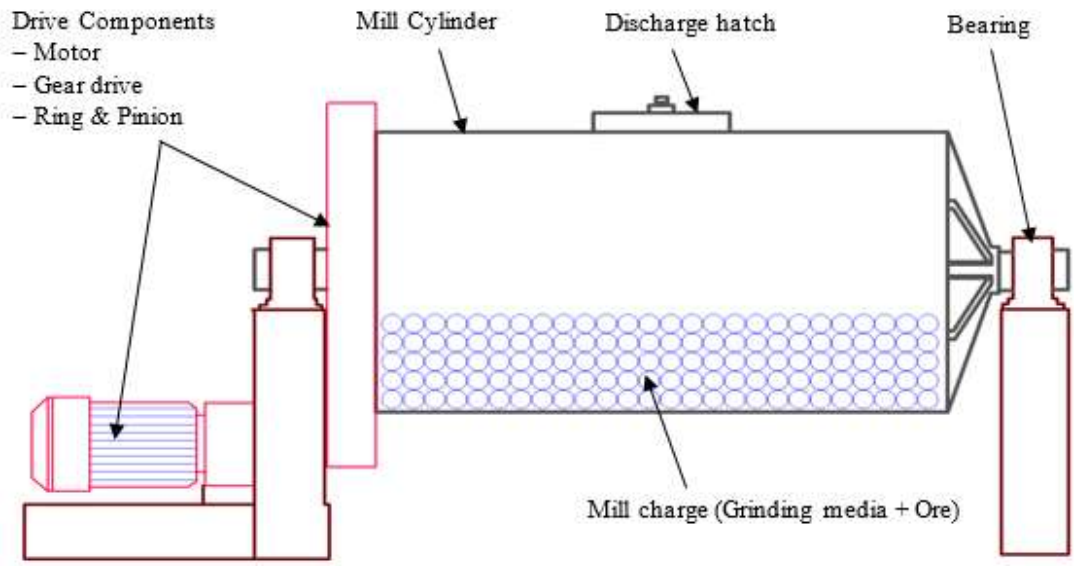

Figure 0.1: Schematic Representation of a Batch Grinding Ball Mill

In continuous grinding shown in Figure 0.2, the ore is fed continuously, and ground material is removed. The output size distribution is dependent on the residence time under set conditions. The flow of ground particles is enhanced through a continuous supply of a liquid, like water or air. In ore concentration plants, continuous mills can be overflow-type or grate-type. The overflow-type mills have an exit hole at the trunnion, which is larger than the inlet hole, providing a hydraulic gradient for the overflow. The grate discharge type has an inbuilt grate and slurry lifters at the discharge end.

The performance of a mill is influenced by various operational parameters, such as its rotational speed, load, the amount of grinding media, the size distribution of that media, and characteristics of the feed being ground (Foszcz et al., 2018). A major technological challenge in the grinding process involves selecting the appropriate type and size of both the mill and the grinding media. This selection is essential for achieving optimal efficiency throughout the grinding phase, the classification circuit, and the regrinding of the processed feed properties.

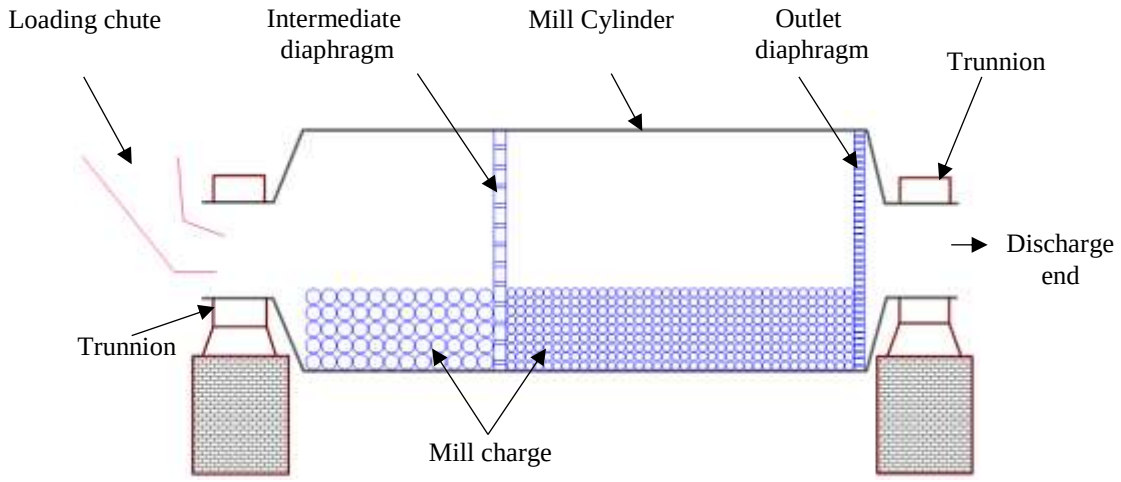

Figure 0.2: Schematic Representation of a Continuous Grinding Ball Mill

2.2.1 Grinding Media

Grinding media in a ball mill are the elements responsible for crushing or grinding particles inside the mill through impact and attrition, and their selection critically affects mill performance. The media can be classified based on the type of material (for instance; forged steel, high-chrome steel, ceramic) or by manufacturing process, which directly influences hardness, wear resistance, and energy transfer characteristics (Matsanga et al., 2023).The ball diameter has a strong influence on mill throughput, energy consumption, and product size distribution. Larger balls deliver greater impact energy and are generally more effective at breaking coarse feed particles, whereas smaller balls produce finer particles due to increased contact surface area and attrition forces. Optimal media selection must balance these competing factors: enough energy to break the largest ore fragments while maintaining sufficient surface area for fine grinding (Matsanga et al., 2023). An empirical formula general form has been proposed by (Magdalinovic et al., 2012), and all fit into the given equation **Error! Reference source not found.**,

$$d_{b\,max} = K_2 d^n, \qquad (0\text{-}1)$$

where $d_{b\,max}$ is the maximum ball diameter in a charge, d is the characteristic top limit of the material size which is being ground, K_2 is an empirical constant linked to the mill type and grinding duty, and n is an exponent describing how media size scales with mill size. This relation highlights the dependence of media size on ore characteristics and mill operating conditions. Recent experimental and modelling work confirms these principles. For example, (Tomach, 2024) demonstrated that grinding media diameter significantly affects grinding efficiency, with finer media enhancing particle size reduction in vibratory ball mills, indicating the continued relevance of media selection to modern milling design. In ball mill operations, top size grinding media specifically refers to the largest ball diameter used in the charge. This dimension is a key operational parameter because it determines the maximum impact energy available to break the coarsest particles in the feed. Larger top-sized balls are effective for coarse grinding but can reduce grinding efficiency for finer product sizes due to fewer grinding contacts and higher energy consumption per impact (Hirosawa & Iwasaki, 2021). Therefore, selection of the top ball size involves balancing the initial breakage requirements of the ore with the target product fineness and overall energy efficiency, and it is typically defined alongside the ball size distribution within the mill charge. Studies also show that media size distribution (graded media) strongly affects milling performance: mixing different ball sizes can increase grinding rates and reduce energy consumption compared to single-size media, especially when optimized via grinding dynamics and modeling approaches such as DEM (Yu et al., 2025). The shape of grinding media remains an area of active research. Cylindrical media such as cylpebs can show different breakage behaviour compared to spherical balls, potentially enhancing selective breakage of larger particles while reducing over-grinding of fines, although detailed mechanisms are still being explored. As particle size decreases, grinding efficiency tends to fall due to increasing specific surface area requirements. Mechanistic studies continue to refine fundamental grinding laws (e.g., through energy-balance formulations), improving predictions of energy requirements at very fine sizes beyond classical models like Rittinger's Law (Martelli & Di Nunzio, 2025). In practice, the combined use of graded media sizes, informed by both empirical relationships and numerical optimization (e.g., DEM and grinding kinetics), offers a more

effective strategy for achieving desired product sizes while controlling energy consumption and wear.

2.2.2 Charge Motion

When a mill is in operation, the grinding media and the material to be ground are lifted along the side of the mill (Wills & Finch, 2006). The force balance on a particle against the wall is given by outward Centrifugal force (F_c) and gravitational force (F_g) (King, 2001) as shown in equations (0-2)and (0-3),

$$F_c = m\omega^2 \frac{D}{2}, \tag{0-2}$$

$$F_g = mg, \tag{0-3}$$

where ω is the angular velocity, m is the mass of any particle (media or charge) in the mill, D is the effective diameter of the mill and g is the acceleration due to gravity. The particle will remain against the wall if these two forces are in balance according to equation 2.4,

$$F_c = F_g \cos\forall. \tag{0-4}$$

where ∀ is shown diagrammatically in Figure 0.3. The particle will fall from the wall at the time when the $cos\forall$ satisfies Equation (0-5) ;

$$cos\forall = \frac{F_c}{F_g} \tag{0-5}$$

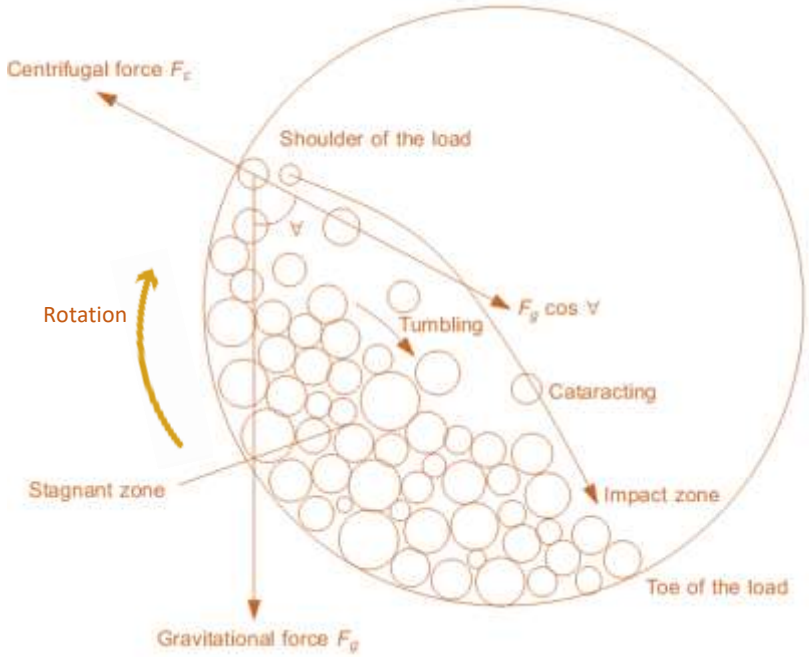

Figure 0.3: Typical Ball Mill Charge Motion

The critical speed of the mill is defined as the speed at which a single ball will remain against the wall for a full cycle. The critical speed is usually calculated using equation (0-6),

$$C = \frac{42.3}{D^{1/2}} revs/min \tag{0-6}$$

where C is the critical speed in rpm, and D is the diameter of the mill in meters. (Morrell, 1993) used a photographic technique in measurement of the charge shape and velocity. The charge motion inside a ball mill refers to the movement of grinding media (balls) and material as the mill rotates. Understanding charge motion is crucial for optimizing grinding efficiency, power consumption, and wear rates. This motion is influenced by several factors, including mill speed, filling ratio, liner design, and media size. Charge motion can be categorized into three types: cascading, cataracting, and centrifuging (Boemer & Ponthot, 2017b). Cascading motion occurs at low to medium speeds, typically between 50-65% of critical speed. In this motion, particles roll down the surface of the

charge, leading to breakage through abrasion and attrition, which is suitable for fine grinding. Cataracting motion takes place at higher speeds, ranging from 65-85% of critical speed. This motion is characterized by impact forces and is more effective for coarse grinding. The speed range should be controlled such that the cataracting streams fall on the toe of the charge, transferring energy to the grinding material. If the media falls on the liners, energy is wasted, and it can aggravate liner wear. Centrifuging motion occurs at very high speeds (≥85% of critical speed), where media adheres to the mill shell due to centrifugal force. In this case, no grinding occurs, making it inefficient and, therefore, it should be avoided. Recent studies using DEM and high-speed imaging confirm these patterns and provide detailed insights into particle trajectories, energy distribution, and optimal media-liner interactions, enabling better mill performance and reduced wear (Caibin & Kuangdi, 2023; Pural & Boylu, 2025).

2.2.3 Mill Charge

The mill charge is represented as a percentage of the total geometric volume, including the void spaces within the stationary grinding media, compared to the overall available volume of the mill . When the mill is operating at critical speed, the grinding media charge is generally 40–50% of the effective mill volume. A high charge volume of 50% gives the maximum possible surface length and maximizes the cascading surface. Proper material feed is also crucial for effective milling operations. The feed size for a ball mill is influenced by both the machine's specifications and the characteristics of the material being processed. Generally, the optimal feed size is less than 20 mm, although some larger ball mills can handle feed sizes of up to 50 mm. This parameter is crucial, as it impacts the grinding efficiency; smaller particles typically facilitate easier grinding and yield a finer end product, whereas larger particles may prolong the grinding time and lead to a coarser output. Furthermore, if the material feed rate is insufficient, the ball mill may operate below its optimal capacity, resulting in ineffective grinding and unnecessary energy consumption (Kanda et al., 1999). An inadequate volume of material can cause the grinding media to interact predominantly among themselves, leading to increased wear and reduced grinding efficiency. Conversely, an excessive volume of material can hinder

efficient grinding by creating a cushioning layer that dampens the impacts between the grinding media. Studies on powder filling ratio recommend an interstitial filling ratio, U in the range 0.6 to 1.1 (Cayirli, 2018). Mill charge behavior strongly influences grinding performance, yet classical descriptions of cascading, cataracting, and centrifuging oversimplify what is in reality a highly dynamic and heterogeneous system. Traditional models based on critical speed and force balance provide useful thresholds but fail to capture the evolving interactions among media, liners, slurry, and ore, all of which change with wear, feed variability, and operating conditions. Empirical rules for media size and charge optimization often lack general applicability, leading to suboptimal energy use and inconsistent size reduction in practice (Morrell, 1996). Although modern DEM simulations and emerging sensor technologies have improved the understanding of collision energies and charge trajectories, these tools still face limitations related to computational cost, model assumptions, and scarce real-time validation in industrial mills (Caibin & Kuangdi, 2023). Overall, mill charge behavior remains complex, and effective optimization requires integrating empirical knowledge with advanced modeling and in-situ monitoring.

2.2.4 Liners and Lifters

Liners and lifters are fundamental to grinding-mill performance because they structural protection and functional control over charge dynamics. Liners shield the shell from abrasive and impact forces while also transmitting rotational motion to

grinding media and ore.

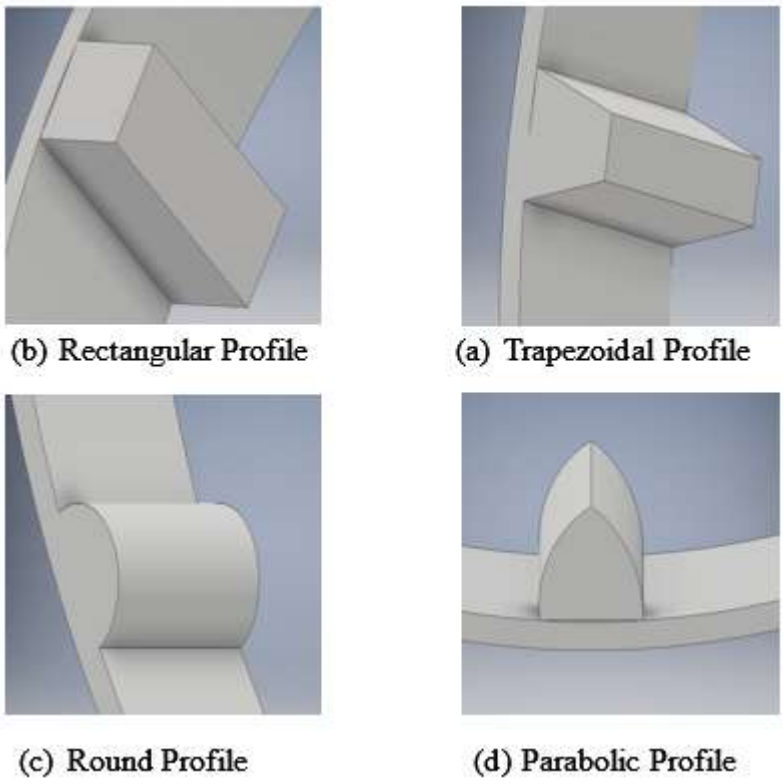

Figure 0.4 shows typical lifters integrated with liners used in industrial applications. The profile and arrangement of lifters are crucial in mill design; when lifters are positioned closely together relative to the size of the grinding media, balls are elevated to greater heights, thereby promoting cataracting motion. When liner geometry is poorly designed, wear accelerates, leading to unplanned downtime, reduced mill availability, and increased operating costs. Recent research continues to emphasize that liner configuration—particularly shape, lifting profile, and material significantly affects load trajectory, energy dissipation, and breakage (Chimwani & Bwalya, 2020; Kimani et al., 2024). The growing application of digital tools such as 3D scanning and custom-engineered liner assemblies shows notable improvements in wear life and throughput, underscoring the economic benefits of optimized liner systems (Mei et al., 2025).

The role of lifters is closely intertwined with liner performance because lifters generate the cascading and cataracting actions necessary for efficient grinding. Their geometry height, spacing, face angle, and profile control media trajectory and the height to which the charge is lifted. DEM-based studies report that inappropriate lifter design increases particle slip, reduces impact energy, and lowers grinding performance (Yin, Ma, et al., 2024). Conversely, optimized lifter profiles improve charge transport, stabilize the shoulder and toe positions, and enhance energy utilization while moderating power draw (Chimwani & Bwalya, 2020)These improvements are particularly important in modern high-capacity mills, where marginal gains in charge motion translate into substantial energy and wear-cost savings.

The importance of careful liner–lifter design is further validated by recent numerical and industrial assessments. DEM simulations have become indispensable for evaluating liner wear, lifter–particle interactions, and local impact forces, allowing designers to tailor face angles and profile shapes to site-specific ore characteristics (Boemer & Ponthot, 2017a); updated through (Kimani et al., 2024). Industrial trials confirm that well-engineered liner–lifter combinations increase service life, reduce unscheduled stoppages, and support more stable milling conditions. As shown across recent optimization and industrial case studies, targeted improvements to liner–lifter geometry remain among the most effective approaches for enhancing throughput, reducing energy consumption, and improving overall mill reliability. The entrapment of media between lifters can reduce the effective diameter of the drum due to the presence of the trapped media. Industrial experiments on the influence of lifters on mill performance have revealed that increased lifespan of liners yields great economic advantages (Toor et al., 2013). In contrast, liners engineered for durability tend to increase the mill's weight and decrease its volume when made from the same material. In empirical analysis methods, the effects of liners and lifters are often overlooked. However, Discrete Element Method (DEM) approaches have proven valuable in the design of liner wear and lifters (Boemer & Ponthot, 2017c; Cleary & Owen, 2019; Moys, 1993; Muhayimana et al., 2018).

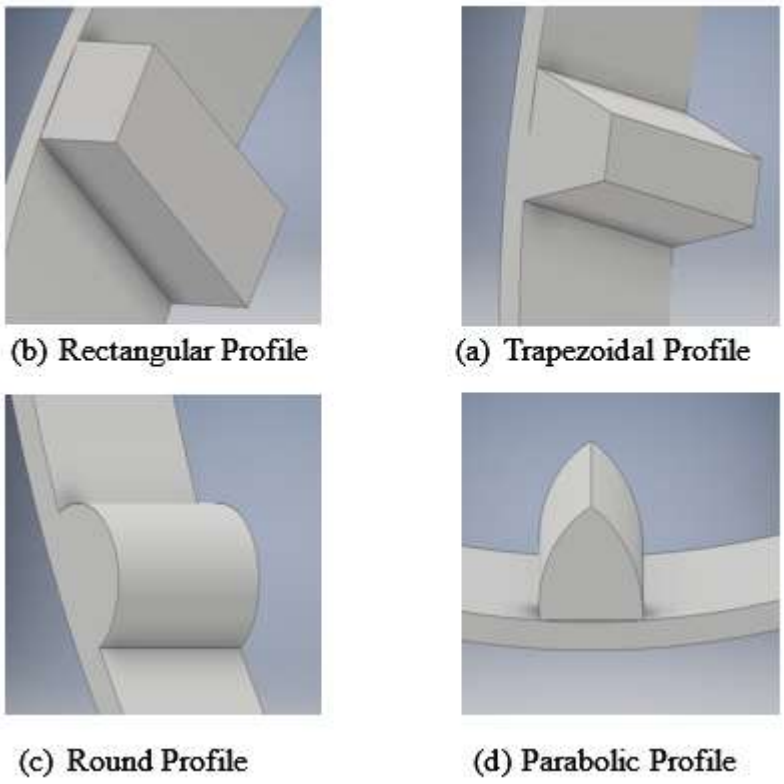

Figure 0.4: Industrial Lifter Profiles Integrated with Liners

By employing DEM, it is possible to make informed decisions regarding lifter shape, face angle, and the number of rows necessary to achieve optimal mill performance. (Rajamani et al., 2000) investigated four distinct lifter profiles: semi-circular, triangular, trapezoidal, and rectangular. Their findings indicated that the rectangular profile incurred the highest power consumption. Furthermore, (Muhayimana et al., 2018; Yin, Li, et al., 2018) explored the effect of the lifter profile using DEM, revealing that the lifter modifications and optimization lead to reduced particle slip.

2.3 Theories of Comminution

Over the years, theories have been developed to predict the relationship between comminution energy and the resulting output sizes. Each law relies on different assumptions and applies to varying ranges of particle sizes. Classical laws of comminution

proposed by Rittinger, Kick, and Bond are referred to as the three theories of comminution (Austin, 1973). Rittinger developed an inverse proportion relationship between the energy required to produce new surface area as shown in equation (0-7) (Austin, 1973),

$$E = K_R \left(\frac{1}{x_p} - \frac{1}{x_f} \right) \tag{0-7}$$

where E is the net-specific energy, x_p and x_f are the feed and product sizes respectively, K_R is Rittinger's constant dependent on material. Rittinger's Law posits that the energy necessary for size reduction is directly proportional to the increase in surface area (Hukki, 1962). Kick's Law of comminution is based on the assumption that the energy required for size reduction is primarily used to reduce the volume of the material rather than to generate new surface area. This law is most applicable to coarse crushing processes, where changes in surface area are relatively small. It states that the energy required to reduce a material's size by a given proportion is constant, regardless of the initial size of the material. Mathematically, Kick's law is expressed by (Austin, 1973), as shown in equation (0-8).

$$E = K_k \ln \left(\frac{x_f}{x_p} \right) \tag{0-8}$$

where E is the net-specific energy, x_p and x_f are the feed and product sizes, respectively, and K_k is Kick's constant. Kick's Law asserts that the energy for size reduction correlates with the logarithm of the ratio between initial and final particle sizes (Hukki, 1962). This law assumes that the crushing force remains constant and is related to the number of particles created rather than the new surface area generated. It is most relevant to coarse crushing and suggests that the energy required is connected to the number of new particles formed.

The third law of grinding was proposed by (Bond, 1962), based on extensive experimental investigations, and states the effective work done in crushing and grinding results

primarily in the formation of crack tips, and it is directly proportional to the total crack length formed. In equidimensional particles, the total crack length is said to be equivalent to the square root of one-half the surface area of the particle. The total work input represented by the given weight of a crushed or ground product is, therefore, inversely proportional to the square root of the diameter of the particles of the product. The specific energy is expressed by (Bond, 1962) in equation (0-9),

$$E = K_4 \left(\frac{1}{\sqrt{x_p}} - \frac{1}{\sqrt{x_f}} \right) \tag{0-9}$$

where, E is the net-specific energy, x_p and x_f are the feed and product sizes respectively, and K_4 is a constant for a given material and mill. This method has been used widely in industries for evaluating the grindability of materials and estimation of power requirements for industrial mills. Bonds empirical equations are based on the determination of the power required to grind the ore from the given feed size to a specific product size, and the selection of the grinding circuit with the mill design that will draw the required power. None of the three laws of comminution apply to all particle ranges of crushing and grinding (Jankovic et al., 2010). In the review, it was found that Kick's equation was applicable for crushing, Rittinger's equation may be used for finer grinding and Bond's equation is applicable in the conventional milling range A general form of the three theories was later developed and expressed by (Jankovic et al., 2010) in equation (0-10) ,

$$dE = -C \frac{dx}{x^n} \tag{0-10}$$

where, E is the net specific energy; x is the characteristic dimension of the product; n is the exponent; and C is a constant related to the material. If exponent n in the above equation is replaced by numerical values; 2, 1 and 1.5, the integrated form of the general equation leads to the fundamental theories represented by the law of Rittinger, Kick and Bond respectively. The above theories of comminution were developed from empirical

relations do not account for the complex particle breakage environment and hence are very limited in prediction capabilities. Population balance models have over time been developed to explain particle breakage in ball mills with greater success.

2.4 Population Balance in Ball Mills

The population balance model (PBM) is a theoretical framework based on the probability that particles of a given size will break into a defined distribution of smaller fragments. It operates under first-order kinetics and is governed by two primary functions: the specific rate of breakage, S_i, and the breakage distribution function, b_{ij} (Austin et al., 1975; Sogani et al., 2016). The S_i, quantifies the proportion of particles in size class 'i' that undergo breakage per unit time during milling. The b_{ij} describes how the broken fragments from size class 'j'are distributed among smaller size classes. That means that any given b_{ij} is the mass fraction of material j that goes into the size class i after the operation of the breakage. These two functions are used to construct the material balance for each particle size class, which can be mathematically represented by equation (0-11):

$$\frac{dm_i(t)}{dt} = -S_i m_i(t) + \sum_{\substack{j=1 \\ i<j}}^{i-1} b_{i,j} S_j \, m_j(t) \qquad (0\text{-}11)$$

where $m_i(t)$ is the mass fraction of the particles of component i, S_i is the specific rate of breakage, b_{ij} is the rate at which particles of the ground component i, become particles of component j, and t is the grinding time. Additionally, $i = 1$ in equation (0-11), for it is often the case that the decrease rate of the largest particle group is shown by the first order equation (0-12)

$$\frac{dm_i(t)}{dt} = -S_1 m_1(t) \qquad (0\text{-}12)$$

where S_1 is a specific rate of breakage of size 1 material and $m_1(t)$ is the fraction by weight of the material of size 1 at time t. If S_1 is constant with time, then the equation can be written in the form of equation (0-13) (Austin, 1973),

$$Log[m_1(t)] = Log[m_1(0)] - \frac{S_1.t}{2.303} \tag{0-13}$$

This equation is stated as the first-order kinetics of grinding. If S_1 is constant with time, it can be determined from the slope of $[m_1(t)]/m_1(0)$ versus time on a semi-log plot. In most instances, when breakage occurs in a ball mill, the breakage of materials with a single feed size fraction usually fits first-order kinetics, and the specific rate of breakage can be calculated through the slope of a semi-log plot. Deviation from the first-order kinetics has been found by (Barani & Balochi, 2016) to be influenced by material characteristics and increased grinding time. During long grinding times, fines can cushion further breakage of particles, resulting in deviation from first-order kinetics (Petrakis et al., 2017). Another reason could be that the size of the material is much bigger than the grinding ball diameter, such that coarse particles cannot be nipped by the balls, and some of the material behaves as a relatively weaker material, while some other material behaves as a relatively stronger material (Barani & Balochi, 2016). In milling kinetics, the specific rate of breakage is given as equation (0-14),

$$S_i = \frac{\mathrm{a}x_i^{\alpha}}{1 + \left(\frac{x_i}{\mu}\right)^{\Lambda}} \tag{0-14}$$

where S_i is the specific rate of breakage, a parameter depending on milling conditions and denotes the particle size when the correction factor is 0.5, x_i is the upper size of the class i in mm, Λ is a positive number that depends on the material type and shows how rapidly the rates of breakage decrease as size increases. These parameters are obtained from a log-log graph of specific breakage against particle size. When the material of size *j* breaks once, the mass fraction of the broken products with size i can be represented by the

breakage function $b_{i,j}, i > j$ and the breakage function is usually represented in cumulative form $b_{i,j}$ as equation (0-15) (Petrakis et al., 2017),

$$B_{i,j} = \sum_{k=n}^{i} b_{k,j} \tag{0-15}$$

where $b_{k,j} = b_{i,j} - b_{i+1,j}$.

According (Austin & Bhatia, 1972), for short grinding cycles $B_{i,j}$ can be estimated from size the analysis of products as using a narrow size *j* fraction as initial feed as equation (0-16),

$$B_{i,j} = \frac{log[(1 - P_i(0))/(1 - P_i(t))]}{\log[(1 - p_{j+1}(0))/(1 - p_{j+1}(t))]} \tag{0-16}$$

where $p_i(t)$ is the mass fraction less than x_i size at time t. Another method of representing the cumulative particle breakage, $B_{i,j}$ is by using the following empirical form by (Yakup et al., 2014) in equation(0-17) ,

$$B_{i,j} = \Phi_j \left(\frac{x_{i-1}}{x_j}\right) + \left(1 - \Phi_j\right).\left(\frac{x_{i-1}}{x_j}\right)^{\beta^{\gamma}} \tag{0-17}$$

where: x_j is the top size, Φ_j , γ and β are model parameters that depend on the properties of the materials. The population balance model is a logical approach which assumes a constant distribution function. The experimental estimation of particle size-distribution is very laborious to generate hence back calculation is used to generate directly an appropriate set of parameters to predict the desired size spectrum (Das, 2001). Back-calculation of the selection and breakage function parameters for grinding involves the minimization of error between the predicted and experimental distributions (Yuan et al., 2023). Using predicted initial values from short-cycle batch experiments, the empirical

form can be used to predict particle distributions. Estimation of the model parameters S_i and b_{ij} is a prerequisite for carrying out process simulation and scale-up design work.

2.5 Milling Mechanistic Models of Breakage Mechanisms

A mechanistic model of comminution considers fundamental theories of modelling ore particle breakage. Whereas population balance models do not decouple the contributions of the machines, the mechanistic models require information on the ore breakage in an independent form (Magalhães, 2013). The first comprehensive mechanistic approach used to explain the breakage mechanisms in comminution was proposed and later modified by (King, 2001) in equation **(**0-18**)**,

$$S_i = \int_0^\infty P(E) m_i^*(E) \int_0^1 F_i(eE) p(e) de dE \qquad \textbf{(}0\text{-}18\textbf{)}$$

where $P(E)$ is the distribution of collision energies, $p(e)$ is the energy partition amongst particles within the bed, $F_i(eE)$ is the distribution of fracture energies of particles in size class i, and $m_i^*(E)$ is the mass of particles captured in an impact of magnitude E. The model was able to qualitatively describe the results of batch grinding experiments, but fell short in describing properly how the particle population evolves during grinding (Tavares, 2017). This model among other similar initial models, pioneered by researchers, were limited by indirect observations and uncertain back-calculated parameters.

The introduction of the Discrete Element Method (DEM) revolutionized the field by enabling detailed simulation of particle kinematics and collision energies. The mechanistic models that used DEM, require a description of how the energy is split among the particles positioned on the bed, which is not known in the model (Magalhães De Carvalho, 2013). A Unified Comminution Model (UCM) was proposed by ref (Powell, 2006), aimed to provide a framework for all comminution device machines. This model used DEM data to describe the mechanical environment, which is then coupled with a population balance framework that describes the different basic modes of breakage.

Computational fluid dynamics (CFD), Smoothed-particle hydrodynamics (SPH), and other tools can be used to characterize the influence of slurry in wet conditions. The population balance structure of the UCM for a given particle class, ij is expressed by (Powell et al., 2008) in equation (0-19) ,

$$\frac{dM_i}{dt} = -\left[\sum_{d=1}^{N} \lambda_i(E_d)M_i - \sum_{r=1}^{S} \lambda_i(E_r)M_i\right] + \sum_{j=1}^{i-1}\left[\sum_{d=1}^{N} \lambda_j(E_d)M_j(E_d)b_{ij}(E_d) + \sum_{r=1}^{S} \lambda_j(E_r)M_j(E_r)b_{ij}(E_r)\right] \quad (0\text{-}19)$$

where $\lambda_i(E)$is the net breakage frequency at energy E for the size class i, given by;

$$\lambda_i(E) = \lambda_i^{DEM}(E)/\lambda_i^{exp}(E), \quad (0\text{-}20)$$

where, $\lambda_i^{DEM}(E)$ is the DEM collision frequency at energy E for size class i and $\lambda_i^{exp}(E)$ is the mean number of collisions required to break particles in size class i with collision energy E. N and S are, respectively, the number of normal and shear energy bins and M_i is the mass of material contained in size i in the mill. The possible breakage modes are described in

.

Table 0.1: Mechanistic Breakage Modes

Breakage mode	Description	Application of DEM + PBM
Impact breakage	Particle shatters on high-energy collision	High-energy collisions in DEM $S_i(E)$) > 0 , fines in PBM
Chipping	Small fragments broken from edges	Low-energy, repeated collisions, small shifts in $b_{i,j}$
Abrasion / attrition	Surface worn down by sliding contacts	Many low-energy contacts ,small incremental decrease in M_i, small fines in PBM
Compression	Particle crushed between balls or liner surfaces	Contact forces in DEM , energy computed mapped to $S_i(E)$ and $b_{i,j}$
Fragmentation	Large particles break into smaller fragments that themselves break	PBM naturally handles cascade: fragments from parent class become new parents in smaller classes

The UCM model was able to differentiate modes of particle breakage, however, it had some limitations. The major shortcoming was the lack of information on distributing the energy between colliding media, the excess energy input power not accounted for in particle damage and the description of breakage of the sub-DEM material (Tavares, 2017).

A Virtual Comminution Machine (VCM) model was developed to facilitate the design of new comminution machines and further improvement of existing comminution devices. This model also includes a framework to deal with different size reduction processes, and improved coupling DEM and SPH compared to UCM model. Other additional features include the provision of a model to describe rounding by means of parameterized super-quadric particles and fines generation by attrition. It also describes weakening by repeated impacts. A more advanced mechanistic modeling approach has been developed, which integrates Discrete Element Method (DEM) data to characterize the mechanical environment within size reduction equipment. This approach involves coupling DEM output with empirical or semi-empirical models that describe various particle breakage mechanisms (Weerasekara et al., 2013). The resulting framework captures how sub-DEM-scale particles interact, how they are confined within particle beds, and how collision

energy is distributed among them. Such models provide a more detailed understanding of breakage processes under realistic milling conditions. The rate of change in the mass of material within a specific size class was expressed by (Tavares, 2017) in equation (0-21) :

$$\frac{dw_i}{dt} = \frac{\omega}{H}\left\{-w_i \int_0^\infty m_i^*(E)p(E)\int_0^1 \left[1 - b_{ij}(eE)\right] F_i(eE,t)p(e)dedE + \sum_{j=1}^{i-1} w_j \int_0^\infty m_j^*(E)p(E)\int_0^1 b_{ij}(eE)F_j(eE,t)p(e)dedE - D_{i,s}(t) + A_{i,s}(t)\right\}, \quad (0\text{-}21)$$

where H represents the ore charge in the mill, w_i is the mass fraction of particles contained in size class i in the mill at the time t, ω is the frequency of stressing events, $p(E)$ is the distribution of stressing energies E in the mill, $m_i^*(E)$ is the mass fraction of particles in size class $\boldsymbol{i}$ at time t, while $p(E)$ is the probability density function of collision energies E occurring within the mill. $b_{ij}(eE)$ is the body breakage function in density form, dependent on stressing energy. $A_{i,s}$ and $D_{i,s}$ describe the appearance and disappearance of particles in class i due to surface breakage processes, such as abrasion or chipping. The product eE is the fraction of the collision energy that is absorbed by each particle captured in an impact event.

The existing models still have significant limitations. These include the reliance on simplified particle shapes in DEM, the need for empirically fitted breakage functions in PBM, high computational costs for realistic multi-scale simulations, and a lack of comprehensive industrial validation. Consequently, while these models are powerful tools for optimization and comparison, creating a fully predictive, universal, and physics-based model remains an ongoing research challenge.

2.6 Discrete Element Method

The discrete element method (DEM) is a numerical method used to describe the mechanical behavior of distinct particles that displace independently of one another and interact at contacts. The method is a cycle that progresses with the loss of contacts and creation of new ones. The original concept was developed by (Cundall & Strack, 1979) where the behavior of soil particles was modeled under dynamic loading conditions.

Newton's second law of motion is solved with appropriate contact relationships to describe grinding media in terms of position, velocity, and forces of interaction over time (Tavares, 2017). The DEM method was first applied in 2D modelling of a ball mill by (Mishra & Rajamani, 1992). Due to limitations in computing capabilities, grinding media were modelled as 2D discs. This method could predict the power draw of the mill, the distribution of collision forces inside the mill, and the effects of lifters in a mill. Since that time, this method has been improved, extending the concept to 3D applications with improvements in algorithms and particle models (Bharadwaj, 2014). A major limitation of discrete element modeling is the high computational demands associated with modeling the large number of particles that exist in a system (O 'sullivan, 2008).

The common methods of discrete element particle modelling are soft particle and hard particle (O 'sullivan, 2008). The soft particle model is capable of handling multi-particle contacts, which is important in the simulation of quasi-static systems. On the other hand, the hard sphere modeling processes an instantaneous sequence of collisions, one at a time, and forces in particles are not explicitly defined (Zhu et al., 2007). The soft particle method has been used extensively in describing particle contacts, and individual entities are allowed to overlap (Boemer & Ponthot, 2017b). Collisional interaction of particles with each other and the environment are modeled using contact laws.

The Discrete Element Method (DEM) has revolutionized the analysis of ball mills by enabling the virtual study of granular flows that are difficult to observe in practice. Since its introduction, DEM has progressed from simple 2D models to complex 3D simulations that predict critical operational metrics like charge motion, power draw, and liner wear (Mishra, 2003). Its primary strength lies in providing unparalleled mechanistic insight into mill internals, allowing researchers and engineers to explore design and operational changes such as lifter geometry or ball size distribution in a controlled, virtual environment before physical implementation.

Despite its transformative role, DEM faces significant and persistent limitations that constrain its predictive accuracy. A major critique is the reliance on oversimplified model

physics, most notably the use of spherical particles, which fails to capture the angularity of real ore and its effect on flow and breakage (Yin, Jin, et al., 2024). Furthermore, validation remains a critical challenge; matching only the total power draw is an insufficient single-point check that can mask inaccuracies in internal particle dynamics. The method also suffers from the scale-detail dilemma, where computational constraints force a trade-off between simulating a realistic number of particles and capturing the complex, first-principles physics of breakage and slurry interactions, often resulting in a reliance on empirical sub-models.

Consequently, DEM currently serves best as a powerful tool for comparative analysis and optimization rather than for ab initio prediction of entirely new milling systems (Hu et al., 2024). Its future on bridging key gaps includes developing efficient non-spherical particle models, creating standardized validation protocols with richer industrial data, and better integrating fundamental breakage and slurry physics through multi-scale, hybrid modelling approaches. Until these advancements mature, DEM will remain an indispensable but carefully applied tool for deriving insight and guiding design, rather than offering fully standalone predictive solutions.

2.6.1 Governing Laws and Time Step

Newton's laws of motion form the foundation for modeling particle dynamics in the Discrete Element Method (DEM), linking the motion of particles to the forces acting upon them. In a typical DEM simulation, the user first defines the system geometry, including particle positions, boundary conditions, and contact model parameters. The governing equations for the translational and rotational motion of an individual particle i, with mass m_i and moment of inertia I_i, are expressed by (Jayasundara et al., 2014) in equations (0-22)and (0-23) ;

$$m_i \frac{d\boldsymbol{V}_i}{dt} = \sum \left(\boldsymbol{F}_{ij}^{n} + \boldsymbol{F}_{ij}^{s} + m_i \boldsymbol{g} \right) \tag{0-22}$$

and

$$I_i \frac{d\boldsymbol{\omega_i}}{dt} = \sum \left(\boldsymbol{R}_i \times \boldsymbol{F}_{ij}^{s} - \mu_r R_i \left| \boldsymbol{F}_{ij}^{n} \right| \widehat{\boldsymbol{\omega}}_i \right) \tag{0-23}$$

where V_i, $\boldsymbol{\omega_i}$ and I_i are, the translational velocity, angular velocity and moment of inertia of the particle, respectively, while $\widehat{\boldsymbol{\omega}}_{\boldsymbol{i}}$ represents a unit vector equal to ω_i divided by its magnitude. $\boldsymbol{R_i}$ is a vector running from the center of the particle to the contact point with its magnitude equal to particle radius R_i $\boldsymbol{F}_{ij}^{n}$ and $\boldsymbol{F}_{ij}^{s}$ represent, respectively, the normal contact force and the tangential contact force imposed on particle i by particle j and $m_i g$ is the gravitational force. In Equation (0-23), the first term on the right-hand side represents the torque due to tangential forces, while the second term accounts for rolling resistance torque arising from the normal force. The stability and accuracy of DEM simulations are highly dependent on the selected time step (Δt). An excessively small time step leads to unnecessarily long simulation times, while an overly large time step can cause numerical instability. Two common methods are used to estimate the critical time-step Δt_{crit} (Burns & Hanley, 2017). The first approach calculates Δt_{crit} as a function of mass, m and stiffness, K, typically considering each degree of freedom as a system of uncoupled point masses, as shown by (Cundall & Strack, 1979) in equation (0-24),

$$t_{crit} = 2\pi \sqrt{\frac{m}{K}} \tag{0-24}$$

where m and K are the mass of the smallest particle in the model and contact stiffness respectively. The second approach uses the Rayleigh criterion, based on the idea that energy cannot propagate from a particle beyond its immediate neighboring particles in a single time step.

2.6.2 Contact Search and Contact Models

In DEM simulations, contact search is used to determine which surfaces are in contact and the type of contact. Irrespective of the shape of particles involved, simulation of n interacting particles involves $n(n-1)/2$ pairs of contacts search problem (Mishra, 2003). Contact search alone is known to consume a large fraction of the calculation time

(Abbaspour-fard, 2000). In the DEM literature, particles are bounded by cells or boxes with dimensions equal to the maximum particle diameter. If the corners of a circumscribing square of a particle have an entry into a cell, the particle is regarded to be a member of that cell. These members are used to generate a list of particles with the potential to contact a given particle.

In contact detection for spherical particles within DEM simulations, grid-based search algorithms are commonly employed to identify potential interactions by locating candidate particles within a defined zone surrounding a target particle. For more complex particle representations, such as multi-sphere particles, a two-level grid search method was introduced by (Fang et al., 2015). In this approach, the first-level search identifies potential contacts using the bounding spheres of multi-sphere particles, while the second-level search refines this by evaluating interactions among the individual element spheres that comprise each particle.

Various contact force models have been developed to describe inter-particle and particle-boundary interactions, accommodating different particle shapes, frictional behaviours, and surface adhesion effects. In the context of ball milling simulations, commonly adopted models include the linear spring-dashpot, Hertz, Hertz-Mindlin, and Johnson–Kendall–Roberts (JKR) models (Barthel, 2008; Di Renzo & Di Maio, 2004). The selection of an appropriate model depends on several factors, including particle geometry, the desired level of physical realism, simulation objectives, and the required accuracy. These models differ in their treatment of normal and tangential forces, elastic and plastic deformation, and adhesive interactions, and are chosen accordingly to best represent the mechanics of the milling environment. The Hertz model is used, to describe the contact between two elastic spheres under compression. In that case, an effective Young's modulus takes into account the elastic properties of both bodies and can be defined as: The Hertz model is largely used to measure mechanical properties of materials, but to obtain reliable values of elasticity is important to carefully evaluate if the assumptions described above are valid. The Johnson-Kendall-Roberts (JKR) contact model is an extension of the well-known Hertz contact model. The model accounts for attraction forces due to van der Waals effects.

The Hertz-Mindlin (no-slip) model is widely recognized for its precision and efficiency in calculating forces between interacting particles (Adams & Nosonovsky, 2000).

The main components of the Hertz-Mindlin model are normal force modeled using Hertzian contact and tangential force modeled using Mindlin-Deresiewicz model. The repulsive force in the normal direction is derived from Hertz's theory for the elastic contact of two curved surfaces. It is non-linear and depends on the overlap that captures how the contact area grows during compression. A viscous damping term is added to this to model kinetic energy loss during collision. The force in the tangential direction is based on the work of Mindlin (Johnson, 1985). It models the incremental, history-dependent shear between two spheres with friction. Unlike a simple Coulomb slider, it accounts for micro-slip, a region of partial slip at the edge of the contact circle, even before full macroscopic sliding occurs. The tangential force builds up proportionally to the tangential displacement, at which point full sliding begins. As illustrated in Figure 0.5, this contact model provides a framework for determining forces that arise from particle interactions in both vertical (normal) and horizontal (tangential) directions. Rolling resistance is modeled using a torque that resists the relative rolling of particles, for simulating highly non-spherical or cohesive grains. Damping force is included to achieve a realistic dynamic behavior and energy dissipation.

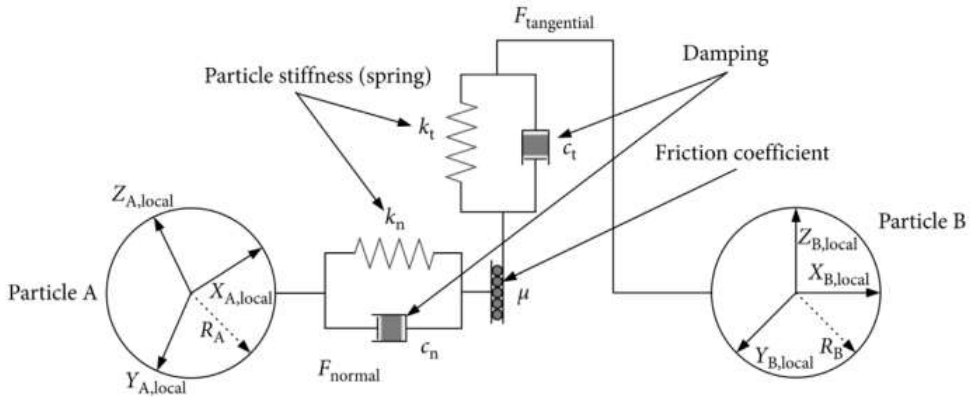

Figure 0.5: The Hertz-Mindlin Contact Model

Applying Newton's second law allows for the computation of acceleration, which is then integrated twice to find the updated positions of each particle. With these new locations established, the model recalculates the contact forces, and this iterative process continues at each discrete time step (Gilardi & Sharf, 2002). In the Hertz-Mindlin framework, the normal force is derived from Hertzian contact theory, while the tangential force stems from the research conducted by Mindlin and Deresiewicz (Mindlin & Deresiewicz, 1953). The normal force (F_n) and tangential force (F_t) are calculated using equations (0-25) and (0-26) respectively,

$$F_n = K_n d_n + C_n v_n \tag{0-25}$$

$$F_t = min\left\{\mu F_{n,} K_t \int v_t dt + C_t v_t\right\} \tag{0-26}$$

Where K_s particle stiffness (N/m), d particle overlap (mm), C dashpot damping coefficient, v relative velocity of the particles (m/s), dt Time step of the simulation (s), e is the coefficient of restitution, $m*$ Effective (equivalent) mass (kg), μ_f coefficient of friction. The damping coefficient for the normal force is approximated based on the coefficient of restitution, which reflects the energy lost during collisions, as shown by (Cummins et al., 2012) in equation (0-27) .

$$C_n = -2Ine\frac{\sqrt{C_n m^*}}{\sqrt{(Ine)^2 + \pi^2}} \tag{0-27}$$

The equivalent mass m^* is shown in equation (0-28) ,

$$m^* = \left(\frac{1}{m_1} + \frac{1}{m_2}\right)^{-1} \tag{0-28}$$

where m is the mass of particle. Each particle experiences a force that is the combination of the normal and tangential contact forces. A Discrete Element Method (DEM) simulation code is employed to evaluate the torque arm, with the resulting torque calculated by integrating the contributions from all particle contacts over time (Di Maio

& Di Renzo, 2005). This approach ensures a detailed and accurate representation of particle dynamics and their influence on torque throughout the simulation.

2.6.3 Modelling Particles in DEM

The Discrete Element Method (DEM) has traditionally modeled granular materials using simple shapes like spheres or disks. Sphere-sphere contact mechanics is the most extensively studied contact model (Govender et al., 2001). These particle shapes can be implemented without difficulties and are efficient in speed of contact detection, which results in faster code development and lower computational time (Podlozhnyuk et al., 2017). However, this ideal shape representation fails to accurately model most phenomena exhibited by real granular materials since most particles are complex in shape (Bharadwaj, 2014). There are three main methods of defining particle irregularities in DEM simulation, namely, polyhedra, super-quadrics, and multi-spheres as shown in Figure 0.6. Polyhedrons are defined in terms of corners, edges, and faces and can be used to represent complex flat-faced particles accurately. Conversely, they require massive computational power to detect contact and compute the coordinates of each corner and face during collision detection. Super-quadrics particles are defined by (O 'sullivan, 2008) in equation (0-29),

$$\left(\frac{x}{a}\right)^{r} + \left(\frac{y}{b}\right)^{s} + \left(\frac{z}{c}\right)^{t} = 1 \qquad (0\text{-}29)$$

where r, s , and t are positive real numbers that determine the main features of the super quadric; a, b and c are scaling factors. The nonlinear equation describing superquadratic requires high computation power. There are no well-defined contact detection methods for such shapes. In the multi-sphere method, particles are represented by overlapping or contacting spheres. The method is based on the Constructive Solid Geometry technique for the construction of complex solids by combining primitive shapes (Abbaspour-fard, 2000). This method approximates particle irregularities while maintaining the accuracy of spheres in fast contact detection and evaluation of the contact forces. Regardless of the

shapes of particles represented by multi-sphere, contact force is calculated between pairs of spheres except that translation and rotation of element spheres are calculated concerning the motion of the whole particle. The choice of the number of element spheres, termed as "sphere density," depends on the application and the desired approximation to actual particle shape (Abbaspour-fard, 2000). If the density of points on the surface of the particle is too high, for instance, clumps composed of thousands of spheres would hardly be usable in a DEM simulation as it would require unreasonable calculation time (Ferellec & McDowell, 2008).

(a) Polyhedra (b) Super-Quadrics (c) Multi-Spheres

Figure 0.6: Particle Shapes in DEM

Recently, advancements in imaging techniques such as laser scanning and X-Ray technologies have allowed for more accurate representations of real particle morphologies (Tolomeo & McDowell, 2022). The major drawback is the requirement of high computational power that makes it infeasible for a large number of particles.

2.6.4 Modelling of Wear Using DEM

In a ball mill, wear occurs through two primary mechanisms: impact collision wear caused by normal forces and abrasion wear resulting from shear forces generated by the sliding motion of the grinding media (Boemer & Ponthot, 2017c). Abrasion directly removes metal from the media surface, while impact wear involves surface damage such as spalling, pitting, flaking, or breakage due to ore-metal contact (Matsanga et al., 2023). In wet grinding, corrosion wear also contributes to material degradation through chemical reactions between the equipment and the corrosive environment. Research indicates that abrasion is the leading cause of metal loss in grinding processes, responsible for 50-70%

of total wear (Amadi et al., 2024). Abrasive wear plays a significant role in various applications where granular material particles slide against equipment surfaces (Radziszewski & Tarasiewiczb, 1993).

The Archard wear model is utilized for DEM modeling of abrasive wear. This model estimates the amount of material removed due to abrasion based on normal contact force and sliding distance, requiring only a single input parameter – an empirical wear constant. The resulting wear depth on CAD geometry mesh elements is calculated. This enables the modeling of geometric deformation resulting from abrasion. The outputs in EDEM are presented as wear depth on geometry mesh elements, facilitating the incorporation of wear-induced deformation into the simulations. According to the Archard model, the wear volume of the geometry is described using equation (0-30),

$$V = K\frac{NL}{H} \tag{0-30}$$

where V is the wear volume of the plane, N is the normal load, K is the wear coefficient, L is the sliding distance, and H is the hardness of the material being ground. In EDEM, K/H is represented by a wear constant W. Hence, the wear volume of geometry is expressed as follows as equation (0-31):

$$V = WNL \tag{0-31}$$

The wear coefficient W can be regarded as the sum of all wear factors, including hardness H, except normal load N, and sliding distance L. The hardness plays a major role in determining the wear coefficient. In the EDEM, the wear depth is used to characterize wear volume according to equation (0-32),

$$h = \frac{V}{A} \tag{0-32}$$

where A is the removed area of material.

2.6.5 Occurrence of Gold Ore

Gold ore is found in the Migori gold belt that starts from near Lake Victoria and extends to the East of Lolgorien with a span of about 4.8 km and a length of about 80 km (Shackleton, 1946). In this region, gold mineralization is reported to occur within banded iron formations, tuffaceous rocks, and most commonly in steeply dipping, strike-parallel quartz veins often associated with steeply dipping strike-slip faults (Mitchell et al., 2020). Exploration in Kenya, particularly Shanta Gold's West Kenya Project, has revealed high-grade gold deposits estimated at 14.05 million tonnes at 1.56 g/t, or about 705,000 ounces(Caracal, 2022) , highlighting the country's significant undeveloped gold potential. Artisanal and small-scale gold mining (ASGM) contributes an estimated 5–6.9 tonnes annually, valued at around USD 250 million, and supports approximately 40,000 miners and 800,000 dependents (Republic of Kenya, 2022a). Production is largely informal, with local trading limiting the economic benefits to miners and leaving much output unrecorded. Industrial-scale mining remains limited, with declared production in 2024 at only 358.5 kg (KNBS, 2025). This suggests that actual gold flows, including informal exports, are considerably higher.

Artisanal and small-scale miners obtain two main types of gold ores: alluvial and hard rock. Hard rock mining involves underground operations that typically feature open pits, where the overburden is manually removed by the miners (Kyalo et al., 2015). Other methods include narrow, vertical, or inclined shafts and adits for accessing the ore body. Processing is done in centres serving at least two ore bodies mined concurrently for small-scale miners and can go as far as different mines under one process plant in the case of large-scale miners. Primary liberation methods incorporate gravity units to recover coarse gold. The recovery of fine gold from tailings is carried out through leaching with cyanide. One of the main challenges in processing centers is obtaining ore of different characteristics requiring blending. Ore blending can lead to high grades, reduce comminution energy, and enhance equipment longevity (Liu et al., 2021). Researchers have addressed ore blending, often revealing that particle breakage does not obey the general rule of mixtures (Tavares & Kallemback, 2013; Van Tonder et al., 2010; Yan &

Eaton, 1994). The complexity of identifying the grindability data of the products based on each ore component is a major limitation in the studies (Tavares & Kallemback, 2013).

2.6.6 Occurrence of Copper Ore

Copper metal is used in vast areas of industry and technology due to its special properties, such as high thermal and electrical conductivity, high ductility, and corrosion resistance (International Copper Study Group, 2016). Society's plans for a decarbonized world will rely on renewable energy and transport electrification, which are copper-intensive sectors (Singer, 2017). Copper annual demand is projected to reach 36.6 million tons by 2031, compared to the current demand of about 25 million tons (Scott Crooks, Jonathan Lindley, Dawid Lipus, Richard Sellschop, Eugéne Smit, 2023). To meet the increasing demand for copper, efforts to explore and extract various copper ores need to be extended. Copper mining activities will struggle to meet this growing demand as discovery rates of new copper deposits are lagging, and the number of operating mines is declining (Noaparast et al., 2012). Copper is extracted from various minerals such as chalcopyrite, bornite, chalcocite, cuprite, malachite, and azurite (Singer, 2017). The copper-bearing minerals can be further classified into oxides or sulfides. The primary mineral chalcopyrite contains copper up to 34% by weight (Jena et al., 2022). The existing deposits of primary copper sulfide ore have continued to decline over the years. The increasing demand for copper will require alternative ore sources like malachite. Copper ore occurs at various locations in Kenya. In Macalder and Kitere located in western region, sulfide copper deposits with grades in the range of 3-4.6 percent have been identified (Sanders, 2007). The occurrence of copper has been reported in the Voi Hills and Maungu, with mineralization reaching up to 8.2 percent (Saggerson, 1958). Other studies in Tharaka Nithi have reported chalcoprite assaying in the range of 1.8-8.4% (Saggerson, 1958). Malachite copper in the range of 3-8% has been identified in Kanzugo area in Kitui area within ingenious rocks (Kugeria, 2020). In the Kazungo area, malachite ore mineralization occurs at disseminated localities striking from southwest to northeast (Sanders, 2007). Another area near Kanzungo is Mithikwani in Matinyani with similar mineralization.

Malachite [$Cu_2CO_3(OH)_2$] is formed by the weathering of primary copper minerals such as chalcopyrite and bornite copper deposits (Haldar, 2017). It can be identified by its distinct green color, monoclinic crystal system with perfect cleavage and penetration twinning (Haldar, 2020). Petrographic studies are used in the identification of malachite. Malachite, like other minerals, behaves differently under different light conditions, making it diminish under one light condition, say PPL (plane-polarized light), and become visible under another, say XPL (crossed-polarized light). Having both XPL and PPL images, therefore, maximizes the chances of identification of mineral crystals forming a rock sample. Processing of malachite ore starts by comminution, involving crushing and grinding to increase the surface area of the ore for further processing. After comminution, malachite ore is usually processed through a hydrometallurgical method consisting of leaching, solvent extraction, and electrolysis (Hocking, 2005). Particle size and distribution are among the most important parameters that affect the leaching of copper. The processes of comminution consume about 50% of the mine site energy (Jeswiet & Szekeres, 2016). Therefore, it requires optimization to avoid energy wastage or to avoid producing more fine particles that are not suitable for downstream processes (Ebadnejad, 2016). Kenya is gaining recognition as a prospective base metals destination. Early-stage prospects have been located in regions like Meru, Kitui, and along the Archean Craton, with surface samples showing high copper grades. Mineralization is often linked to rift-related intrusives and metamorphic belts. Although large-scale mining is not yet operational, artisanal activities confirm deposit viability. Rising global copper demand, especially for electrification and renewables, is spurring investment interest. The mining industry is nascent, as evidenced by 2023 exports of roughly 8,122 tonnes of copper ores and concentrates, primarily to China (KNBS, 2025). Despite regulatory complexities and the need for further development, exploration and investor activity are increasing, indicating considerable latent potential.

2.7 Summary of Research Gaps

The identified research gaps from the literature review can be summarized as follows:

i. Accurately predicting particle breakage in ball mills remains a major challenge in DEM simulations, particularly due to the complex behavior associated with the generation and accumulation of fine particles during the milling process.

ii. Existing phenomenological and empirical models used to analyze ball milling processes often neglect the influence of internal mill components, such as liners and lifters. This omission limits the accuracy of these models in capturing the true dynamics of charge motion and energy transfer within the mill.

iii. A significant research gap exists due to the limited capability of current DEM simulation tools to model large-scale particle systems typical of ball milling processes. This limitation, driven by both software constraints and computational resource demands, restricts the ability to perform high-fidelity simulations necessary for accurately capturing complex particle interactions in realistic milling environments.

iv. While the Discrete Element Method (DEM) has been effectively applied to enhance the understanding, design, and optimization of ball mills, limited research has been conducted on polygonal-shaped mills, which are commonly used by artisanal and small-scale miners. This gap highlights the need for further investigation into the performance and behavior of such mill geometries under varying operating conditions.

v. There is a general lack of publicly available scientific information on ore comminution, largely due to the reluctance of processing industries to share detailed data and methodologies, often driven by competitive and proprietary concerns. This hinders knowledge advancement and model validation in the field.

This research will address all the gaps mentioned above.

CHAPTER THREE

METHODOLOGY

3.1 Background

This section outlines the methods and materials used to assess the impact of ball milling process parameters on energy consumption and liner wear. It describes the test rig and operating conditions used for calibrating and validating the simulation results. Additionally, it details the simulation setup and boundary conditions used in the discrete element method (DEM). Finally, the procedures for determining the breakage parameters of copper and gold ores are presented. Gold ore and copper ores are selected due to their availability and liberation particle size that require milling.

3.2 Sizing of the Experimental Rig

The experimental ball mill rig was designed to incorporate a coupling for interchanging mills.

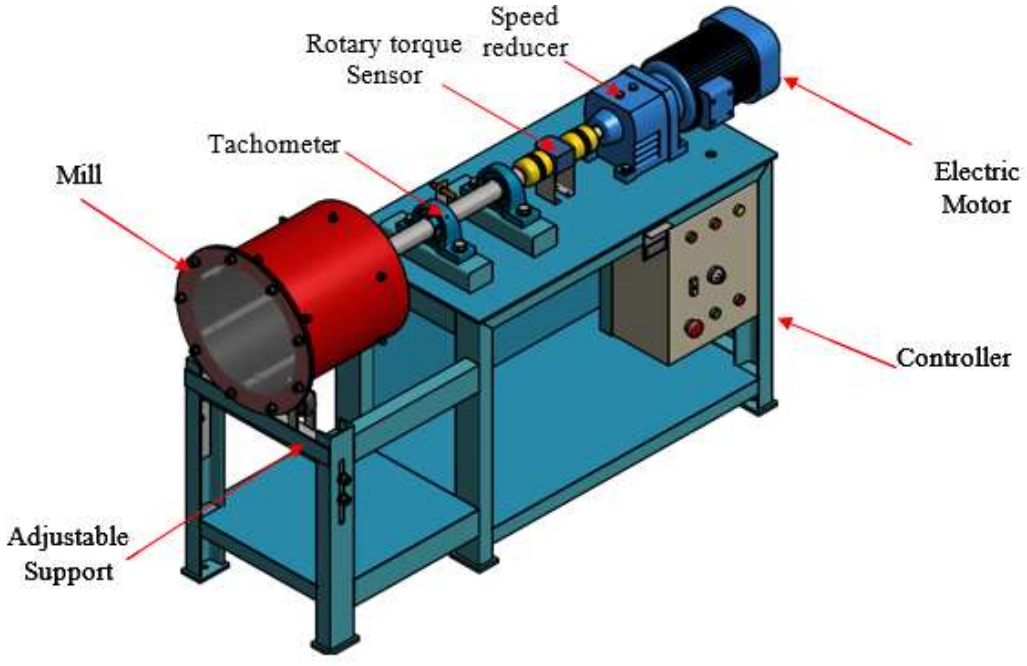

Figure 0.1 shows a pictorial view of the rig that includes the mill, drive system, instrumentation, as well as an adjustable drum support. To enable a valid comparison with the standard FC Bond ball mill test, the mill used in this study was constructed with comparable volume and diameter dimensions.

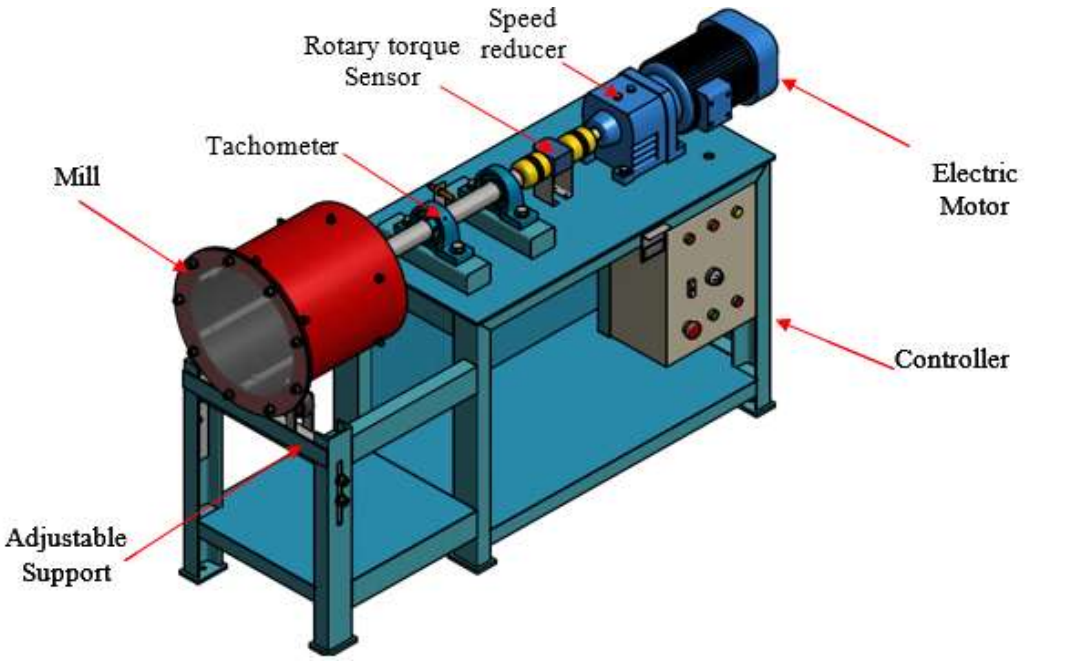

Figure 0.1: Laboratory Experimental Rig

The main dimensions of the mill drum are shown in Figure 0.2. The effective internal diameter and length of the cylindrical drum were 350 mm and 354 mm, respectively. Hence, the available internal volume of the drum was obtained as $V_d = 0.0325\ m^3$. A total of 6 rectangular lifters were fitted in the drum, each having a length, width, and height of 354 mm, 20 mm, and 10 mm, respectively.

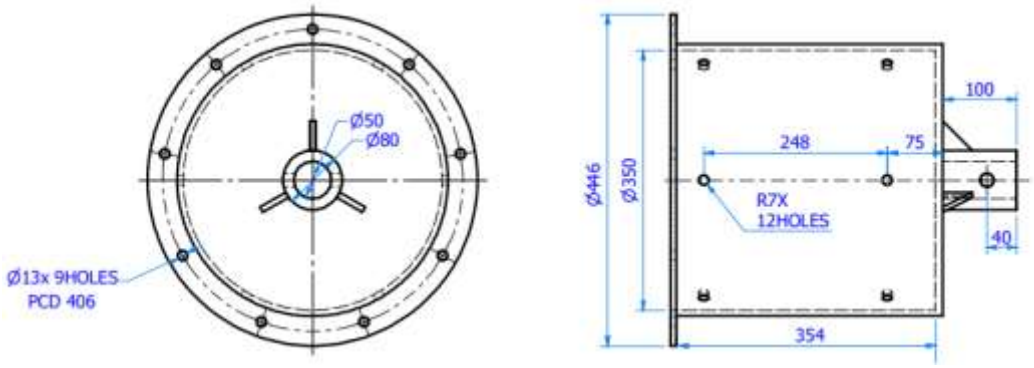

Figure 0.2: Major Dimensions of Cylindrical Mill Drum

In ball milling, the maximum volume occupied by grinding media is normally 50% of the effective volume. For a closely packed equisized ball charge, 26% void is used. For optimal output, balls of varying sizes are typically used, meaning the maximum volume occupied by the balls will be approximately 50% or half of the effective volume. The maximum weight of the grinding media at 50% fill volume was $M_g = 71.73\ kg$. Ore normally fills the spaces between the grinding media up to 10-15% above the grinding media (balls). During operation, a maximum charge of 30% of the drum's effective volume is allowable. For this study, the density (ρ_c) of gold-bearing quartz material was standardized at $2260\ kg/m^3$. Based on this value, calculations determined a maximum ore charge mass (M_c) of $21.76\ kg$.for the drum configuration. The total mass of the empty drum, M_d obtained from CAD design was 43.44 kg. The total mass of the drum, grinding media, and charge was obtained as $M_t = 136.93\ kg$. For a tumbling mill, the torque is primarily due to the weight of the charge acting at a certain lever arm (the effective center of mass of the charge from the mill's center).

The torque required to tumble the media was calculated based on the torque-arm method (M. S. Powell & McBride, 2004) as shown in (0-1):

$$T = MgR_{com}Sin(\theta_{com}) \qquad (0\text{-}1)$$

where T denotes the Torque in Nm, m denotes the charge mass , g denotes acceleration due to gravity, R_{com} is the radius of the torque arm to the center of gravity of the charge, θ_{com} tilt angle of the charge relative to vertical. Using a charge volume of 50%, R_{com} was found by calculating the centroid of the charge as 0.2mm. The mill power usually peaks at 80% critical speed, which is equivalent to $6.13rd/s$. The radius of the torque, $\theta_{com}$was calculated using equation (0-4),

$$\theta_{com} = \arctan(\frac{\omega^2 R}{g}) \quad (0\text{-}2)$$

where ω is the angular velocity, R is the radius of the mill, and , g denotes acceleration due to gravity. The calculated value tilt angle of the charge, θ_{com} was found to be $33.8°$ and subsequent torque of $78.28N.m$. A ball mill offset of 0.02m was assumed due to imbalance of the mill drum adding an extra torque of 8.52Nm. The power required was found to 532.08W, including an allowance for friction, windage, start-up acceleration, and safety factor of safety of 1.5 totaling 1140.18w. A standard electric motor sized at 1.5 kW operating at 150 rpm was selecting for the drive. Four lifters for the size of the ball mill produced optimum collisions according to previous work by (Muhayimana, 2019).

3.3 Experimental Setup

In this research, a specialized test apparatus to investigate granular flow patterns controlled conditions was constructed as shown in

Figure 0.3. The system incorporated a variable-speed electric motor regulated by a frequency converter, providing precise speed control from stationary operation to beyond the theoretical critical rotation threshold. A digital tachometer provided real-time speed verification through an integrated display panel. For mechanical power analysis, the apparatus employed a high-precision rotary transducer (200 Nm capacity, 24V DC operation) interfaced with a National Instruments USB-6009 data acquisition module. Custom-developed algorithms processed the sensor outputs to compute torque and power consumption values.

The experimental design compared two geometrically distinct mill configurations - hexagonal and cylindrical profiles - maintaining identical cross-sectional areas and (355 mm). Both mills featured 4 mm-thick natural rubber linings on all interior surfaces except the observation face, which utilized transparent polycarbonate for optical access. Complete technical specifications for the experimental apparatus appear in

.

Figure 0.3: Fabricated Experimental Rig in Operation

The flat-end design minimized boundary effects on particle dynamics. High-resolution digital imaging captured the granular motion, with subsequent analysis quantifying characteristic charge features (shoulder and toe positions) relative to a standardized reference point at the 3 O'clock position.

Table 0.1: Experimental Setup Technical Specifications

Component	Specifications
Electric motor	Three phase 1.5HP, 240 V, 50Hz, Serial No.19A002
Motor controller	VFD Model: ABB ACS150-01E-09A8-2, Timer, Motor overload protection, on/off switches, Emergency button, indicators
Reducer	MODEL WTX-1050A, $\emptyset 28mm$, Torque range 130-400Nm, Max speed 2000 rpm, Signal output 0-10v, Power supply 24VDC/500mA Helical geared unit with coaxial shaft in line with the motor shaft. Reduction ratio 7.5
Dynamic Torque Sensor	Ø28 axle Torque range: 130-400Nm, Max speed 2000rpm. Signal output of 0-10v, Power supply: 24VDC/500mA,
Data acquisition	National Instruments USB-6009 Multifunction DAQ, input 0-10V, Output analogue/digital. Sampling Frequency; each analogue input - 48 kS/s. Analog outputs -150 S/s. Resolution: analogue inputs 14-bit analogue outputs 12-bit.Camera specifications: Canon EOS 90D DSLR, 18-135mm zoom lens, 32.5MP APS-C CMOS Sensor, 10 fps.
Mills	Hexagonal and Cylindrical profiles, Area: 876.27cm2, Length: 355 mm, diameter 0.345mm, critical speed 73.19 r.p.m
Lifters (Steel)	Rectangular profile: height:10 mm, width:20 mm
Grinding media	Material: High Cr-Mn-Steel, density 7850, Mean Ø 12.15mm, bulk density 4460 kg/m3

3.4 DEM Simulations

Numerical simulations were conducted using the Academic Version of Altair EDEM to evaluate and compare the performance of cylindrical and hexagonal mills under different operating conditions. The simulations involved varying the mill speed between 55% and 95% of the critical speed, representing a broad spectrum of ball mill operation speeds. Charge filling levels ranged from 9% to 48% of the mill's internal volume, a range selected to maintain operational efficiency, avoiding overfilling, which can reduce grinding effectiveness and increase power consumption, and underfilling, which can accelerate media wear due to excessive contact. The investigation also included assessing the influence of six rectangular lifters within each mill and analyzing how lifters shaped as regular polygons with 4 to 16 sides affected mill performance. In total, 103 simulations

were performed. The mill designs were created using CAD software, converted into standard format files, and imported into the EDEM simulation environment. Spherical grinding media with a 12.15 mm diameter were used, and the simulations considered both particle-particle and particle-wall interactions, including restitution, static friction, and rolling friction coefficients. Table 0.2 shows a summary of the factors and levels used in the simulation.

Table 0.2: Summary of Factors and Levels used in DEM Simulation

Factor	Type	Levels
Mill geometry	Categorical	2 levels: Cylindrical, Hexagonal
Mill speed (% of critical speed)	Continuous (discretized)	55%, 65%, 75%, 85%, 95%
Charge filling level (% of mill volume)	Continuous (discretized)	9%, 18%, 28%, 38%, 48%
Lifter presence	Categorical	2 levels: With lifters (6 rectangular), Without lifters
Polygonal profile	Discrete numerical	4, 6, 8, 10, 12, 14, 16 sides

During the simulation, grinding media diameter (12.15 mm), material properties, contact parameters (restitution, static friction, rolling friction), simulation time, and particle generation procedure were held constant. The primary responses extracted from the simulations were: charge motion characteristics, collision energy distribution, power draw, torque variation, mill wear. Grinding efficiency was shown by a ratio between interparticle collisions and power draw.

A full factorial combination for primary operating variables (mill speed × filling level × mill geometry). No physical replication was performed, as DEM simulations are deterministic given identical initial and boundary conditions. Variability was minimized by allowing particle beds to reach a stable packed state before data collection and through consistent particle generation, settling procedures, and simulation durations. Each simulation began with particle generation and settling under gravity until a stable packed bed was achieved through energy dissipation. The accelerations are numerically integrated

over a time step to update particle velocities and positions defined by (Liu et al., 2025) in equations (0-3) and (0-4),

$$x(t + \Delta t) = x(t) + v(t)\Delta t \quad (0\text{-}3)$$

$$v(t + \Delta t) = v(t) + a(t)\Delta t, \quad (0\text{-}4)$$

where v is velocity in m/s, x is the position $a(t)$ is the acceleration of a particle at a given time t, Δt is the time step. Rotational velocity and particle orientations were updated using equations similar to equations (0-3) and (0-4). Equation (0-5) vector that applies component-wise in all three spatial directions. The critical time-step was calculated using the theoretical expression for the Rayleigh wave velocity for the system defined by (Otsubo et al., 2017) in equation (0-5),

$$\Delta t_{crit} = \frac{\pi R\sqrt{\rho/G}}{0.1631\nu + 0.8766} \quad (0\text{-}5)$$

where ρ is the particle density, R is the average particle radius, G is bulk modulus and ν is poisson ratio. Simple DEM simulation models use linear contact models where a constant spring stiffness is applied to all contacts. Data extracted from the simulations, including charge motion profile snapshots, was thoroughly analyzed to obtain key such as power draw, collision energy, relative wear, and operational stability. The properties of the grinding media and mill are detailed in

Table 0.3. The subscripts $p-p$ describe an inter-particle interaction whereas $p-w$ describe and particle wall interaction.

Table 0.3: Parameters Used for DEM Simulations

Category	Parameter	Value	Source
Boundary	Poisson's ratio	0.5	Supplier Data sheet
	Young's modulus	$3.33 \times 10^{11}\ N/m^2$	Supplier Data sheet
	Density	$1522\ kg/m^3$	Supplier Data sheet
Media	Poisson's ratio	0.3	Supplier Data sheet
	Density	$7800\ kg/m^3$	Supplier Data sheet
	Young's modulus	$2.08 \times 10^{11}\ N/m^2$	Supplier Data sheet
Paired	Inter-particle coefficient of Restitution (ϵ_{p-p})	0.75	Iterative method
	Particle-boundary coefficient of Restitution (ϵ_{p-w})	0.45	Iterative method
	Inter-particle coefficient of static friction ($\mu_{s,p-p}$)	0.5	Iterative method
	Particle-boundary Static friction: ($\mu_{s,p-w}$)	0.65	Iterative method
	Inter-particle coefficient of rolling friction: ($\mu_{r,p-p}$)	0.02	Iterative method
	Particle-boundary rolling friction ($\mu_{r,p-w}$)	0.01	Iterative method
Common	Gravity acceleration	$9.81\ \mathrm{m/s^2}$	Altair EDEM
	Contact model	Hertz Mindlin	Altair EDEM
	Timestep (20% critical timestep)	$\sim 3.05e^{-5}s.$	Altair EDEM

3.5 Boundary Conditions

During simulation, the domain extent was defined by specifying the minimum and maximum values for the X, Y, and Z coordinates. Domain size affects simulation time; the larger the domain, the longer the simulation will take to run. For the particle size of 12.15mm running on a on Corei7, CPU speed of 2.5GHz the simulation time was about 48hrs. Particles that move out of the domain during the simulation are permanently removed from the simulation. To prevent particle removal from the domain, cylindrical periodic boundaries were defined within the domain using the axis from a rotational kinematic or a vector based on a starting or end point. Any particle exiting the boundary

plane will enter the opposing plane, and all forces, torques, positions, and velocities would be rotated by the difference in angle between the two planes.

3.6 Parameter Calibration

A structured Design of Experiments (DOE) methodology was adopted to calibrate the discrete element method (DEM) parameters for the simulation of a cylindrical ball mill operating without lifters. The primary objective of the DOE was to identify, screen, and refine the key interaction parameters governing charge motion and power draw, ensuring close agreement between numerical predictions and experimental observations.

All simulation experiments were conducted under fixed and controlled operating conditions to isolate the effects of material and contact parameters. The mill was operated at a charge filling level of 28% and a rotational speed of 75% of the critical speed, conditions selected due to their stable and repeatable charge behavior. A cylindrical mill without lifters was used to simplify the interpretation of charge dynamics and facilitate reliable measurement of the charge shoulder position. Once the simulated charge reached a quasi-static state, charge motion was characterized using the mean shoulder position obtained from sequential image frames. For each simulation case, sixteen image frames captured over a two-second interval were analyzed, and the coefficient of variation (CV) was calculated to assess the consistency and reliability of the measurements.

The responses considered in the DOE were the mill power draw and the mean shoulder angle of the charge. These responses were selected because they are sensitive to changes in contact parameters and provide complementary measures of bulk charge behavior and energy consumption. Experimental measurements of power draw and charge motion were used as target benchmarks for calibrating the DEM parameters.

The DOE was implemented in three sequential stages: a definitive screening experiment, a sensitivity study, and a response surface optimization using a central composite design (CCD). The first stage consisted of a definitive screening experiment designed to identify

the DEM parameters with the most significant influence on the selected responses. Six paired interaction parameters related to particle–particle and particle–wall contacts were initially considered for calibration. At the same time, boundary conditions and material properties were fixed based on suppliers' datasheets and validated literature. The parameter ranges are summarized in Table 0.4 were used to define the experimental space. Charge motion and power draw were employed as comparative metrics to evaluate agreement between simulation and experimental results. Statistical hypothesis testing was conducted at a significance level of $\alpha = 0.05$, where the null hypothesis assumed that variations in paired parameters did not affect the responses. Parameters exhibiting p-values greater than 0.05 were deemed statistically insignificant and were fixed at representative values for subsequent experiments.

Table 0.4: Parameter Range for Screening Experiments without Lifters

Coefficient	Interaction	Symbol	Parameter range
Restitution	Particle-Particle	$€_{p\text{-}p}$	0.4-0.8
	Particle-Boundary	$€_{p\text{-}w}$	0.3-0.7
Static friction	Particle-Particle	μ_{5p-p}	0.3-0.6
	Particle-Boundary	μ_{5p-w}	0.5-0.9
Rolling friction	Particle-Particle,	μ_{rp-p}	0.01
	Particle-Boundary,	μ_{rp-w}	0.01

Following the screening phase, a sensitivity study was conducted to further quantify the relative influence of the remaining parameters and to reduce the number of required simulations. Thirteen parameter combinations were generated within the reduced experimental space, with three experiments replicated to ensure the reliability and repeatability of the results. Consistent with prior studies, rolling resistance was fixed at 0.01, as this value has been shown to yield realistic bulk behavior for spherical steel and ore particles while avoiding excessive numerical damping. The sensitivity analysis confirmed that friction-related parameters had the largest effect on both power draw and charge behavior, whereas other parameters had a negligible influence and were therefore held constant.

The final stage of the DOE employed a central composite design (CCD) to refine the calibration of the influential parameters and to develop predictive response surface models. Based on the outcomes of the screening and sensitivity analyses, the coefficients of static friction for particle–particle and particle–wall interactions were selected as the primary factors. The particle–particle friction coefficient was varied between 0.3 and 0.6, while the particle–wall friction coefficient ranged from 0.4 to 0.9. These limits defined the axial points of the randomized CCD, which included factorial, axial, and center points to enable the estimation of linear, interaction, and quadratic effects.

In the CCD simulations, the coefficients of restitution for all contacts were assigned fixed values derived from previously validated studies by (Zhang et al., 2023), ensuring realistic collision behavior without introducing additional sources of variability. Analysis of variance (ANOVA) was used to evaluate the statistical significance of the fitted models and to confirm the adequacy of the response surfaces. The resulting second-order regression models as shown in equations **Error! Reference source not found.** and **Error! Reference source not found.** were used to predict power draw and shoulder angle as functions of the frictional parameters.

$$P = 36.12 - 30.1\,\mu_{s,p-p} - 34.5\,\mu_{s,p-w} + 41.9\,(\mu_{s,p-p})^2 + 21.2(\mu_{s,p-w})^2 + 43.9\,\mu_{s,p-p} \times \mu_{s,p-w} \quad (0\text{-}6)$$

$$S = 149.86 + 53.3\,\mu_{s,p-p} + 16.7\,\mu_{s,p-w} - 51.1\,(\mu_{s,p-p})^2 - 6.11(\mu_{s,p-w})^2 + 36.0\,\mu_{s,p-p} \times \mu_{s,p-w} \quad (0\text{-}7)$$

where the respective notations are defined in Table 0.4. The calibrated DEM parameters were obtained through an iterative multi-response optimization process, in which the predicted power draw and shoulder angle were compared against experimental benchmarks. If discrepancies exceeded acceptable limits, the DOE cycle was repeated until convergence was achieved. The final calibrated parameter set minimized the overall prediction error across both responses, and the resulting agreement between simulations and experiments is illustrated in Figure 0.4.

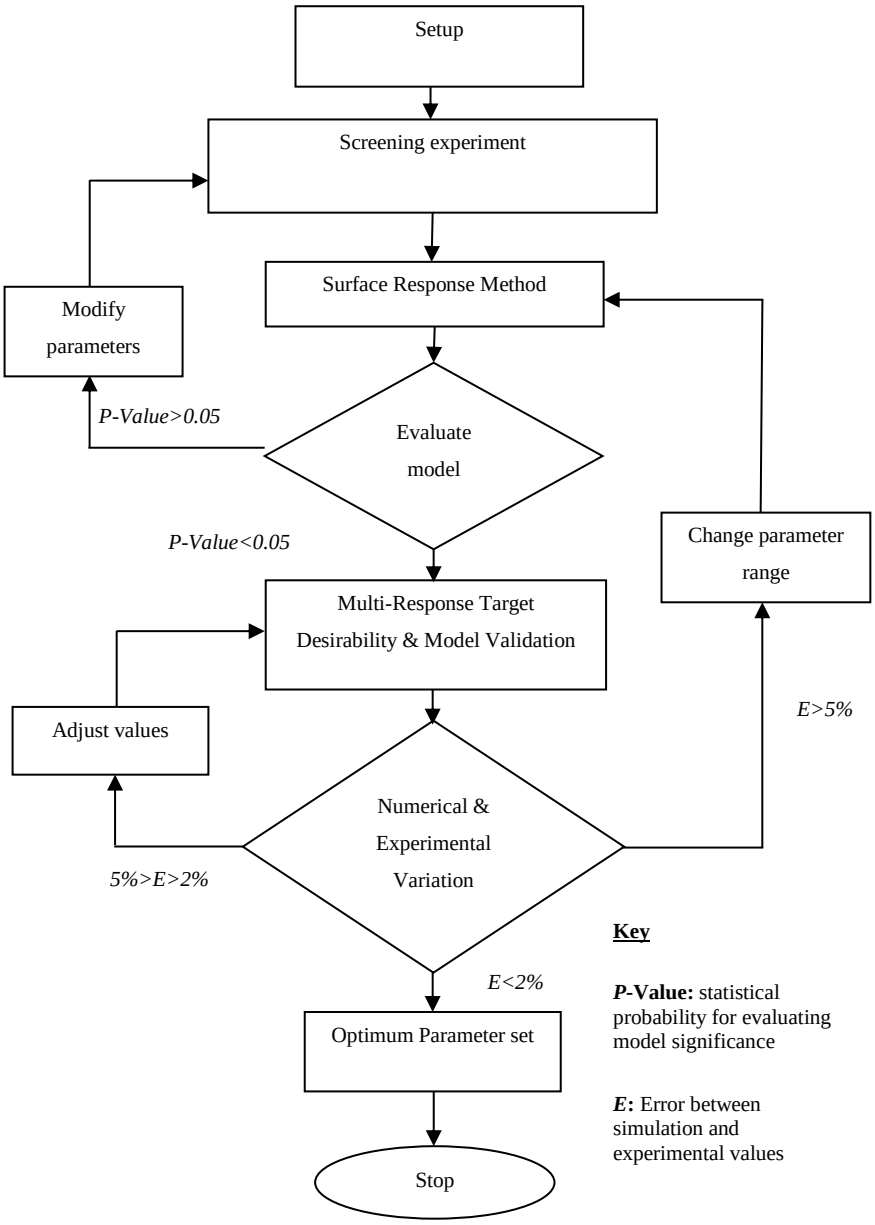

Figure 0.4: Parameter Identification Methodology

3.7 Simulation of Wear

A Multi-Sphere (MS) approach was adopted to construct the particle model. This technique involves superimposing several smaller spheres to create a single, composite

particle that better mimics the complex, irregular shapes found in natural ore. The MS method offers the dual advantage of improved contact detection efficiency and high modeling accuracy and is widely supported in established DEM software packages. One key benefit of the MS method is its ability to replicate complex geometries using only a few spheres, thus preserving computational efficiency. The particle model in this work was developed using EDEM software, which allowed the design of a simulated particle with characteristics closely resembling those of the actual rock sample as shown in Figure 0.5

Figure 0.5: Particle Modelling for Wear Simulation

For the calibration phase, quartz material sourced from an informal mining site in Kajiado County, Kenya was selected due to its abrasive properties, low cost, and local availability. The key parameter used to characterize and calibrate the bulk material was the Angle of Repose (AoR). This is the steepest angle at which a bulk material remains stable without sliding. This property, while simple to measure, is closely linked to more complex material attributes such as inter-particle friction. As a result, it serves as a critical indicator for effective calibration. The AoR was determined using a cylindrical apparatus with a diameter-to-height ratio of 1:3, chosen for its ability to facilitate uniform material flow once the cylinder is lifted (Beakawi Al-Hashemi & Baghabra Al-Amoudi, 2018). Specifically, a cylinder measuring 70 mm in diameter and 210 mm in height was employed. This size allowed for sufficient material volume to form a stable pile suitable for measurement. The pile formed by a bulk material at its Angle of Repose (AoR) is characterized by a conical shape with a circular base and symmetrical, straight sides; the

slope of these sides is precisely equal to the material's inherent AoR (Higashitani et al., 2020). This equilibrium angle, determined by internal friction and cohesion, represents the critical point where gravitational forces pulling particles down the slope are exactly balanced by frictional forces resisting movement. The peak of the cone is sharp for free-flowing materials like dry sand, while more cohesive substances may exhibit a rounded apex. For an accurate AoR measurement via the pulling cylinder method, a near-zero acceleration should be achieved to allow the pile to form in equilibrium (Li et al., 2020). A total of 10 trials were conducted, and the average AoR was computed for use in the particle calibration process. Building on the charge motion model introduced in earlier sections, this study integrates a wear model and a geometry modification strategy to predict both the wear distribution on the shell liner and the resulting changes in its geometry over time.

The first step in this process involves identifying the onset of a pseudo steady-state during the simulation. Once this state is established, tangential damping energy data is collected for each facet of the liner across multiple rotations. This data reflects the relative wear experienced by each surface. To quantify the wear, the relative wear rate is calculated by dividing the accumulated wear data by the duration of data collection. To convert these simulation results into real-world values, actual wear profiles are measured from physical liners, and a correlation between the relative wear rate and absolute volume loss is established. This relationship defines the wear constant, effectively linking the simulation model with physical observations. Using the wear constant, the absolute wear rate for each liner facet can be determined. The total volume loss of each element is then predicted by multiplying this wear rate by the expected operational hours. With this information, the geometry of the liner is updated to reflect material loss, enabling accurate predictions of performance degradation and maintenance needs over time.

3.8 Ore Materials

Copper ore was obtained from Mithikwani in Matinyani division, Kitui West Constituency in Kenya. A large sample was obtained from an area of approximately $200m \times 4m$. The

overburden was removed to a depth of about 1m, and the ore rock was blasted. The boulders were transported and crushed using an industrial jaw crusher. In this study, polished thin sections were sampled and prepared at the Madini house in the Ministry of Mining and Petroleum laboratory in Nairobi. The analyses of the minerals for the mineralogical and chemical composition were done using X-ray Fluorescence (XRF) and Atomic Absorption Spectroscopy (AAS). Chemical compositions were obtained with the Bruker Esprit 1.9 software. Gold ores were obtained from Osiri, Lolgorian and Ndhiwa within the Migori gold belt, denoted by S, L, and N, respectively. These individual ores were mixed to form three binary blends and one ternary blend according to weight percent as shown in Table 0.5. Ore blending in gold milling is used to stabilize mill throughput, control feed grade variability, and improve overall recovery (Dunne et al., 2019).

Table 0.5: Material Compositions for Gold Ore

Material type	Composition	Text name
Individual ores	Osiri	S
	Lolgorien	L
	Ndhiwa	N
Binary ore blends	50% S + 50% L	Blend A
	50% S + 50% N	Blend B
	50% L + 50% N	Blend C
Ternary blend	40%O +20%L+40%N	Blend D

3.9 Grinding Tests

The dry ball milling process was used in the laboratory grinding tests. The grinding tests were carried out according to the procedure known as the one-size-fraction method (Austin & Bagga, 1981). This is a laboratory technique used to empirically determine the breakage function in comminution (grinding and crushing) models. It involves grinding a monosized (narrow size fraction) feed material in a batch mill for a short time, then carefully sieving the product to analyze the resulting size distribution. The ore samples were reduced in size using a jaw crusher, shown in Figure 0.6. The samples were then ground in a ball mill to reduce to standard sieve size classes within the ranges of –3.35+2.36 mm, –2.36+2.00 mm, –2.00 +1.70 mm, –1.70+1.40 mm, and -1.40+1.00 mm.

Figure 0.6: A Laboratory Jaw Crusher at JKUAT Engineering Workshops

The samples were then split into batches using the cone and quartering method. This is a sampling method used to obtain a small, representative sample from a large, heterogeneous pile of granular material. The process involves forming the material into a symmetrical cone by pouring it through a central point, then dividing the cone into four equal quarters with a cross-shaped cutter. Two opposite quarters are selected and combined, while the other two are discarded. This sub-sample is then re-coned and quartered repeatedly until the desired sample size is achieved. A pre-grinding procedure was implemented to generate particle strength and shape distributions representative of those typically produced in the test ball mill under defined operating conditions. This step was essential to ensure that these properties remained relatively stable during the initial phase of grinding, thereby preventing significant changes that could affect the specific breakage rate. As noted by (Gupta, 2017), maintaining consistent particle characteristics at the onset of grinding helps achieve more accurate breakage kinetics. Figure 0.7 shows a typical sample of copper and gold ore in the size class of –2.36+2.00 mm.

(a) Copper Ore

(b) Gold Ore

Figure 0.7: Prepared Samples in the Size Class –2.36+2.00 mm

The volume occupied by grinding media J, and material filling f_c, were calculated based on equations (0-8) and (0-9) proposed by (Petrakis et al., 2017),

$$J = \left(\frac{V_b}{V_m}\right).\frac{1}{1-\varepsilon} \tag{0-8}$$

$$f_c = \left(\frac{V_p}{V_m}\right).\frac{1}{1-\varepsilon} \tag{0-9}$$

where V_b is the volume of solid grinding media, V_p the volume of solid powder, V_m is mill volume and ε is the bed porosity of grinding media. Randomly packed granular beds naturally fall in the range $\varepsilon \approx 0.36 - 0.45$, and 0.4 is the validated average used in engineering calculations. The interstitial filling U is calculated using the equation (0-10).

$$U = \frac{f_c}{\varepsilon.J} \tag{0-10}$$

The operating conditions for the milling tests are summarized in Table 0.6. Grinding was conducted at a range of time intervals: 0.5, 1, 2, 5, 10, 15, 20, 25, and 30 minutes. Short grinding durations were selected based on the one-size-fraction method described by Austin and Bhatia (1972). After each test, samples were sieved using a series of screens

with mesh sizes increasing by a √2 progression to determine the particle size distribution. The material retained on the screens, along with the remaining mill contents, was then used as the feed for the subsequent grinding interval.

Table 0.6. Laboratory Ball Mill Operating Conditions

Parameter	Value
Mill diameter, D (m)	0.350
Mill length, L (m)	0.355
Lifters	No.4,rectangular Profile
Grinding media beb, J (%)	30
Interstitial filling,U (%)	67
Material volume fraction, fc	0.08
Mill speed (% critical speed)	75
Ball size , d(mm) Distribution	38(30%), 25mm(60%), and 19mm (30%)

The specific breakage rates were determined by plotting the fraction retained on the top size for each size interval against time according to equation (0-11). The obtained value was fitted in equation (0-14) to obtain the model parameters. Equation (0-16) was used to obtain breakage functions for each feed size. The values were fitted in equation(0-17) to determine the other model parameters. The breakage distribution is normalizable thus, the size distribution of other grinding products can be reproduced. The specific rate of breakage, S_i , and the breakage distribution function, b_{ij} were determined using the *BallParam_Batch* spreadsheet available in Moly-Cop Tools™, which applies the full set of differential equations from the population balance model (PBM). This tool identifies the optimal parameter combination by minimizing the residual error between experimental and model-predicted particle size distributions. The fitting error is quantified according to (Petrakis et al., 2017) by equation (0-11):

$$\varphi = \sum_{i=1}^{n} w_i \left(\frac{F_i - R_i}{R_i}\right)^2 . 100\%, \qquad (0\text{-}11)$$

where F_i denotes the experimental mass fraction retained on the screen size x_i, R_i is the model-predicted fraction retained for the same screen size in mm, n is the number of screen intervals, and w_i represents a weighting factor that reflects the relative reliability

of each screen size measurement, with higher values indicating more accurate data. For accurate parameter estimation, the software requires input from at least four particle size distributions measured at different grinding times.

CHAPTER FOUR

RESULTS AND DISCUSSION

4.1 Introduction

This chapter first discusses the results of the discrete element simulation of ball mill operating conditions. The mill profile, lifters, and speed are evaluated on the effects on collision energy, power draw, operational stability, and wear. Finally, the grinding kinetics of copper and gold ore are discussed.

4.2 Ball Mill Operation Conditions

4.2.1 Parameter Identification

In the screening experiment, it was ascertained that coefficients of static friction and restitution had a low influence on power and charge behavior. Coefficients of rolling friction had the greatest effect on power draw and shoulder angle. The high value of interparticle rolling friction ($\mu_{r,p-p} = 0.2$) produced average power output value in the range of $211 - 215\text{W}$. The lowest value of $\mu_{r,p-p} = 0.05$ produced power value of $172 - 194$ W. The coefficient of inter-particle rolling friction of 0.2 created adherence of particles, which was far from the observed particle behavior. A value of 0.05 was close to the experimental average shoulder angle of $160°$ value as shown in Figure 0.1.

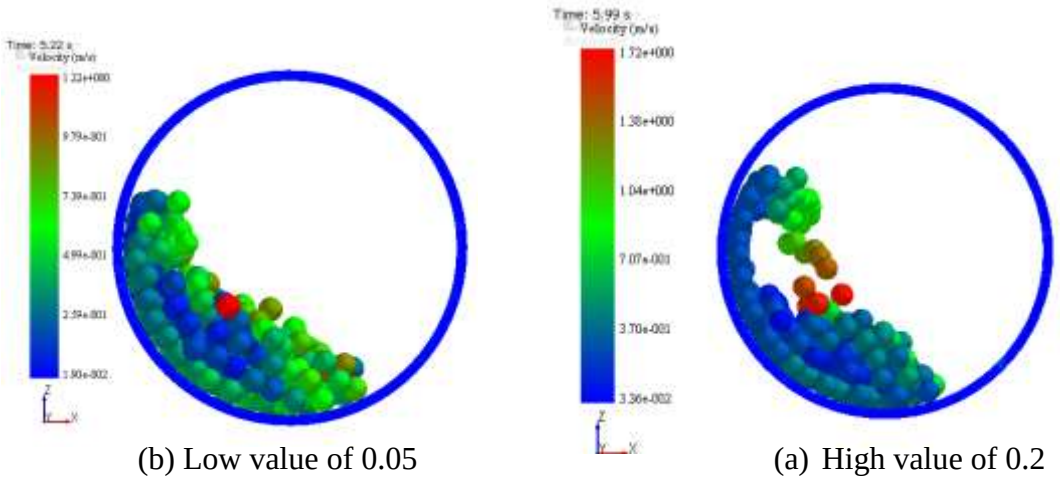

(b) Low value of 0.05 (a) High value of 0.2

Figure 0.1: Effect of the Coefficient of Friction on Charge Motion

The lower value of particle–wall rolling friction better approximated the expected value of shoulder angle. The best combination of parameters was determined to closely approximate the experimental values of a power draw of $136.88W$ and a shoulder angle of $160.3°$. **Error! Reference source not found.** shows a summary of the calibrated parameters. The optimal parameter combination matching experimental results was determined to be $\mu_{s,p-p} = 0.5$; for interparticle sliding friction, and $\mu_{r,p-\mathrm{w}} = 0.65$ for particle-wall rolling friction. The higher rolling friction coefficient at the mill wall reflected the actual material properties of the system components. These parameters exhibited an essentially linear correlation within the experimental operating range, with the solution demonstrating uniqueness as evidenced by the absence of inflection points in response curves.

Validation studies using these calibrated parameters across various rotational speeds and fill volumes (**Error! Reference source not found.**) showed excellent agreement with experimental data. The simulations predicted power draw within 2% of measured values and reproduced shoulder angles within 6.2% accuracy. This level of precision aligns with the ±2° variation observed in repeated shoulder angle measurements. The maximum

deviations of <2% for power and <4° for shoulder position fall within the acceptable range established in previous DEM validation studies (Cleary et al., 2003).

Qualitative validation through comparative image analysis (

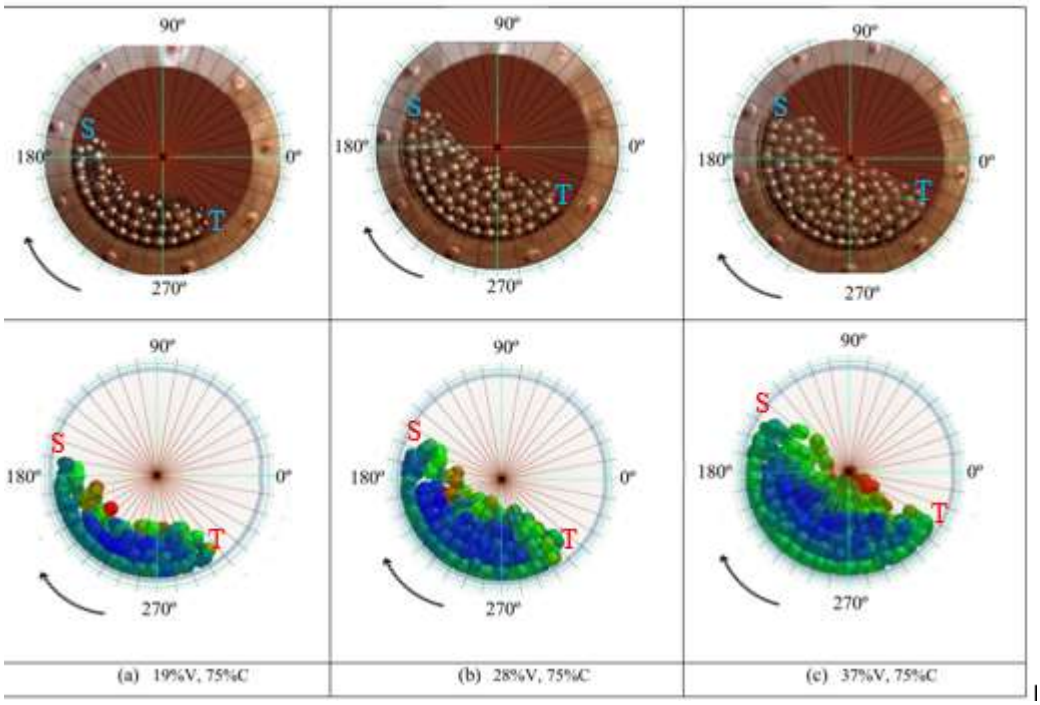

Figure 0.2) further confirmed the model's accuracy. The DEM simulations successfully replicated key charge characteristics including shoulder position, free surface profile, and bulk toe location across all tested conditions. The velocity-color mapping (blue = low speed, red = high speed) in simulation snapshots provided additional visual confirmation of realistic particle behavior patterns. This comprehensive validation demonstrates that the calibrated DEM model reliably predicts the ball mill's operational dynamics.

Table 0.1: Validation of Calibrated

Fill		Power(W)			Shoulder Position (deg)		
	Speed	Experimental	Simulation	Error(%)	Experimental	Simulation	Error(%)
26kg	65	87.21	83.90	3.8	170.6	170.4	0.1
	75	100.41	96.45	3.9	170.9	168.2	1,6

	85	**115.38**	**112.72**	**2.3**	**169.7**	**167.1**	**1.6**
39kg	**65**	**117.94**	**118.02**	**0.1**	**162.3**	**162.5**	**0.1**
	75	**136.88**	**138.11**	**0.9**	**159.9**	**160.3**	**0.2**
	85	**158.20**	**154.76**	**2.2**	**158.3**	**158.0**	**0.2**
52kg	**65**	**147.22**	**145.13**	**1.4**	**153.4**	**148.8**	**3.1**
	75	**171.78**	**169.24**	**1.5**	**149.6**	**146.2**	**2.3**
	85	**196.53**	**193.24**	**1.7**	**148.3**	**141.7**	**4.7**

Table 0.2: Summary of Calibrated Parameters

Coefficient	interaction	Value
Restitution	Particle-Particle, $\epsilon_{p\text{-}p}$	0.75
	Particle-Boundary, $\epsilon_{p\text{-}w}$	0.45
Statistic friction	Particle-Particle, μ_{5p-p}	0.5
	Particle-Boundary, μ_{5p-w}	0.65
Rolling friction	Particle-Particle, μ_{rp-p}	0.01
	Particle-Boundary, μ_{rp-w}	0.02

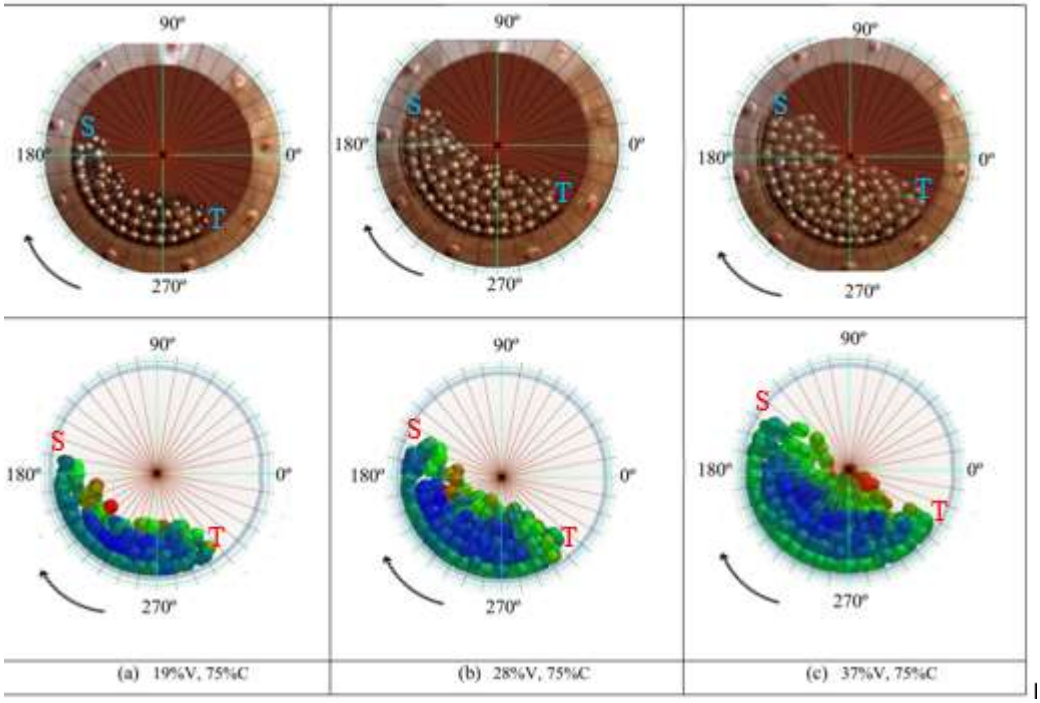

Figure 0.2: Comparison Between Experimental and Simulation Results

4.2.2 Charge Profile and Motion

The energy available for particle breakage and mill wear characteristics is fundamentally governed by the charge motion profile. Increasing mill rotational speed produced a corresponding rise in particle velocities. The color-mapped velocity represents the instantaneous center-of-mass velocity of each particle. The numerical velocities for particle groups were obtained by calculating region-wise averages in bins. The color-mapped velocity coding revealed three distinct motion regimes: (1) green particles in the low-velocity abrasion zone (<0.5 m/s), (2) red particles undergoing high-velocity cataracting/centrifuging (>2 m/s), and (3) blue particles in the slow-moving zone (<0.5 m/s), with all motion occurring in a clockwise rotation.

Figure 0.3 illustrates the characteristic charge dynamics in a lifter-free cylindrical mill, where particles ascend to the shoulder position (denoted by T) before cascading along the free surface to the toe region. At elevated speeds and fill levels (typically >75% critical speed and >35% fill volume), distinct cataracting streams become prominent. The charge structure consistently adopts a kidney-shaped profile, featuring a central core of low-velocity particles (0.1-0.3 m/s).

Force transmission in this configuration occurs primarily through frictional interactions, which prove insufficient to prevent substantial particle slippage. Notably, the lifter free cylindrical profile exhibited intermittent charge surging phenomena, characterized by periodic bulk sliding of the charge layer, accompanied by sudden changes in toe and shoulder positions. This behavior results from the complex interplay between gravitational forces and insufficient dynamic friction at the particle-wall interface.

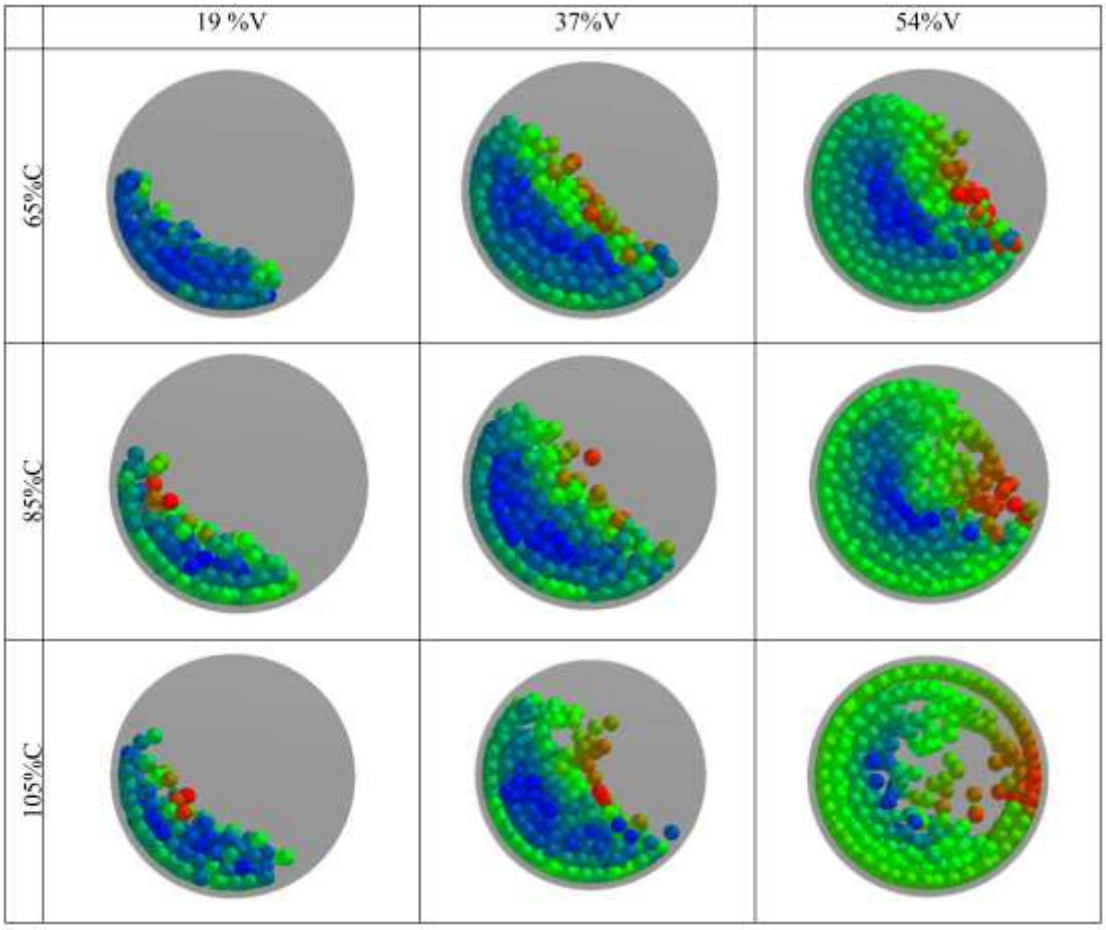

Figure 0.3: Charge Profile Cylindrical Mill without Lifters

The hexagonal mill configuration without lifters demonstrated distinct charge dynamics, as shown in Figure 4.4. This geometry promoted enhanced media elevation, with approximately 15-20% more particles achieving detachment from the bulk charge compared to cylindrical equivalents. While maintaining the characteristic kidney-shaped profile, the system exhibited unique vertical oscillations in the typically low velocity region (0.1-0.3 m/s), driven by periodic interactions with the hexagonal vertices. The geometry's six contact points accumulated grinding media before transporting them along cascading trajectories, with particle velocities reaching 1.5-2 m/s on the free surface. At operational parameters exceeding 70% critical speed and 30% fill volume, approximately 25% of particles exhibited discontinuous flow patterns, leading to intensified particle-particle interactions.

Figure 0.5 reveals the significant influence of polygonal side count on charge behavior in simulations conducted at 75% critical speed with 28% fill volume. Square-profile mills generated an expansive stagnant zone (40-50% of charge volume) with correspondingly low average particle velocities (0.05-0.1 m/s). This configuration produced the most pronounced velocity gradient across the charge, ranging from near-static conditions in the core to 1.8-2.2 m/s in cascading streams. The data suggests an inverse relationship between vertex count and stagnant zone volume, with hexagonal profiles reducing the dead zone by approximately 30% compared to square configurations under identical operating conditions.

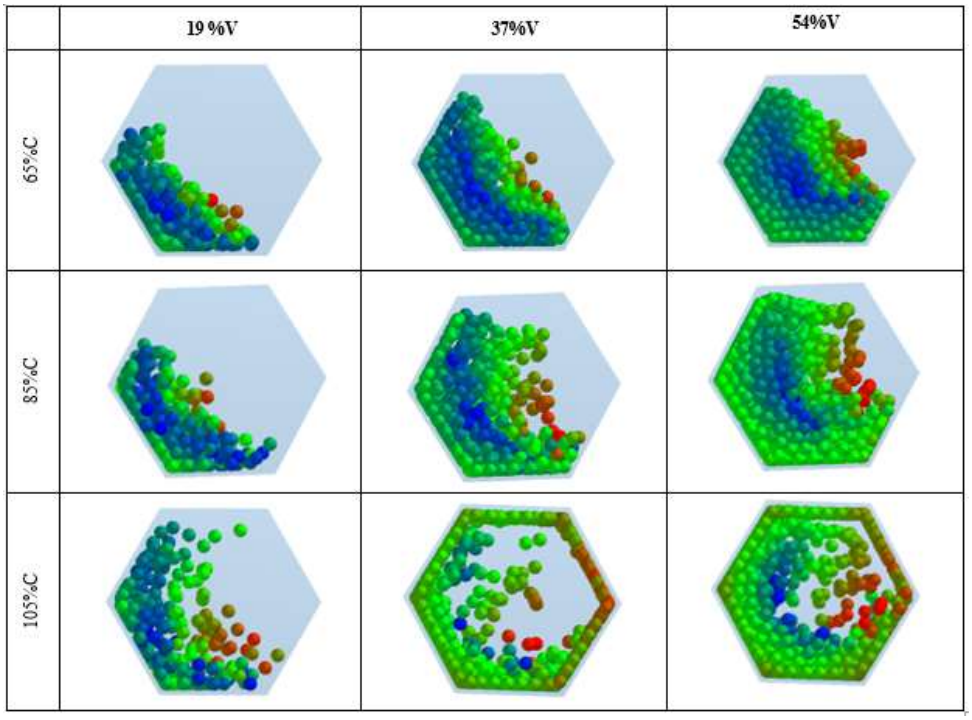

Figure 0.4: Charge Motion for Hexagonal Mill without Lifters

The study found that particle velocity in rotating mills depends significantly on the number of sides in polygonal mill designs. Fewer sides increased sliding, reducing speed, while higher side counts (8, 12, 16) led to fewer fast-moving particles, with the slowest motion in the 16-sided mill. This indicates an optimal intermediate shape for maximizing particle movement, such as a hexagon or octagon. Additionally, higher rotational speeds

(95% critical speed) enhanced velocity compared to slower operation (65% critical speed. In lifter-free mills, increased fill volume improved particle motion by increasing wall friction, whereas mills with lifters, especially hexagonal ones, showed better particle lifting and higher speeds due to mechanical agitation. These findings confirm that mill geometry profile, lifter presence, and fill level critically influence grinding efficiency. The internal geometry of a grinding mill directly controls the trajectory of grinding media and ore particles as shown in Figure 0.5. Variations in mill profile, such as cylindrical versus polygonal geometries or the inclusion of lifters, alter the balance between cascading, cataracting, and centrifuging motion regimes. These regimes determine the frequency and magnitude of particle–particle and particle–wall collisions, which in turn affect impact energy distribution and grinding effectiveness.

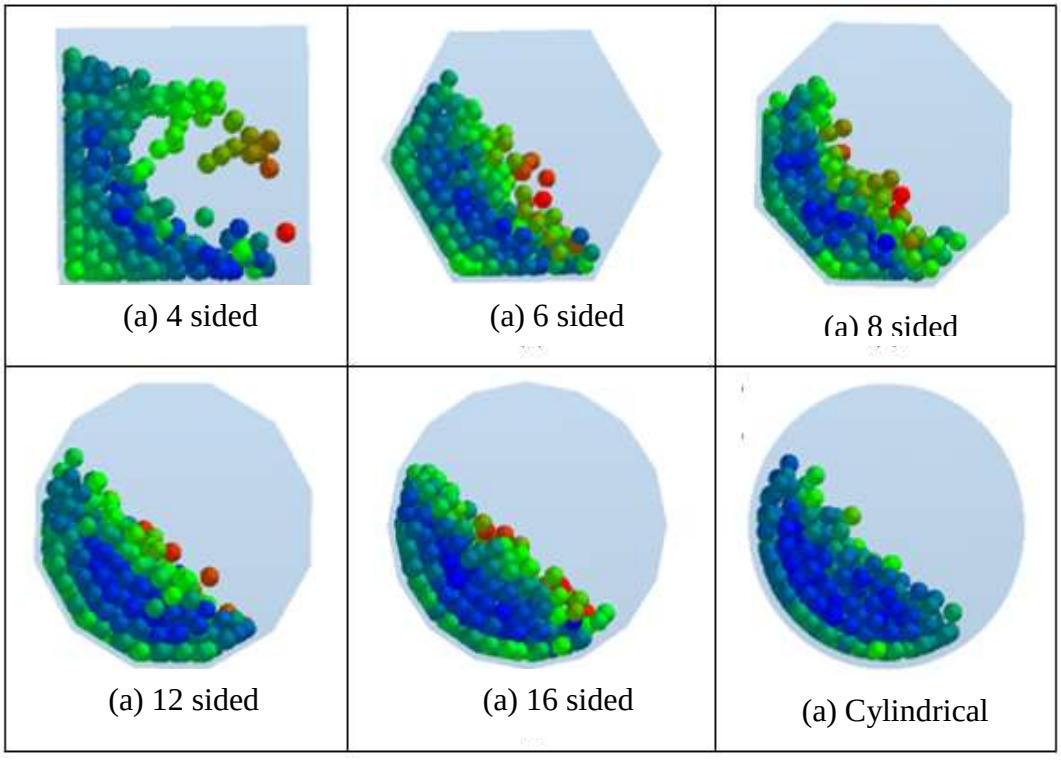

Figure 0.5: Charge Profile Different Polygonal Shaped Mills

The addition of lifters as shown in Figure 0.6 and Figure 0.7 reduced dead zones and increased average particle velocity as. Cataracting particle streams are evident even at lower speeds, while centrifuging is predominantly observed at higher rotation speeds. Additionally, a kidney-shaped charge profile is noticeable in the cylindrical mill at elevated feed levels; however, the hexagonal rotating mill does not exhibit this kidney-shaped profile due to the effects of its vertices.

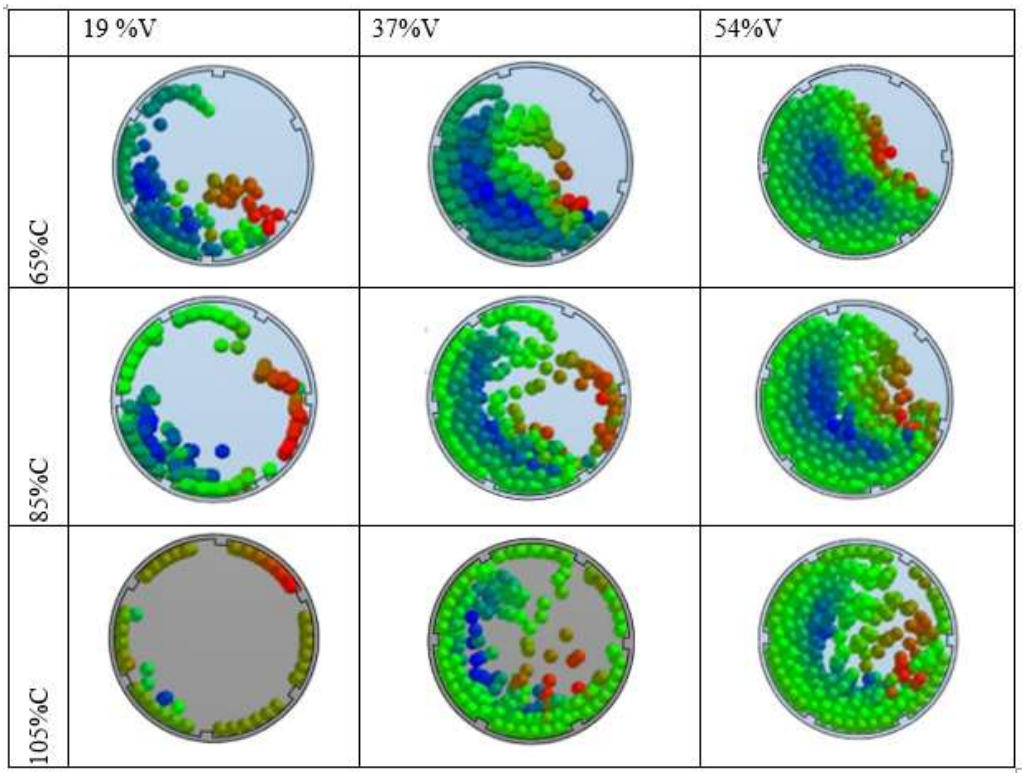

Figure 0.6: Charge Profile of Cylindrical Mill Profile with Lifters

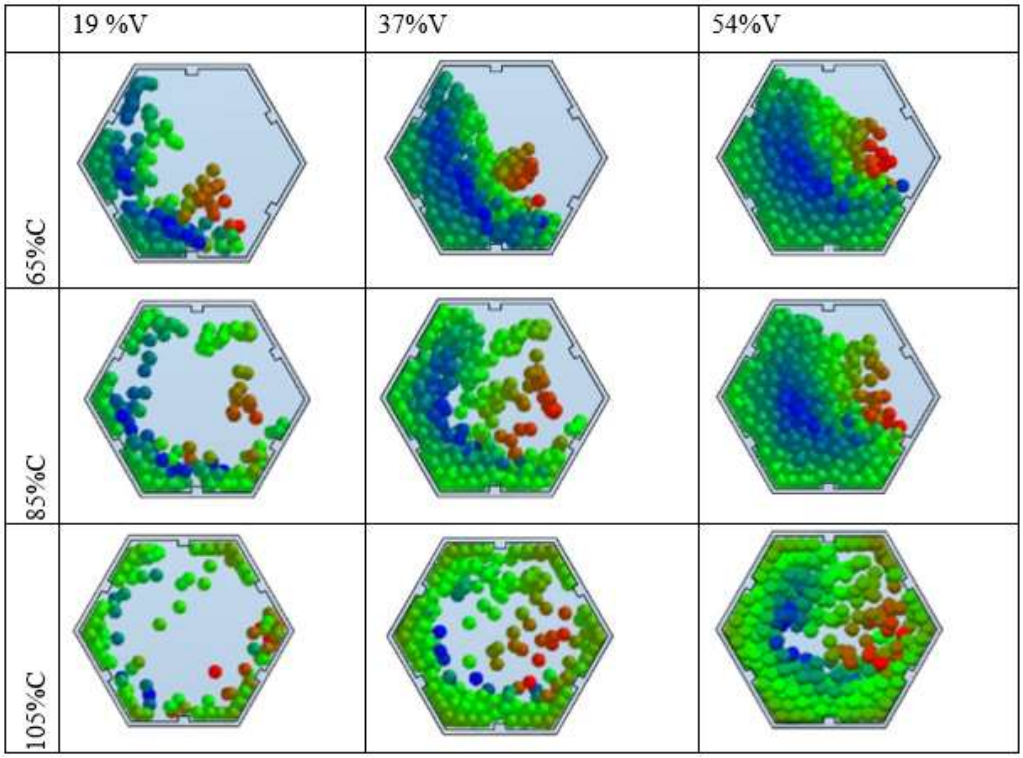

Figure 0.7: Charge Profile Hexagonal Mill Profile with Lifters

Particle velocity is a fundamental descriptor of ball mill dynamics, as it directly the magnitude of impact energy and thereby controls the prevailing motion regime, dominant breakage mechanisms, mixing behaviour, and overall power draw. particle velocity reflects the balance between energy imparted by the mill rotation and lifters and the dissipation of that energy through interparticle collisions within

the charge.

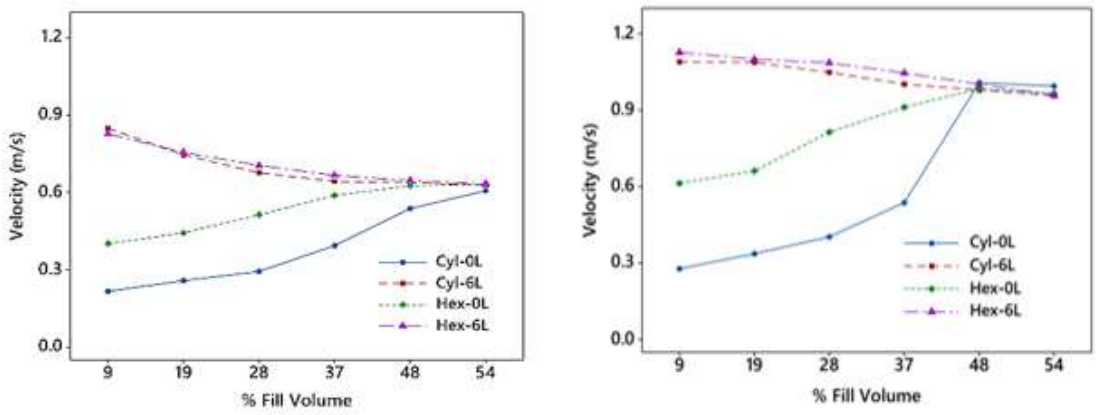

Figure 0.8 illustrates the variation of average particle velocity with fill volume. At a constant mill speed, the average velocity of lifter-equipped profiles decreases with increasing fill level, primarily due to the growing proportion of slow-moving particles within the bulk, which reduces the overall charge mobility. In contrast, particles in the hexagonal mill exhibit comparatively higher average velocities, a consequence of enhanced particle acceleration at the sharp vertices, which promote more effective momentum transfer during lifting and detachment. As the fill level increases further, the average velocities of all four profiles converge at approximately 54% feed, indicating a transition toward bulk-dominated motion. Beyond a fill volume of about 48% at 95% mill capacity, the influence of lifters progressively diminishes; the increasingly dense charge acts as a buffer that absorbs and redistributes kinetic energy through frequent particle–particle interactions, thereby constraining particle motion and reducing the effectiveness of lifters in accelerating the charge.

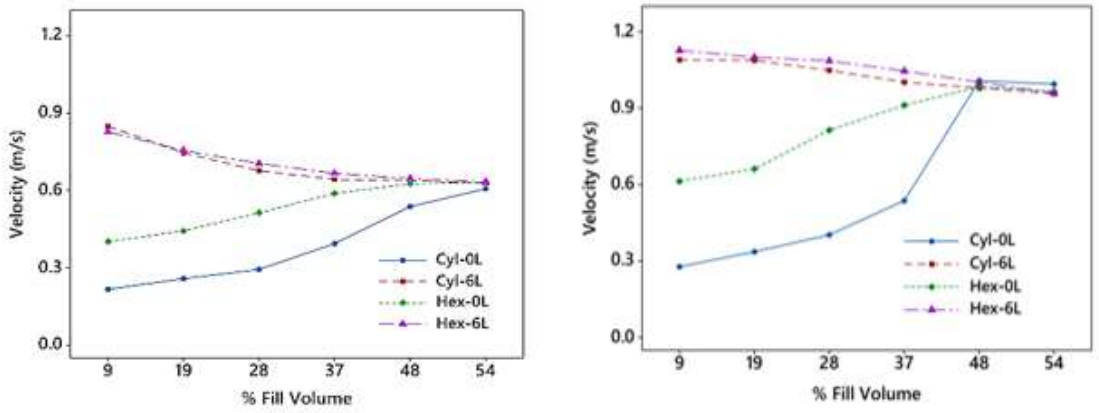

Figure 0.8: Variation in Average Particle Velocity for Various Mill Profile

4.2.3 Collisions and Collision Energy

This study is grounded in the established principle that energy dissipated during interparticle collisions is directly related to the energy available for particle breakage during impact events (Huang et al., 2019). From a physical standpoint, this implies higher collision energy losses correspond to more intense impacts and, consequently,

greater likelihood of particle fragmentation.

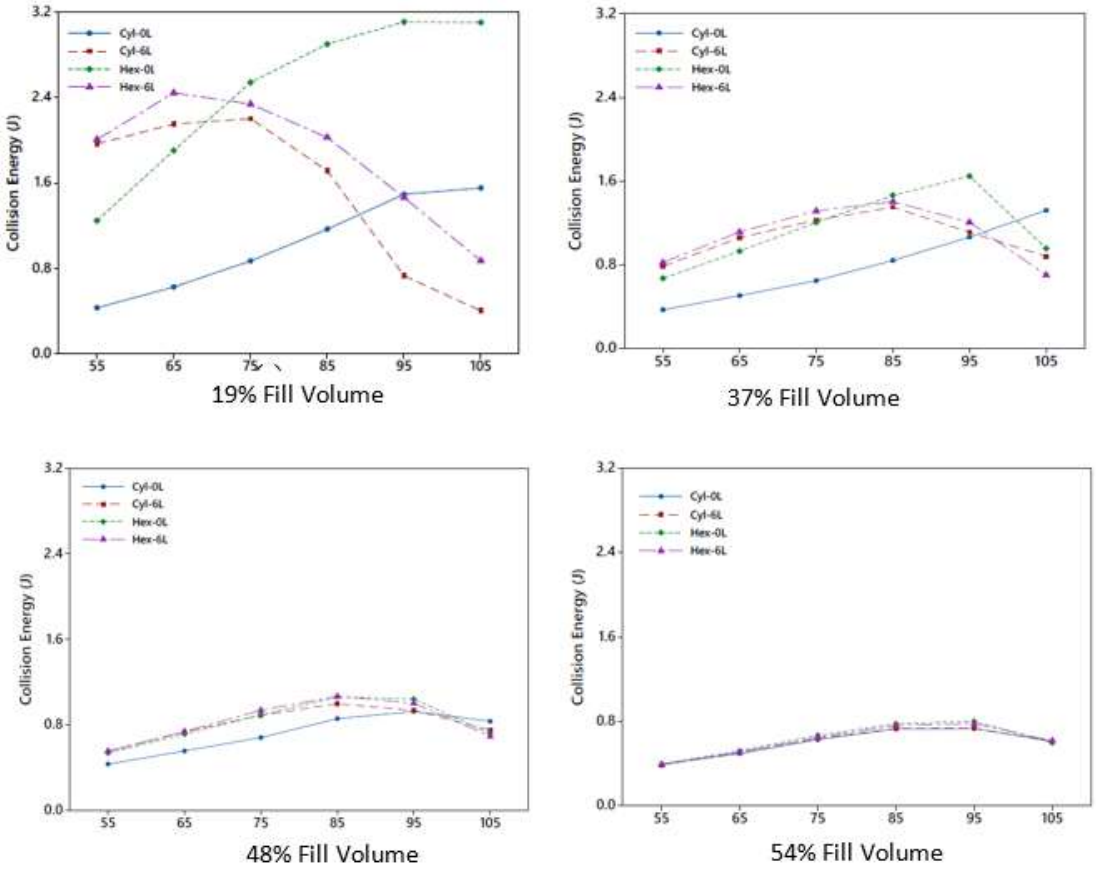

Figure 0.9 illustrates the variation in collision energy characteristics under different operational configurations. The results show that cylindrical mill profiles without lifters exhibit the lowest collision energy losses, reflecting inefficient energy transfer from the rotating mill to the grinding media due to limited charge lifting and particle acceleration. In contrast, hexagonal profiles without lifters achieve 25–30% higher average energy dissipation, which can be attributed to enhanced charge elevation and expansion promoted by the angular vertices, leading to increased particle velocities and impact intensities.

A distinct transition is observed at fill volumes exceeding approximately 37% of the mill volume, beyond which intensified particle–particle interactions disrupt the coherence of the bulk charge and give rise to pronounced collision energy peaks in lifter-free configurations. For mills equipped with lifters, collision energy follows a characteristic

trend, increasing rapidly to a maximum before gradually declining at higher operating conditions. Physically, lifters introduce two dominant effects: first, they increase the frequency of high-energy collisions by 40–50% through improved charge lifting; second, they enhance impact intensity by altering particle trajectories and promoting cataracting motion. At higher fill levels and speeds, however, energy dissipation decreases as particle motion transitions toward more constrained bulk flow and partial centrifugal behavior, reducing effective impact events.

Hexagonal profiles fitted with lifters demonstrate superior energy utilization at sub-75% critical speeds across all fill levels, achieving 15–20% higher collision energy losses than equivalent cylindrical designs. This improvement arises from the combined influence of lifters and geometric vertices, which reduce particle slip and promote more efficient momentum transfer. Maximum energy dissipation consistently occurs within the 70–90% critical speed range, where particle impact forces are greatest. The peak typically appears near 80% of critical speed, corresponding to optimal conditions for effective fracture energy transfer and comminution efficiency.

4.2.4 Normal Cumulative Geometry Force

The normal cumulative force was an indicator of the magnitude of impact forces acting on the mill's geometry. Generally, as the material fill increased, the average normal cumulative geometry force increased as shown in Figure 0.10. This increase was attributed to the higher number of particles interacting with the mill wall, which increases collision dynamics. Among the various mill designs assessed, the hexagonal mill consistently exhibited the highest cumulative geometry force across all experimental conditions. The vertices of the hexagonal shape were involved in facilitating greater lift for the media particles. As these particles accumulated at the vertices, they gained kinetic energy and were forced toward the sides of the polygon at significantly higher speeds, resulting in intensified impact forces on the mill’s structural geometry. Adding lifters to the hexagonal mill configuration led to a marked reduction in cumulative energy force.

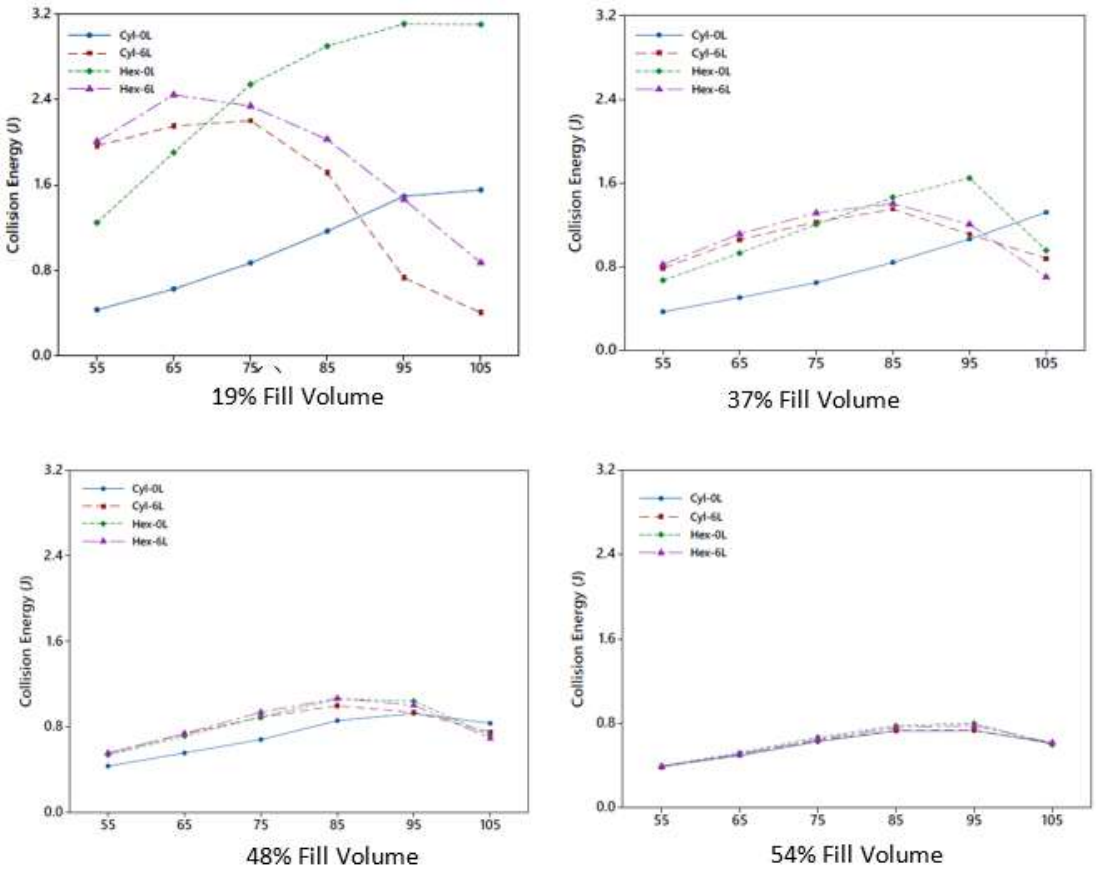

Figure 0.9: Variation of Inter-Particle Collision Energy Loss

The lifters positioned at the center of each side, parallel to the length of the mill, considerably altered the trajectory and motion of the particles. This design effectively expanded the charge within the mill, enhancing interparticle interactions during which ultimately diminished the impact forces experienced by the mill. Expanded charge produces cataracting streams associated with high impact collisions. The cylindrical mill profiles demonstrated the lowest average cumulative force due to their unique charge behavior. In these designs, the elevated toe position restricts particle flow in the direction opposite to the movement of the mill, thereby reducing impacts on the mill's geometry. The natural flow patterns of cascading and cataracting particles in a cylindrical mill predominantly impact the toe position, further lessening the intensity of forces on the mill wall.

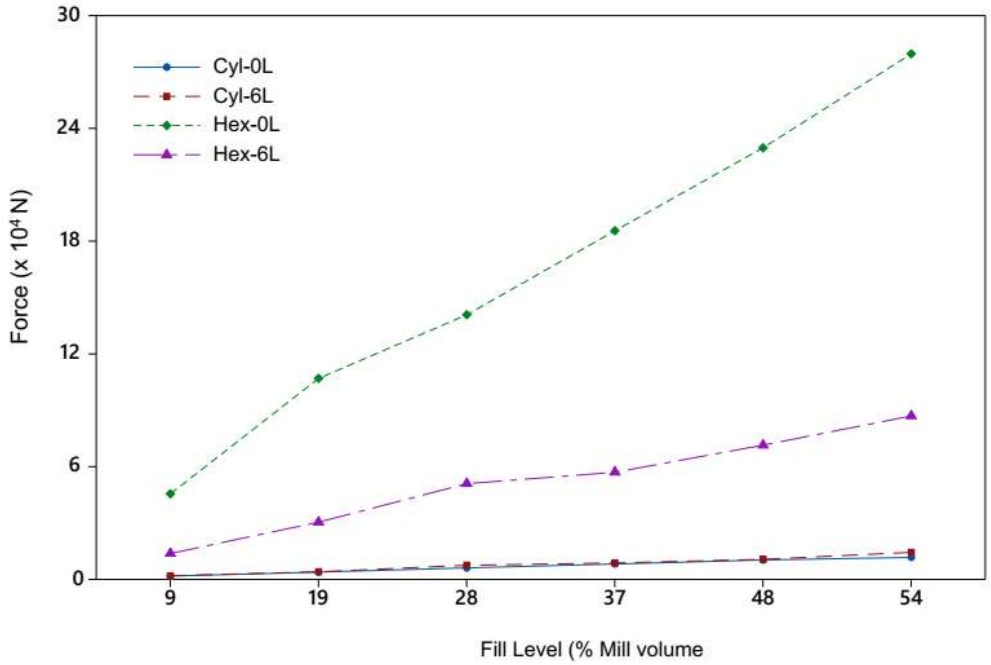

Figure 0.10: Variation of Normal Cumulative Geometry Force

Additionally, the cylindrical profile tends to encourage a centrifuging motion, a phenomenon that not only reduces the intensity of geometry impacts but also significantly limits the potential for interparticle collision energy, ultimately affecting overall milling efficiency.

4.2.5 Power Draw

Figure 0.11 illustrates the dependence of power consumption on rotational speed for different mill configurations, highlighting the underlying physical mechanisms governing energy demand. At a fixed rotational speed, increasing the fill volume leads to higher power consumption due to the greater mass of the grinding charge, which increases inertial forces and the torque required to rotate the mill. At low fill levels, lifter-free mill designs exhibit an approximately proportional relationship between rotational speed and power draw, reflecting relatively free charge motion and limited resistance to rotation. As the fill volume increases, power consumption reaches a maximum at around 85% of critical speed,

a condition associated with an extended torque arm of the charge as particles are lifted higher before detaching.

Hexagonal-profile mills without lifters consistently require more power than equivalent cylindrical mills under identical operating conditions. This behavior arises from enhanced charge engagement with the mill geometry, where the polygonal vertices promote greater charge lifting and resistance to rotation. Consequently, peak power in hexagonal mills occurs at lower rotational speeds compared to cylindrical designs. The introduction of lifters markedly reduces power consumption upto 40% by improving energy transfer efficiency; lifters promote earlier initiation of cataracting motion—observed at approximately 55% of critical speed even at high fill levels—thereby reducing excessive sliding and energy losses associated with bulk charge motion. In lifter-equipped mills, the rotational speed at which maximum power occurs shifts to higher values with increasing fill level, occurring at approximately 65%, 75%, and 80% of critical speed for fill volumes of 28%, 37%, and 48%, respectively. This shift reflects the increasing dominance of charge inertia and the higher speeds required to mobilize a larger mass effectively.

Figure 0.12 further examines the influence of mill geometry by showing the relationship between power consumption and polygonal side count at a fixed rotational speed of 75% of critical speed. Under identical operating conditions, the rotational speed corresponding to maximum power draw is indicative of optimal comminution efficiency, as it represents the point of most effective energy transfer to the charge. The hexagonal (six-sided) configuration exhibits the highest power demand, up to 20% consistent with its enhanced charge lifting and torque resistance, while mills with higher side counts show progressively lower power consumption as the geometry approaches a cylindrical form and charge–wall interaction becomes smoother.

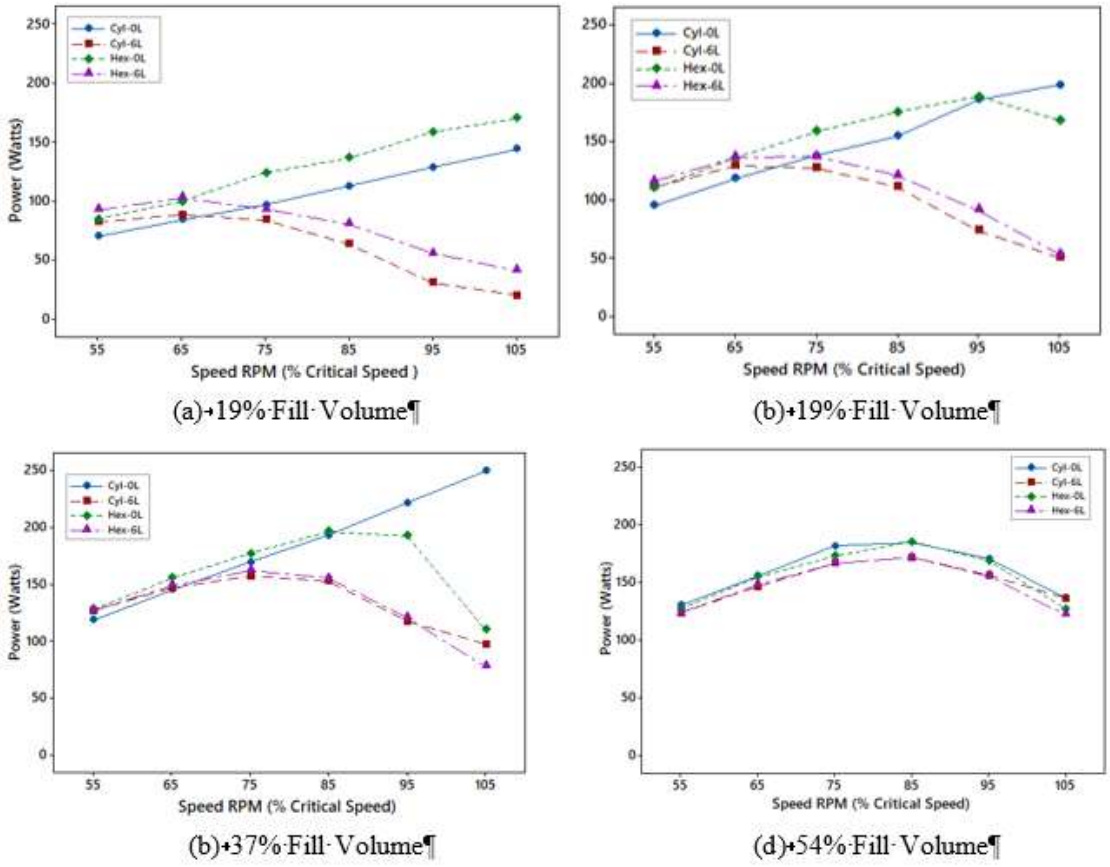

Figure 0.11: Variation in Power between Mill Profiles

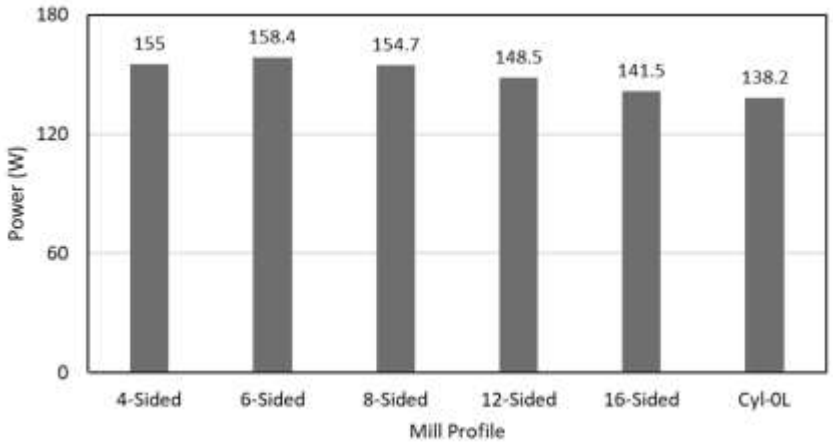

Figure 0.12: Effect of Number of Polygon Sides on Power Draw

A robust correlation (Pearson's r = 0.99) was observed between power consumption and interparticle collision energy at low fill volumes, though this relationship diminished (r = 0.76) at higher fill levels (54%). The attenuation occurs because increased mill loading promotes the formation of a stagnant particle bed that reduces overall charge mobility. Figure 0.13 presents the normalized collision energy-to-power ratio as a function of rotational speed, showing lifter-equipped mills achieve peak efficiency at 85% of critical speed. Comparative analysis revealed that hexagonal liners without lifters demonstrated 12-15% greater power efficiency than equivalent cylindrical configurations. This study established that the mill profile is a dominant factor parameter on power draw at subcritical speeds.

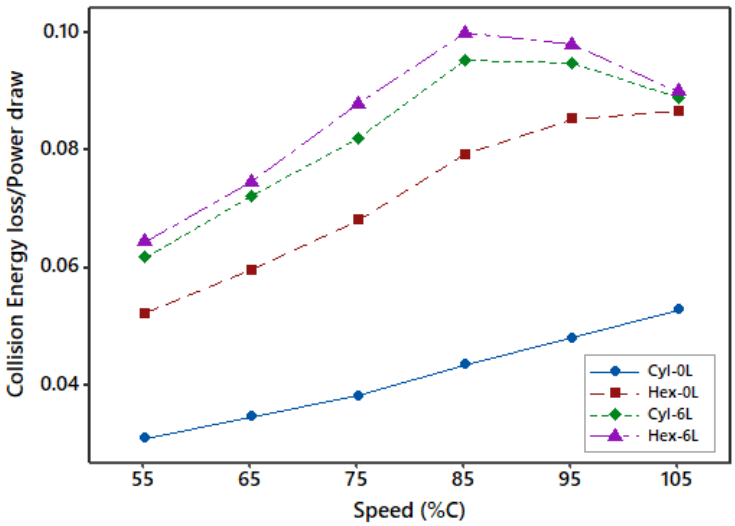

Figure 0.13: Collision Energy-to-Power Ratio against Rotational Speed

4.2.6 Operational Stability

Rotating mills achieve particle size reduction through a dynamic process in which grinding media are lifted from the toe region toward the shoulder of the mill shell, generating impacts that both promote breakage and contribute to the torque required to

drive the mill. DEM simulations conducted at 75% of critical speed and a 28% fill volume revealed pronounced fluctuations in instantaneous torque, reflecting the inherently stochastic nature of particle–particle and particle–wall interactions within the charge. These torque fluctuations, quantified using the standard deviation of the torque signal (Figure 0.13), provide a useful measure of operational stability, with higher variability indicating more irregular charge motion and load transfer.

The results indicate that mill geometry plays a decisive role in torque stability. Square-profile mills exhibited the largest torque variability, which can be physically attributed to the discontinuous charge motion and abrupt changes in contact forces occurring at the sharp vertices. As the number of vertices decreased, charge motion became more continuous, leading to progressively improved operational stability. For hexagonal mills, the addition of lifters reduced torque fluctuations by 7.3%, lowering the standard deviation from 9.6 to 8.9. This stabilizing effect arises because centrally positioned lifters redirect particles toward the toe region, reducing direct, high-intensity impacts on the mill shell and promoting a more uniform load distribution.

In contrast, cylindrical mills without lifters exhibited the most stable operation overall, owing to their smooth geometry and continuous charge motion. However, the introduction of lifters in cylindrical mills led to a slight increase in torque variability, likely due to the added periodic disturbances introduced by lifter–particle interactions. Collectively, these findings highlight the significant impact of mill geometry and lifter configuration on both the efficiency and stability of grinding operations, demonstrating that design features that enhance charge control can substantially mitigate torque fluctuations while maintaining effective comminution.

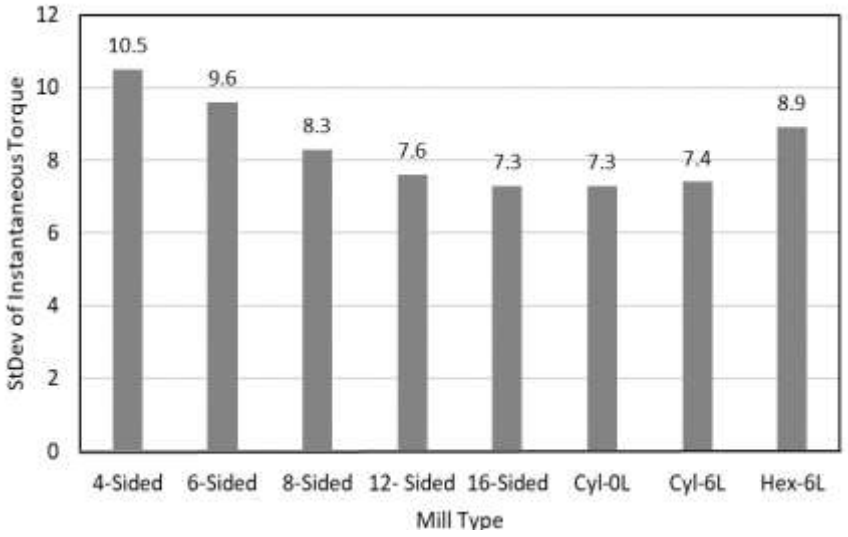

Figure 0.14: Standard Deviation of Torque of Mills

4.2.7 Wear Analysis

During modeling of wear, it was observed that using smaller spheres provided a more accurate particle shape, though at the cost of increased computational demand. On the other hand, using larger spheres simplified the geometry, reducing computational load but sacrificing some precision. After a series of trials, a balanced configuration was achieved using six identical spheres, each with a diameter of 3 mm. This setup effectively replicated the irregular form of the sample rock while maintaining manageable computational requirements. During validation, it was noted that lifting speeds exceeding 0.05 m/s caused the granular pile to collapse, compromising the test. Therefore, the material was dispensed vertically at a controlled speed of 0.5 m/s onto a leveled surface. After lifting the cylinder, a stable pile was formed. The wear constant of $7.48^{-08}\ pa^{-1}$ obtained through iterative simulation showed close agreement with the experimentally determined value. In this study, this wear constant was identified as providing a response that closely replicates the experimental results.

The Archard wear model was applied to estimate abrasive wear depth for both cylindrical and polygonal rotating mills. The study also examined the influence of lifters and

rotational speed on wear behaviour. Wear patterns differed markedly between the two geometries without lifters, as shown in Figure 0.15. The cylindrical profile without lifters exhibited relatively uniform wear, with minimal depth accumulation, due to its smooth surface, which promoted consistent particle sliding. In contrast, the polygonal (hexagonal) profile displayed nonuniform wear concentrated around the vertices. These vertices altered the material flow by reducing particle sliding and increasing energy transfer between the charge and the liners. As a result, the hexagonal geometry without lifters experienced less abrasive action, suggesting that wear resistance can be improved by incorporating slightly thicker corners or by replacing sharp polygonal edges with truncated or rounded geometries.

An increase in rotational speed caused higher material flow rates over both liner profiles, producing an almost linear rise in wear. However, despite this increase, the hexagonal profile consistently experienced less wear than the cylindrical profile at all simulated speeds. On average, the polygonal geometry exhibited 17.9% less wear, primarily due to reduced slip caused by the presence of vertices. Introducing lifters on both profiles further decreased wear at all rotational speeds, as illustrated in Figure 0.16. Lifters reduced particle slip across the liner surface, thereby limiting abrasive interactions. Increasing the number or height of lifters eventually caused particle entrapment between lifters, and these trapped particles acted as a protective layer shielding the liners from direct contact with the flowing charge.

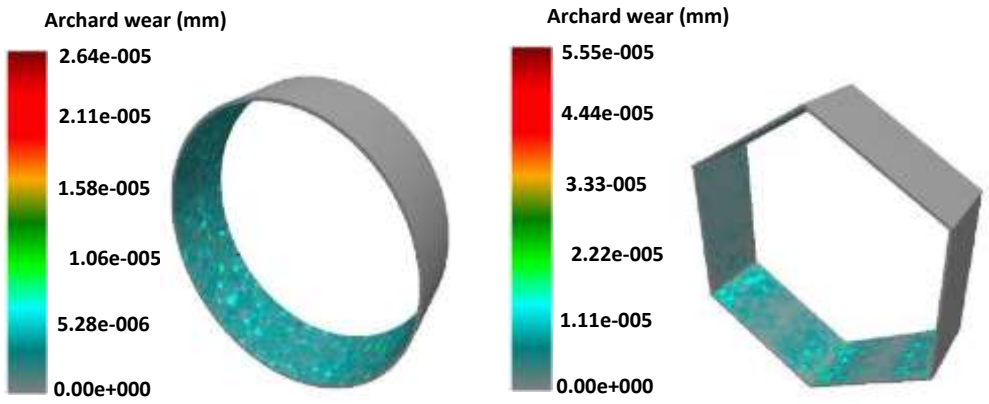

(a) Cylindrical profile (b) Hexagonal mill

Figure 0.15: Archard Wear on Cylindrical and Hexagonal Mills

The hexagonal mill lifters experienced a 34.7% higher wear rate compared to the cylindrical profile with lifters. For the hexagonal liner profile, the vertices induced substantial fluctuations in both the material's mean velocity and wear patterns. Incorporating lifters at the midpoint of each longitudinal face significantly altered particle dynamics, resulting in a pronounced decrease in impact forces exerted on the mill shell. At the shoulder region, centrally positioned lifters on the hexagonal faces propelled a portion of the grinding media to elevated trajectories, thereby expanding the charge volume, while the remaining media maintained conventional cascading motion. The lifted particles would later fall on the toe position and interact with particles that had been cascading, thereby reducing particle-geometry interaction. At the toe position, lifters on the hexagon profile trapped media particles and reduced the speed of the cascading particles that would have moved at high speed to the mill wall. The combined effect of the lifter at the shoulder position, which created a dispersed charge inside the mill, reducing particle geometry interaction, and the effect of the lifter at the toe position, which trapped particles, limiting their acceleration to the mill wall, led to an overall reduction in relative wear of the mill for a hexagonal drum with lifters. The cylindrical mill with lifters experienced the least wear, peaking at 85% and then declining due to particle flow behavior. The cylindrical surface of the mill locked more of the particles up to the shoulder

position, unlike the hexagon mill, which produced increased particle interaction along the mill wall.

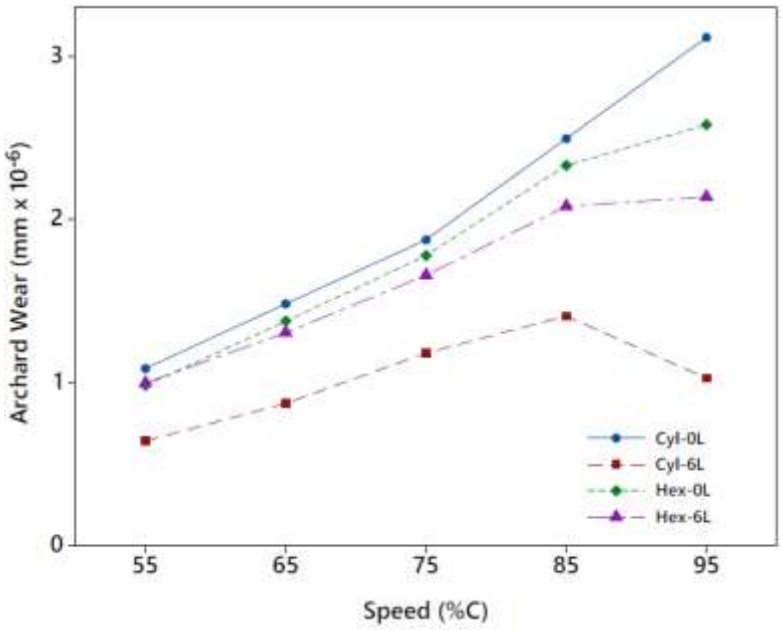

Figure 0.16: Variation of Wear on Various Mill Geometries

4.3 Ore Characterization

The field specimens of copper ore were massive and light green, with a dull luster phaneritic texture. A sample result of petrographic studies is shown in

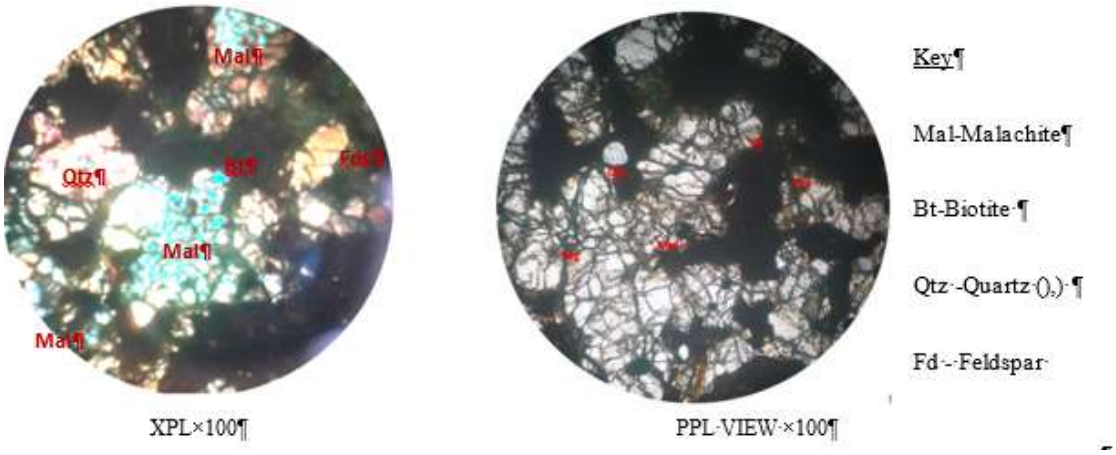

Figure 0.17. The specimen shows the presence of biotite that appeared stained with a secondary mineral, preferably malachite; it appears altered. The groundmass consists of quartz, feldspar, and biotite, among other minerals. Malachite is a copper-bearing mineral characterized by a green color. Chemical compositions obtained using X-ray Fluorescence Spectroscopy (XRF) and analyzed using Bruker Esprit 1.9 software are shown in Table 0.3.

Table 0.3: Chemical Composition of Copper Ore (wt. %).

MgO	Al_2O_3	SiO_2	CaO	Fe	Cu
7.84	15.20	52.37	9.43	7.57	4.76

The results represent the average values of three samples obtained randomly during crushing. The percentage composition of copper, 4.76%, confirms the presence of copper in the ore. The ore-bearing mineral is classified as malachite from physical observation, petrographic studies, and chemical composition analysis. The area of study is within the Mozambique belt, mainly covered by rocks of the basement system (Wairimu, 2012). Chemical analysis indicates the local malachite ore contains 3-8% copper content, which aligns with the compositional range reported for the Mithikwani deposit.

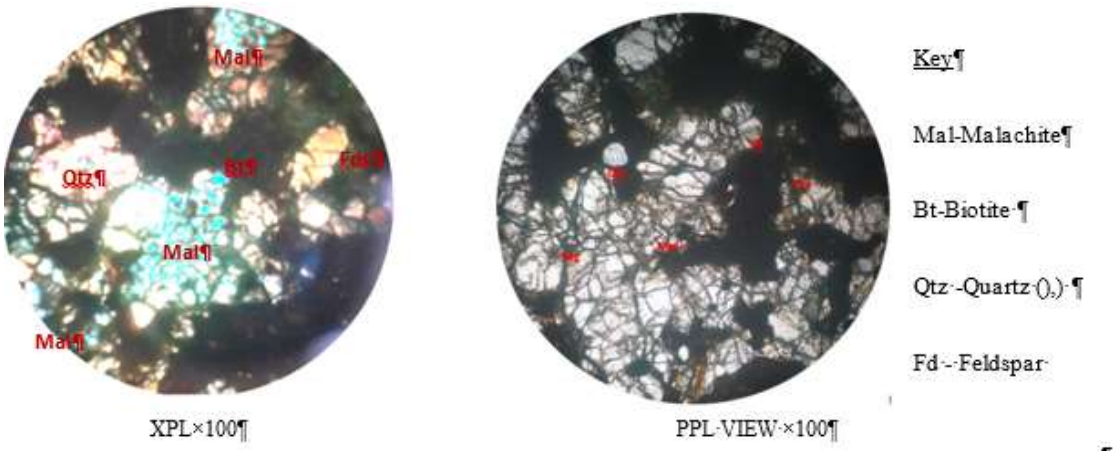

Figure 0.17: Photomicrograph of Thin Section Samples

The elemental contents of gold ores obtained through X-ray Fluorescence are shown in Table 0.4. The Osiri and Ndiwa ores contain silica and alumina as the major compositions. The composition of FeO was significant for the Osiri ore. The other oxide compounds were detected like K_2O with lower percentages. This resulted in the determination that silicate minerals like quartz, feldspar, and clay are the primary minerals, along with iron oxide found in the Osiri and Ndiwa samples. The Lolgorean ore is dominated by silica, leading to the conclusion that the ore is predominantly quartz mineral. A sample of Lolgorean ore shown in Figure 0.18 was massive, off-white to cream in color with a medium-grained texture. It was colorless in PPL, with no alteration. it has anhedral to irregular grains and is high in grey white interference colors

Table 0.4: Percentage Mineralogical Composition of the Gold Ore Samples

Ore	**Notation**	Al_2O_3	SiO_2	K_2O	FeO	Au
Osiri	S	9.497	72.632	3.644	10.788	0.013
Lolgorien	L	0.000	92.498	0.15	1.621	0.018
Ndhiwa	N	13.205	76.217	4.364	2.213	0.014

According to geological analyses of the mining sites, gold is primarily associated with quartz veins. The relative proportions of the various phases exhibit significant variability among the distinct components. This indicates that the identified components are inherently different and are expected to demonstrate divergent behaviors during the processes of comminution.

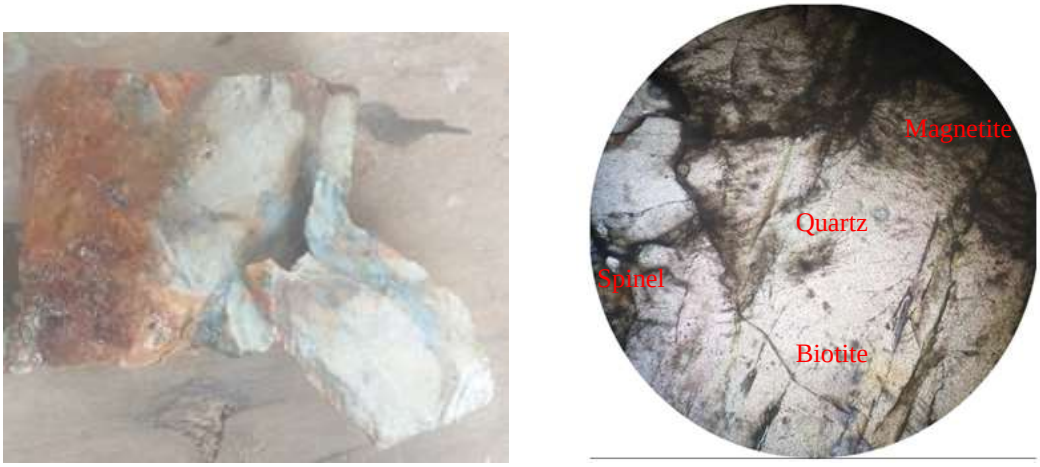

FIELD SAMPLE PPL VIEW ×100

Figure 0.18: Lolgorien Field Sample and PPL View

4.4 Grinding Kinetics

Grinding kinetics describe the breakage properties consisting of the breakage distribution function and the breakage rate of the particles being studied. The breakage properties of copper ore and gold ore are discussed. The cylindrical mill profile with six lifters is used to carry out the experiments. The mill had a high index of collision energy /power draw, the lowest Archard wear, and high operational stability.

4.4.1 Breakage Characteristics of Copper Ore

The percentage mass retained on the top sieve was plotted on a semi-logarithmic (log–linear) scale against grinding time (t) for all mono-sized feed fractions to determine the specific breakage rate (S_i), as illustrated in Figure 0.19. Under first-order breakage kinetics, the slope of the linear regression fitted to each dataset corresponds to S_i. The resulting specific breakage rates for the individual size fractions are summarized in Table 4.5. In sieve analysis, a negative (–) sign denotes particles passing through a given sieve aperture, whereas a positive (+) sign represents particles retained on that sieve size. The results show a clear dependence of S_i on particle size. The specific breakage rate increased with

increasing feed size, attaining a maximum value of 2.892 min^{-1} at a particle size of 2.000 mm. Beyond this size, a pronounced decline in S_i was observed. This behavior reflects the underlying breakage mechanics within the mill. For smaller particles, insufficient impact energy and cushioning effects reduce the probability of fracture, while for excessively large particles, the grinding media are unable to effectively nip and fracture the particles due to geometric constraints and higher particle strength. Consequently, an optimum feed size exists at which the energy transfer from the grinding media to the particles is maximized.

The peak S_i value therefore defines two distinct breakage regimes: a fine-particle regime dominated by inefficient energy utilization, and a coarse-particle regime where particles are too large or too strong to be effectively broken by the prevailing ball size distribution. Under the investigated operating conditions, the particle size corresponding to the maximum S_i was identified as the optimum feed size for efficient breakage. The experimentally determined S_i values for the individual mono-sized fractions were subsequently fitted using nonlinear regression to a size-dependent breakage rate model equation (0-14). The estimated model parameters, which characterize the variation of specific breakage rate with particle size, are presented in Table 0.6.

Table 0.5: Specific Breakage Function Values for Feed Size Classes

Classes mono- sized malachite materials (mm)	**Selection function values (S_i) (1/minute)**
–3.350+2.360	1.345
–2.360+2.000	2.441
–2.000+1.700	2.892
–1.700+1.400	0.534
–1.400+1.000	0.055

Table 0.6: Specific Breakage Function Parameters

Classes mono-sized malachite materials (mm)	a	α	μ	Λ
–3.350+2.360	1.00	0.62	3.47	1.73
–2.360+2.000	1.02	0.70	4.71	1.57

–2.000+1.700	1.56	0.87	5.01	2.00
–1.700+1.400	0.41	2.36	4.97	2.30
–1.400+1.000	0.51	2.34	4.63	2.30

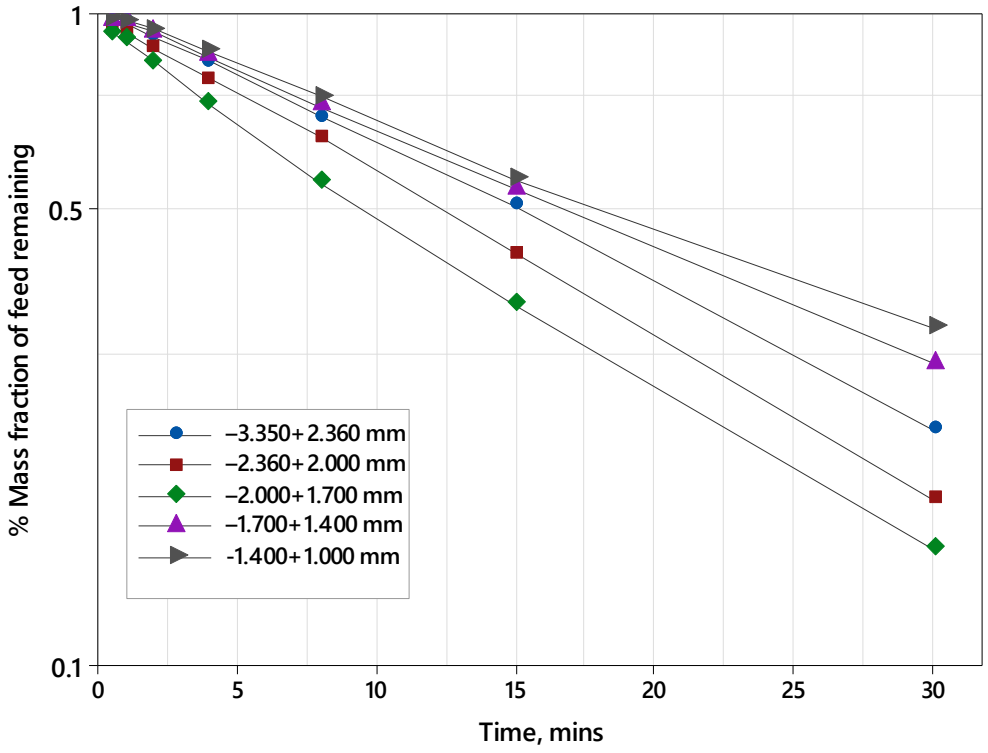

Figure 0.19: First Order Grinding Plots for Malachite Ore

Primary breakage function parameters were calculated for short grinding cycles. All the feed materials were considered to be normalizable for simulation purposes. Figure 0.20 illustrates the cumulative breakage distribution functions for malachite ore across multiple feed size fractions. The breakage function parameters (β, γ, and Φ) were determined through Equation (0-17) and are presented in Table 0.7. The calculated specific breakage parameters (α, Λ, γ and μ) and breakage parameters (β, γ, and ∅) were used to reproduce the size distribution of the grinding products

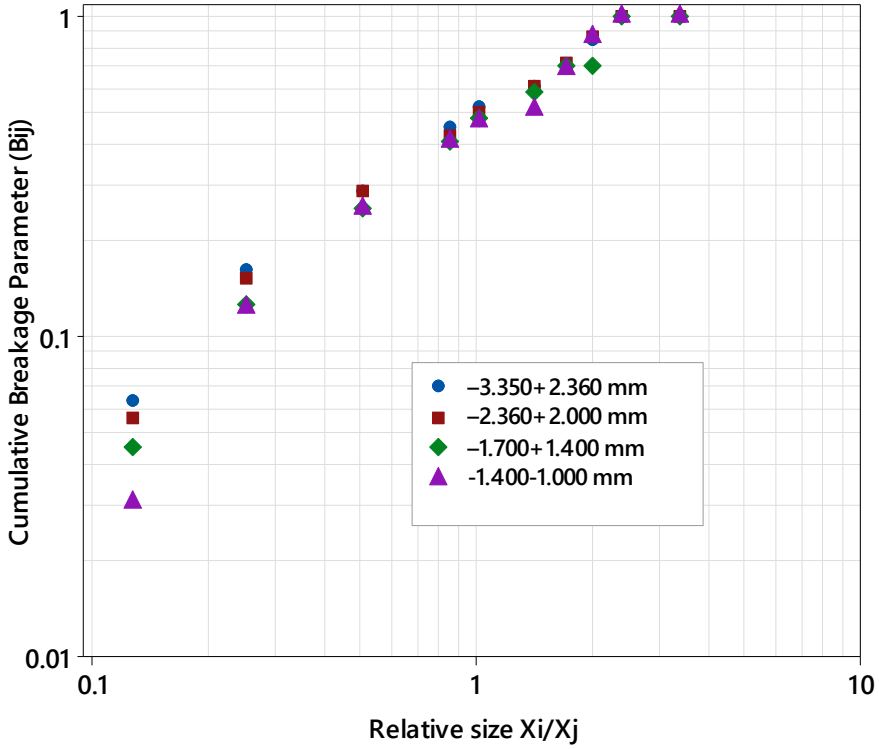

Figure 0.20: Cumulative Breakage Function of Malachite Ore

Table 0.7: Primary Breakage Distributions for Various Feed Sizes

Classes mono-sized malachite materials (mm)	β	γ	$\emptyset$
–4.750+3.350	5.5	0.85	0.81
–3.350+2.360	5.3	0.85	0.81
–2.360+2.000	5.18	0.86	0.82
–2.000+1.700	5.11	0.96	0.82
–1.700+1.400	5.49	0.98	0.83
Average	5.13	0.9	0.82

Figure 0.21 shows the measured and predicted size distributions for all milling products. The RMSE between predicted and actual PSD was 2.4%, indicating good agreement. This enabled the kinetics model to be verified and provided evidence that the Selection and Breakage Functions parameters could be applied to a continuous mass balance.

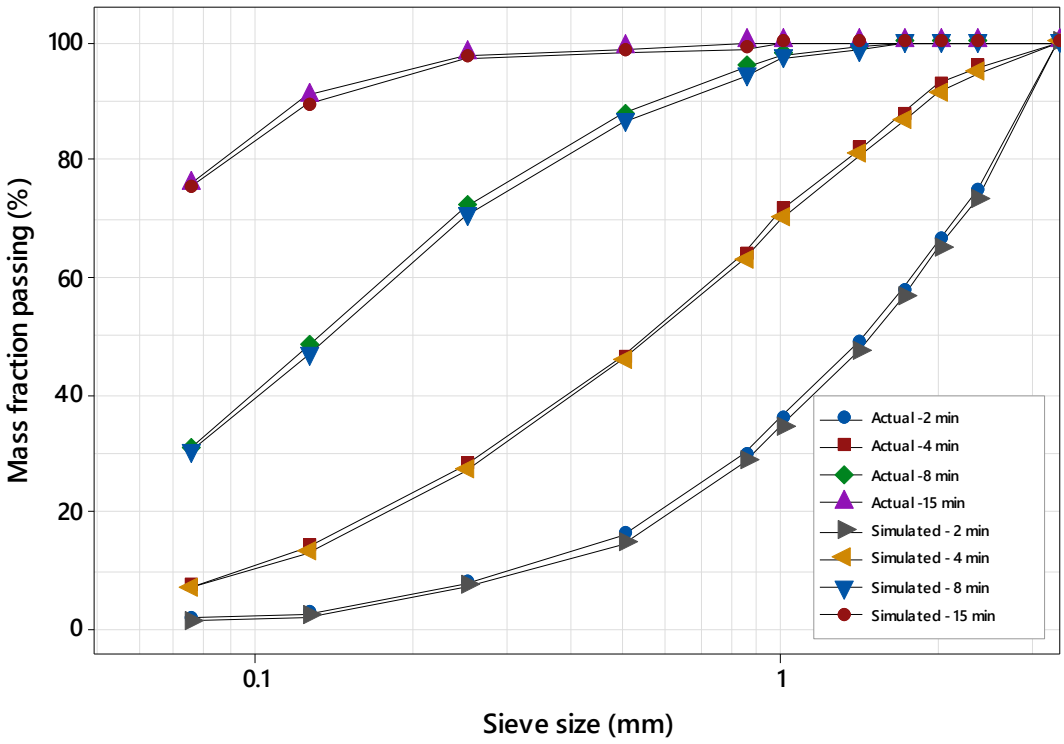

Figure 0.21: Predicted and Measured Particle Size Distributions

4.4.2 Blending of Gold Ores

The initial breakage plots for the three types of ores and their respective blends are presented in Figure 0.22. Through linear regression analysis of the experimental data, it has been determined that the breakage process of the fractions adheres to a first-order kinetic model. The slopes of these plots allowed for the calculation of the specific breakage rates. Based on the plot outcomes, it was found that the Lolgorean (L) ore exhibits the highest hardness due to high quartz content $SiO_2 = 72.632\%$wt, followed by the Osiri (S) ore, with the Ndhiwa (N) ore being the softest of the three. Figure 0.23 shows the average and the actual selection function for binary and tertiary gold ore blends. The binary blends composed of Osiri and Ndhiwa exhibit noteworthy synergistic breakage behavior ($0.358\, min^{-1}$), that resulted in minimal variations in particle size distribution between them. In contrast, other blends are largely influenced by the more complex and

harder Lolgorean ore, which overshadows the grinding characteristics of the softer ores. Even in the tertiary blend, the influence of Lolgorean ore remains predominant ($0.319\ min^{-1}$).The attributes of grindability in binary ores are significantly affected by the mineralogical properties inherent to the ores themselves. When the proportion of the harder ore is excessively high, the overall hardness of the blend escalates. This heightened hardness necessitates extended grinding times and results in increased consumption of grinding balls. This can also be attributed to the cushioning effect of soft ore limiting breakage of the hard ore.

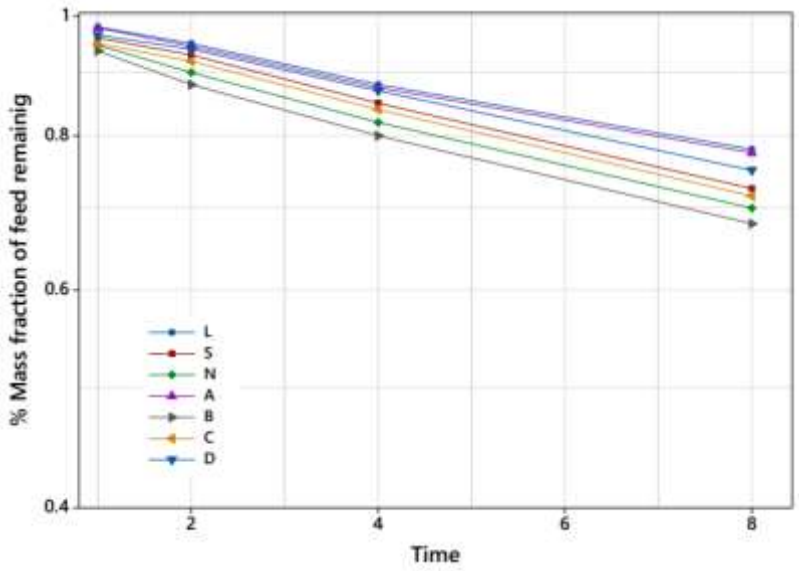

Figure 0.22: First-Order Breakage Plots for Gold Ore Size Fractions

As the milling process continues, the harder particles are gradually reduced in size, allowing the softer particles to become more prevalent in the upper size intervals of the resulting material. The initial grinding rate is typically slow but gradually stabilizes following the relative mechanical properties of both soft and hard components in the feed mixture. When an inverse relationship governs these properties, the breakage rate initially peaks due to the structural integrity of harder particles. However, prolonged milling leads to progressive rate reduction as softer constituents are preferentially comminuted, eventually resulting in selective accumulation of more resistant particles.

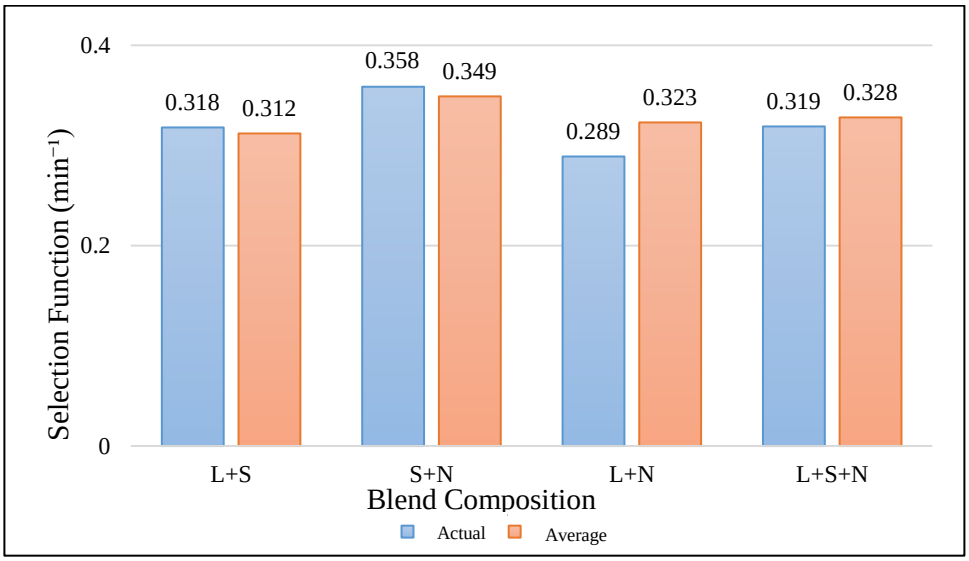

Figure 0.23: Selection Function for Binary and Tertiary Gold Ore Blends

CHAPTER FIVE

CONCLUSIONS AND RECOMMENDATIONS

5.1 Conclusion

The Discrete Element Method (DEM) simulation method was utilized to analyze the behavior of media particles within both polygonal and cylindrical-shaped rotating mills. A narrow set of parameters was used to carry out grinding tests. The following conclusions were drawn;

i. The developed DEM model demonstrated strong predictive capability, achieving a high Pearson correlation coefficient (>0.9) between simulated and measured responses. Quantitatively, the predictions showed excellent agreement with experimental data, with a root mean square error (RMSE) of 2.3 W for power draw and 2.1° for shoulder angle. These low error values confirm that the model is capable of accurately capturing both the dynamic charge motion and the energy consumption characteristics of the mill.

ii. The introduction of lifters substantially enhanced the mechanical performance and wear characteristics of both cylindrical and polygonal mill geometries. Lifters promoted more effective charge lifting, reduced slipping, and improved impact–shear interactions, which collectively enhanced energy utilization. Across all simulated conditions, mills equipped with lifters achieved a 27–40% reduction in Archard abrasive wear rate, indicating significant improvement in liner longevity. Additionally, lifters improved energy efficiency by facilitating better energy transfer between the mill and the particle bed.

iii. Among the mill configurations tested, the cylindrical mill equipped with lifters delivered the most stable and wear-resistant performance. This geometry displayed the lowest wear accumulation less by about 30% and the most consistent charge motion behaviour. The use of lifters on the cylindrical profile ensured predictable and uniform trajectories, minimized excessive particle–liner sliding,

and resulted in enhanced operational stability with a standard deviation of toque of 7.4. Overall, the cylindrical mill with lifters emerged as the most robust design, offering the best combination of efficiency, reduced wear, and smooth mill operation.

iv. Analysis of mono-sized malachite classes in the size range −4.750 + 3.350 mm to −1.700 + 1.400 mm yielded consistent breakage function parameters, with average values of $\beta = 5.13$, $\gamma = 0.90$, and $\varphi = 0.82$. The relatively low variability of these parameters across the investigated size classes indicates stable breakage behaviour for malachite within the studied operating regime. The optimum upper particle size of copper ore was found to be 2.00 mm under the present milling operating conditions. This led to the conclusion that the average breakage function values for malachite obtained can be used in scale up design of ore processing plants.

v. Study into the grinding characteristics of gold ore blends revealed a trend where the overall grindability of the blend tended to lean more closely with that of the harder ore present in the mixture. While blending is often done to average out ore quality, mixing a very hard ore with a very soft one can be antagonistic. The soft ore can act as a protective buffer, lowering the overall breakage efficiency and making the grinding process less effective and more costly than anticipated. This underscores the need for competence-based blending strategies, not just grade-based ones.

5.2 Recommendations for Future Work

The outcome of this work is a guideline for future studies aimed at improving ball milling. It is crucial to scale up the results for industrial-scale operations. Therefore, the following recommendations should be considered:

i. Mineralogical Characterization: A thorough mineralogical characterization of the ground product is essential for gaining a comprehensive understanding of its elemental composition. This analysis is crucial in informing the design of mineral processing units and enhancing insights into their operational performance.

ii. Breakage Properties Evaluation: The evaluation of the breakage properties of binary and tertiary blends of gold ore was conducted using a dry processing method. To better predict their behavior in a typical ball milling circuit, the adoption of a wet continuous process would prove advantageous.

iii. Wear Model: For a more precise prediction of mill wear, it is important to develop a wear model that integrates both impact and abrasion factors. This study primarily focused on the Archard wear model, which emphasizes abrasion, but did not investigate the wear effects of high-energy impacts on mill geometry.

REFERENCES

Adams, G. G., & Nosonovsky, M. (2000). Contact modeling — forces. *Tribology International*, *33*, 431–442. www.elsevier.com/locate/triboint

Amadi, A. H., Mohyaldinn, M., Abduljabbar, A., Ridha, S., Avilala, P., & Owolabi, G. T. (2024). Wear Analysis of NiTi Sand Screens Using Altair Discrete Element Method. *Materials*, *17*(2). https://doi.org/10.3390/ma17020281

AmanNejad, M., & Barani, K. (2020). Effects of Ball Size Distribution and Mill Speed and Their Interactions on Ball Milling Using DEM. *Mineral Processing and Extractive Metallurgy Review*, 1–6. https://doi.org/10.1080/08827508.2020.1781630

Anticoi, H., Guasch, E., Hamid, S. A., Oliva, J., Alfonso, P., Garcia-Valles, M., Bascompta, M., Sanmiquel, L., Escobet, T., Argelaguet, R., Escobet, A., de Felipe, J. J., Parcerisa, D., & Peña-Pitarch, E. (2018). Breakage function for HPGR: Mineral and mechanical characterization of tantalum and tungsten ores. *Minerals*, *8*(4). https://doi.org/10.3390/min8040170

Austin, L. G. (1973). A commentary on the Kick, Bond and Rittinger laws of grinding. *Powder Technology*, *7*(6), 315–317. https://doi.org/10.1016/0032-5910(73)80042-7

Austin, L. G., & Bagga, P. (1981). An analysis of fine dry grinding in ball mills. *Powder Technology*, *28*(1), 83–90. https://doi.org/10.1016/0032-5910(81)87014-3

Barani, K., & Balochi, H. (2016). First-order and second-order breakage rate of coarse particles in ball mill grinding. *Physicochem. Probl. Miner. Process*, *52*(1), 268–278. https://doi.org/10.5277/ppmp160123

Barreto, M. L., Schein P., Hinton, J., & Hruschka, F. (2018). Economic Contributions of Artisanal and Small-Scale Mining in Kenya: Gold and Gemstones. In *27 November* (Issue January). Pact Global UK.

http://blogs.lse.ac.uk/internationaldevelopment/2018/04/13/the-economic-contributions-of-artisanal-small-scale-mining-in-kenya-gold-and-gemstones/

Barthel, E. (2008). Adhesive elastic contacts – JKR and more. *Journal of Physics D: Applied Physics*, *41*. https://doi.org/10.1088/0022-3727/41/16/163001>

Beakawi Al-Hashemi, H. M., & Baghabra Al-Amoudi, O. S. (2018). A review on the angle of repose of granular materials. *Powder Technology*, *330*, 397–417. https://doi.org/10.1016/j.powtec.2018.02.003

Boemer, D., & Ponthot, J. P. (2017a). A generic wear prediction procedure based on the discrete element method for ball mill liners in the cement industry. *Minerals Engineering*, *109*, 55–79. https://doi.org/10.1016/j.mineng.2017.02.014

Boemer, D., & Ponthot, J. P. (2017b). DEM modeling of ball mills with experimental validation: influence of contact parameters on charge motion and power draw. *Computational Particle Mechanics*, *4*(1), 53–67. https://doi.org/10.1007/s40571-016-0125-4

Boemer, D., & Ponthot, J.-P. (2017c). A generic wear prediction procedure based on the discrete element method for ball mill liners in the cement industry. *Minerals Engineering*, *109*, 55–79. https://doi.org/10.1016/j.mineng.2017.02.014

Bond, F. C. (1962). Crushing and Grinding calulations. *Allis-Chalmers*, *07R935C*.

Caibin, W., & Kuangdi, X. (2023). Charge Volume of Grinding Mill. In *The ECPH Encyclopedia of Mining and Metallurgy* (pp. 1–1). Springer Nature Singapore. https://doi.org/10.1007/978-981-19-0740-1_1106-1

Caracal. (2022). *East Africa Gold Production*. file:///C:/Users/user/Downloads/CP002.Caracal-Gold-PLC_Corporate-Presentation_SEPT-2022.pdf

Cayirli, S. (2018). Influences of operating parameters on dry ball mill performance. *Physicochemical Problems of Mineral Processing*, *54*(3), 751–762. https://doi.org/10.5277/ppmp1876

Chhabra, R., & Shankar, V. (2019). Particle Size Reduction and Enlargement. In *Coulson and Richardson's Chemical Engineering*. Susan Dennis. https://doi.org/10.1016/B978-0-08-101098-3.00006-8

Chimwani, N., & Bwalya, M. M. (2020). Exploring the end-liner forces using dem software. *Minerals*, *10*(12), 1–12. https://doi.org/10.3390/min10121047

Cleary, P. W., Morrisson, R., & Morrell, S. (2003). Comparison of DEM and experiment for a scale model SAG mill. *International Journal of Mineral Processing*, *68*(1–4), 129–165. https://doi.org/10.1016/S0301-7516(02)00065-0

Cleary, P. W., & Owen, P. (2019). Effect of operating condition changes on the collisional environment in a SAG mill. *Minerals Engineering*, *132*(June), 297–315. https://doi.org/10.1016/j.mineng.2018.06.027

Cummins, S. J., Thornton, C., & Cleary, P. W. (2012). Contact force models in inelastic collisions. *Ninth International Conference on CFD in the Minerals and Process Industries CSIRO, Melbourne, Australia*, 10–12. http://www.cfd.com.au/cfd_conf12/PDFs/175CUM.pdf

Datta, A., & Rajamani, R. K. (2002). A direct approach of modeling batch grinding in ball mills using population balance principles and impact energy distribution. *International Journal of Mineral Processing*, *64*(4), 181–200. https://doi.org/10.1016/S0301-7516(01)00044-8

Di Maio, F. P., & Di Renzo, A. (2005). Modelling particle contacts in distinct element simulations: Linear and non-linear approach. *Chemical Engineering Research and Design*, *83*(11 A), 1287–1297. https://doi.org/10.1205/cherd.05089

Di Renzo, A., & Di Maio, F. P. (2004). Comparison of contact-force models for the simulation of collisions in DEM-based granular flow codes. *Chemical Engineering Science*, *59*(3), 525–541. https://doi.org/10.1016/j.ces.2003.09.037

Doan, T., Indraratna, B., Nguyen, T. T., & Rujikiatkamjorn, C. (2025). *A Coupled CFD-DEM Approach to Examine Clogging Behaviour of Granular Medium by Fines* (pp. 1–9). https://doi.org/10.1007/978-981-97-8233-8_1

Dunne, R. C., Kawatra, S. K., & Young, C. A. (2019). *SME Mineral Processing, and Extractive Metallurgy Handbook.* (Vol. 2). Society for Mining, Metallurgy, and Exploration (SME).

Ebadnejad, A. (2016). Investigating of the effect of ore work index and particle size on the grinding modeling of some copper sulphide ores. *Journal of Materials Research and Technology*, *5*(2), 101–110. https://doi.org/10.1016/j.jmrt.2015.05.002

Fang, H., Ji, X., Yang, J., Yang, Y., Ji, T., & Wei, C. (2024). Adaptive control method and experimental study of cone crusher based on aggregate online detection. *Physicochemical Problems of Mineral Processing*, *60*(3). https://doi.org/10.37190/PPMP/188759

Foszcz, D., Krawczykowski, D., Gawenda, T., Kasińska-Pilut, E., & Pawlos, W. (2018). Analysis of process of grinding efficiency in ball and rod mills with various feed parameters. *IOP Conference Series: Materials Science and Engineering*, *427*(1). https://doi.org/10.1088/1757-899X/427/1/012031

Fuerstenau, D. W., Kapur, P. C., & De, A. (2003). Modeling breakage kinetics in various dry comminution systems. *KONA Powder and Particle Journal*, *21*(March), 121–132. https://doi.org/10.14356/kona.2003015

Gao, D., & Sun, J. (2003). Using DEM in Particulate Flow Simulations. *Cdn.Intechopen.Com*, 29–50. https://doi.org/10.5772/26681

Gilardi, G., & Sharf, I. (2002). Literature survey of contact dynamics modelling. *Mechanism and Machine Theory*, *37*, 1213–1239. https://doi.org/0094-114X/02/$

Gottheil, J. (2021). *Modelling Mineral Liberation of Ore Breakage to Improve the Overall Efficiency of Mining Operations*. University of Ottawa.

Govender, I., Powell, M. S., & Nurick, G. N. (2001). 3D particle tracking in a mill: A rigorous technique for verifying DEM predictions. *Minerals Engineering*, *14*(10), 1329–1340. https://doi.org/10.1016/S0892-6875(01)00147-9

Guo, Q., & Xia, H. (2023). A review of the Discrete Element Method/Modelling (DEM) in agricultural engineering. *Journal of Agricultural Engineering*. https://doi.org/10.4081/jae.2023.1534

Gupta, V. K. (2022). Population balance modeling approach to determining the mill diameter scale-up factor: Consideration of size distributions of the ball and particulate contents of the mill. *Powder Technology*, *395*, 412–423. https://doi.org/10.1016/j.powtec.2021.09.059

Higashitani, K., Makino, H., & Matsusaka, S. (2020). *Powder Technology Handbook* (4th ed.). Taylor & Francis Group, LLC.

Hirosawa, F., & Iwasaki, T. (2021). Dependence of the dissipated energy of particles on the sizes and numbers of particles and balls in a planetary ball mill. *Chemical Engineering Research and Design*, *167*, 84–95. https://doi.org/10.1016/j.cherd.2020.12.024

Hocking, M. B. (2005). Ore Enrichment and Smelting of Copper. *Handbook of Chemical Technology and Pollution Control*, 391–420. https://doi.org/10.1016/b978-012088796-5/50016-8

Hu, J., Rangel, R. L., Kisuka, F., Zhang, L., Yin, S., & Wu, C. Y. (2024). DEM analysis of heat generation and transfer during granular flow in a rotating drum. *Chemical Engineering Journal*, *499*. https://doi.org/10.1016/j.cej.2024.155945

Huang, P., Ding, Y., Wu, L., Fu, S., & Jia, M. (2019). A novel approach of evaluating crushing energy in ball mills using regional total energy. *Powder Technology*, *355*, 289–299. https://doi.org/10.1016/j.powtec.2019.07.050

Hukki, R. T. (1962). Proposal for a solomnic settlement between the theories of von Rittinger, Kick and Bond. *Transactions of the AIME*, *223*, 403–408.

Johnson, K. L. (1985). Contact mechanics. In *CAMBRIDGE UNIVERSITY PRESS* (1st ed.). Press Syndicate of the University of Cambridge. http://linkinghub.elsevier.com/retrieve/pii/0301679X8690085X

Kalman, H. (2000). Particle Breakage and Attrition. *KONA Powder and Particle Journal*, *18*, 108–120. http://www.kona.or.jp/search/18_108.pdf

Kanda, Y., Simodaira, K., Kotake, N., & Abe, Y. (1999). Experimental study on the grinding rate constant of a ball mill: Effects of feed size and ball diameter. *KONA Powder and Particle Journal*, *17*(May), 220–226. https://doi.org/10.14356/kona.1999030

Kimani, H. W., Kimotho, J. K., & Mutua, J. (2024). Investigation of Liner Wear on Different Ball Mill Profiles Using Discrete Element Method. *Open Access Journal Journal of Sustainable Research in Engineering*, *8*(1), 68–84.

King, R. P. (2001). *Modeling and Simulation of Mineral Processing Systems*. Butterworth-Heinemann. https://miningandblasting.files.wordpress.com/2009/09/modeling-and-simulation-of-mineral-processing-systems.pdf

Kirsch, S. (2018). DEM Model Calibration for Vertical Filling : Selection of adequate Trials and Handling Randomness. *15th Weimar Optimization and Stochastic Days*, 1–14.

KNBS. (2025). *Economic Survey 2025*.

Kyalo, M. N., Munyerere, I. F., Rop, B., & Maranga, S. M. (2015). Scouring abandoned mines in search for elusive metal (gold) in Kakamega ' s Rosterman area - A case study in Kenya. *Sustainable Research and Innovation (SRI) Conference*, 362–366.

Lee, H., Kim, K., & Lee, H. (2019). Analysis of grinding kinetics in a laboratory ball mill using population-balance-model and discrete-element-method. *Advanced Powder Technology*, *30*(11), 2517–2526. https://doi.org/10.1016/j.apt.2019.07.030

Li, P., Ucgul, M., Lee, S.-H., & Saunders, C. (2020). A new approach for the automatic measurement of the angle of repose of granular materials with maximal least square using digital image processing. *Computers and Electronics in Agriculture*, *172*, 105356. https://doi.org/10.1016/j.compag.2020.105356

Liu, J., Zhang, P., & Wang, Y. (2025). Research on Integration Methods for Particle Position Updating in the Discrete Element Method. *Processes*, *13*(12), 4024. https://doi.org/10.3390/pr13124024

Magalhães, D. C. R. (2013). *Mechanistic modelling of semi-autogenous grinding* [Universidade Federal do Rio de Janeiro]. http://pct.capes.gov.br/teses/2013/31001017031P0/TES.PDF

Martelli, S., & Di Nunzio, P. E. (2025). Powder Ball Milling: An energy balance approach to particle size reduction. *Journal of Materials Research*, *2*(40), 292–308.

Matsanga, N., Nheta, W., & Chimwani, N. (2023). A Review of the Grinding Media in Ball Mills for Mineral Processing. *Minerals*, *13*(11), 1373. https://doi.org/10.3390/min13111373

Mei, X., Du, H., Yao, W., & Liu, A. (2025). Investigating the Wear Evolution and Shape Optimize of SAG Mill Liners by DEM-FEM Coupled Simulation. *Minerals*, *15*(11). https://doi.org/10.3390/min15111155

Mindlin, R. D., & Deresiewicz, H. (1953). Elastic Spheres in Contact Under Varying Oblique Forces. *Journal of Applied Mechanics*, *20*(3), 327–344. https://doi.org/10.1115/1.4010702

Ministry of Mining, K. (2016). *Mining and Minerals Policy- The Popular Version*.

Mishra, B. K. (2003). A review of computer simulation of tumbling mills by the discrete element method. *International Journal of Mineral Processing*, *71*(1–4), 95–112. https://doi.org/10.1016/S0301-7516(03)00031-0

Morrell, S. (1996). Power draw of wet tumbling mills and its relationship to charge dynamics - part 1. a continuum approach to mathematical modelling of mill power draw. *Transactions of the Institution of Mining and Metallurgy. Section C. Mineral Processing and Extractive Metallurgy*, *105*(Jan), C43–C53.

Moys, M. H. (1993). A model of mill power as affected by mill speed, load volume, and liner design. *J. S. Afr. Fnst. Min. Metall*, *93*(6), 135–141. https://www.saimm.co.za/Journal/v093n06p135.pdf

Muhayimana, P. (2019). *Process Optimization of a Small Scale Ball Mill for Mineral Processing Using Discrete Element Method*. Jomo Kenyatta University of Agriculture and Technology.

Muhayimana, P., Kimotho, J. K., Kyalo, M. N., & Ndiritu, H. M. (2018). Effects of Lifter Configuration on Power Consumption of Small Scale Ball Mill. *Open Access Journal Journal of Sustainable Research in Engineering*, *4*(4), 171–183.

Napier-Munn, T. J., Morrell, S., Morrison, R. D., & Kojovic, T. (1999). Ball mills. In *Mineral comminution circuits, their operation and optimization* (pp. 206–229). Julius Kruttschnitt Mineral Research Centre, University of Queensland.

O 'sullivan, C. (2008). Particle-Based Discrete Element Modelling: A Geomechanics Overview. *The 12th International Association for Computer Methods and Advances in Geomechanics (IACMAG)*, 498–505.

Otsubo, M., O'Sullivan, C., & Shire, T. (2017). Empirical assessment of the critical time increment in explicit particulate discrete element method simulations. *Computers and Geotechnics*, *86*, 67–79. https://doi.org/10.1016/j.compgeo.2016.12.022

Pereira, L., Schach, E., Tolosana-Delgado, R., & Frenzel, M. (2023). All About Particles: Modelling Ore Behaviour in Mineral Processing. *Elements*, *19*(6), 359–364. https://doi.org/10.2138/gselements.19.6.359

Petrakis, E., Stamboliadis, E., & Komnitsas, K. (2017). Identification of optimal mill operating parameters during grinding of quartz with the use of population balance modeling. *KONA Powder and Particle Journal*, *2017*(34), 213–223. https://doi.org/10.14356/kona.2017007

Pezo, M., Pezo, L., Lončar, B., Kojić, P., & Jovanović, A. A. (2025). A Comprehensive Review of Discrete Element Method Studies of Granular Flow in Static Mixers. *Processes*, *13*(11), 3522. https://doi.org/10.3390/pr13113522

Powell, M. S., & McBride, A. T. (2004). A three-dimensional analysis of media motion and grinding regions in mills. *Minerals Engineering*, *17*(11–12), 1099–1109. https://doi.org/10.1016/j.mineng.2004.06.022

Pural, Y. E., & Boylu, F. (2025). Prediction and visualization of charge shape and ball trajectory in tumbling mills: a python-based tool for liner design and operational optimizations. *Physicochemical Problems of Mineral Processing*, *61*(3). https://doi.org/10.37190/ppmp/204533

Radziszewski, P., & Tarasiewiczb, S. (1993). Modelling and simulation of ball mill wear. In *Wear* (Vol. 160).

Rajamani, R. K., Mishra, B. K., Venugopal, R., & Datta, A. (2000). Discrete element analysis of tumbling mills. *Powder Technology*, *109*(1–3), 105–112. https://doi.org/10.1016/S0032-5910(99)00230-2

Republic of Kenya. (2007). *Kenya Vision 2030: A globally competitive and prosperous Kenya.* (Issue October). https://vision2030.go.ke/wp-content/uploads/2018/05/Vision-2030-Popular-Version.pdf

Republic of Kenya. (2022a). *National Action Plan for Artisanal and Small-Scale Gold Mining in Kenya*.

Republic of Kenya. (2022b). *National Action Plan for Artisanal and Small-Scale Gold Mining in Kenya in accordance with the Minamata Convention on Mercury*. https://minamataconvention.org/sites/default/files/documents/national_action_plan/Kenya-ASGM-NAP-2022-EN.pdf

Roufail, R. A. (2011). *The effect of stirred mill operation on particles breakage mechanism and their morphologyical features*. *October*, 266.

Rumpf, H. (1973). Physical aspects of comminution and new formulation of a law of comminution. *Powder Technology*, *7*(3), 145–159. https://doi.org/10.1016/0032-5910(73)80021-X

Semsari, P., Parian, M., & Rosenkranz, J. (2020). Breakage process of mineral processing comminution machines – An approach to liberation. *Advanced Powder Technology*, *31*(9), 3669–3685. https://doi.org/10.1016/j.apt.2020.08.005

Shabana, N. (2010). *CEMENT INDUSTRY - Cement Mill Notebook*.

Shackleton, R. M. (1946). *Geology of the Migori Gold belt and the adjoining areas* (Issue 10). https://s3-eu-west-1.amazonaws.com/samsamwater1/maps/kenya/geology/Geology+of+the+Migori+Gold+Belt.pdf

Sogani, V., Somani, P., Singla, N., & Mathur, R. (2016). Population Balance in Ball Mill. *International Journal of Innovative Research in Technology*, *3*(2), 2349–6002. http://ijirt.org/master/publishedpaper/IJIRT143844_PAPER.pdf

Tavares, L. M. (2022). Review and Further Validation of a Practical Single-Particle Breakage Model. *KONA Powder and Particle Journal*, *39*(0), 62–83. https://doi.org/10.14356/kona.2022012

Tavares, L. M., & de Carvalho, R. M. (2009). Modeling breakage rates of coarse particles in ball mills. *Minerals Engineering*, *22*(7–8), 650–659. https://doi.org/10.1016/j.mineng.2009.03.015

Toledo M., P., Moncada M., M., Ruiz S., C., Betancourt C., F., Rodríguez, C. G., & Vicuña, C. (2025). A review of the application of the discrete element method in comminution circuits. *Powder Technology*, *459*, 121027. https://doi.org/10.1016/j.powtec.2025.121027

Tolomeo, M., & McDowell, G. R. (2022). Modelling real particle shape in DEM: a comparison of two methods with application to railway ballast. *International Journal of Rock Mechanics and Mining Sciences*, *159*, 105221. https://doi.org/10.1016/j.ijrmms.2022.105221

Tomach, P. (2024). The Influence of the Grinding Media Diameter on Grinding Efficiency in a Vibratory Ball Mill. *Materials*, *17*(12). https://doi.org/10.3390/ma17122924

Toor, P., Franke, J., Powell, M., Bird, M., & Waters, T. (2013). Designing liners for performance not life. *Minerals Engineering*, *43–44*, 22–28. https://doi.org/10.1016/j.mineng.2012.07.004

Vasilyeva, N., Golyshevskaia, U., & Sniatkova, A. (2023). Modeling and Improving the Efficiency of Crushing Equipment. *Symmetry*, *15*(7). https://doi.org/10.3390/sym15071343

Wang, L. G., Chen, J.-F., & Ooi, J. Y. (2021). A breakage model for particulate solids under impact loading. *Powder Technology*, *394*, 669–684. https://doi.org/10.1016/j.powtec.2021.08.056

Wills, B. A., & Finch, J. A. (2016). Grinding Mills. In *Wills' Mineral Processing Technology* (pp. 147–179). Elsevier. https://doi.org/10.1016/B978-0-08-097053-0.00007-8

Xiao'Ou, X. (2024). Crushing Equipment. In *The ECPH Encyclopedia of Mining and Metallurgy* (pp. 412–412). Springer Nature Singapore. https://doi.org/10.1007/978-981-99-2086-0_501

Yin, Z., Jin, Z., & Li, T. (2024). Research on an Accurate Simulation Modeling and Charge Motion Quantitative Evaluation Method for Ball Mill in Confined Space. *Minerals*, *14*(6). https://doi.org/10.3390/min14060604

Yin, Z., Li, T., Peng, Y., & Wu, G. (2018). Effect of Lifter Shapes on the Mill Power in a Ball Mill. *IOP Conference Series: Materials Science and Engineering*, *452*(4). https://doi.org/10.1088/1757-899X/452/4/042201

Yin, Z., Ma, D., & Li, T. (2024). Effect of Grinding Media Grading on Liner Wear and Load Behavior in a Ball Mill by Using Rocky DEM. *Lubricants*, *12*(10). https://doi.org/10.3390/lubricants12100340

Yu, J., Wei, H., Li, P., Han, Y., & Gao, P. (2025). *An Optimization Method for Accurate Ball Loading In Ball Mills Based on Grinding Kinetics*. https://doi.org/10.2139/ssrn.5154485

Yuan, C., Wu, C., Fang, X., Liao, N., Tong, J., & Li, Y. (2023). A New Approach to the Grinding Kinetics of Magnetite Ore Based on the Population Balance Model. *Minerals*, *13*(3). https://doi.org/10.3390/min13030424

Zhang, J., Qu, T., Yan, B., Zhao, C., Bian, Q., Zhao, Z., & Tang, B. (2023). Parameter influence analysis of ball mill based on DEM. *U.P.B. Sci. Bull., Series D*, *85*(1), 15–26.

APPENDICES

Appendix I: Main Dimensions of the Test Rig

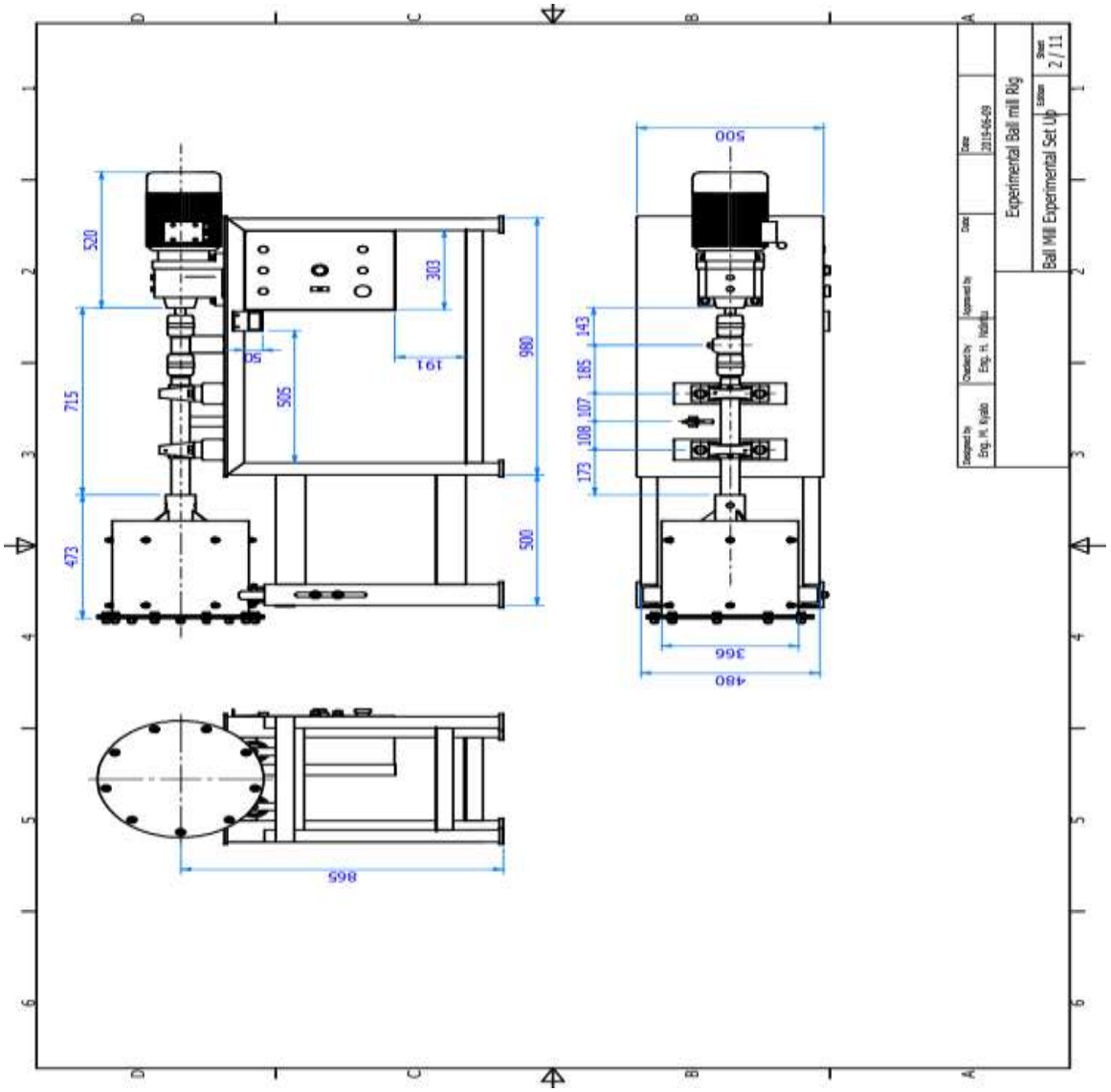

Appendix II: Details of the Mill Drum

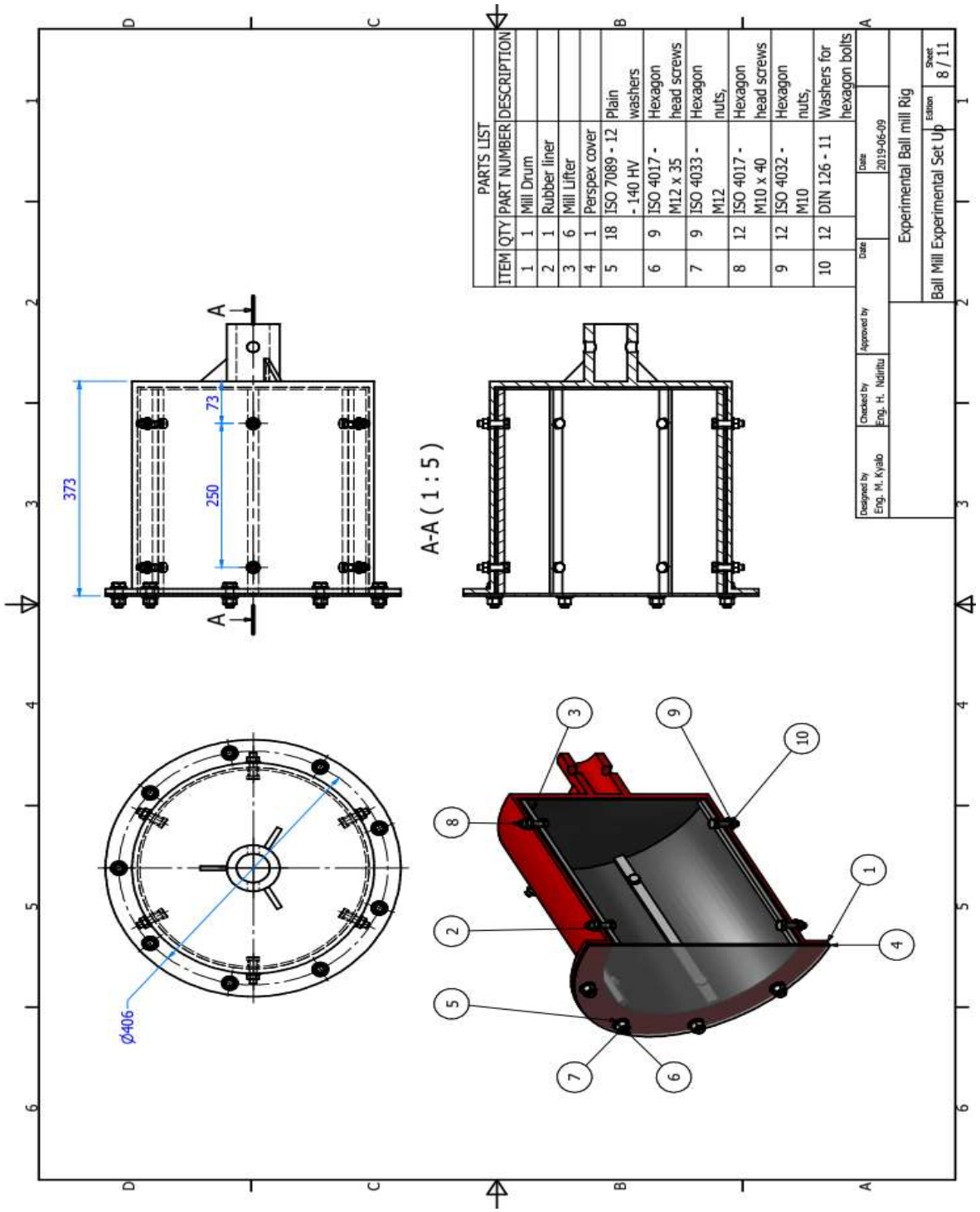

Appendix III: Jaw Crusher at Match Electricals Used for Size Reduction

Appendix IV: DOE for Calibration

Screening DOE 1

Std Order	Run Order	Pt Type	Blocks	CORp-p	COSFp-p	CORFp-p	CORp-w	COSFp-w	CORFp-w	Power (KW)
1	1	2	1	0.6	0.60	0.200	0.5	0.80	0.3	212.76
2	2	2	1	0.6	0.30	0.050	0.3	0.50	0.1	173.13
3	3	2	1	0.8	0.45	0.200	0.3	0.50	0.3	210.88
4	4	2	1	0.4	0.45	0.050	0.5	0.80	0.1	172.83
5	5	2	1	0.8	0.60	0.125	0.5	0.50	0.1	201.00
6	6	2	1	0.4	0.30	0.125	0.3	0.80	0.3	210.92
7	7	2	1	0.8	0.30	0.200	0.4	0.80	0.1	213.94
8	8	2	1	0.4	0.60	0.050	0.4	0.50	0.3	200.52
9	9	2	1	0.8	0.30	0.050	0.5	0.65	0.3	193.68
10	10	2	1	0.4	0.60	0.200	0.3	0.65	0.1	215.86
11	11	2	1	0.8	0.60	0.050	0.3	0.80	0.2	194.71
12	12	2	1	0.4	0.30	0.200	0.5	0.50	0.2	216.35
13	13	0	1	0.6	0.45	0.125	0.4	0.65	0.2	211.20

Surface Response DOE 2

Run	$\mu_{r,p-p}$	$\mu_{r,p-w}$	Power (Kw)	Shoulder angle (^{0})	Toe angle (^{0})
1	0.0275000	0.055000	161.74	158.4	302.1
2	0.0275000	0.055000	159.59	157.7	300.0
3	0.0050000	0.055000	153.09	160.4	302.7
4	0.0434099	0.086820	173.56	156.7	298.6
5	0.0434099	0.023180	158.02	161.0	297.6
6	0.0275000	0.055000	161.29	160.2	300.2
7	0.0115901	0.023180	149.20	161.1	302.1
8	0.0275000	0.055000	160.69	156.5	301.4
9	0.0115901	0.086820	162.09	158.8	302.8
10	0.0500000	0.055000	166.34	151.4	301.5
11	0.0275000	0.100000	170.66	157.0	301.8
12	0.0275000	0.055000	160.88	160.7	301.1
13	0.0275000	0.010000	152.09	160.5	300.5

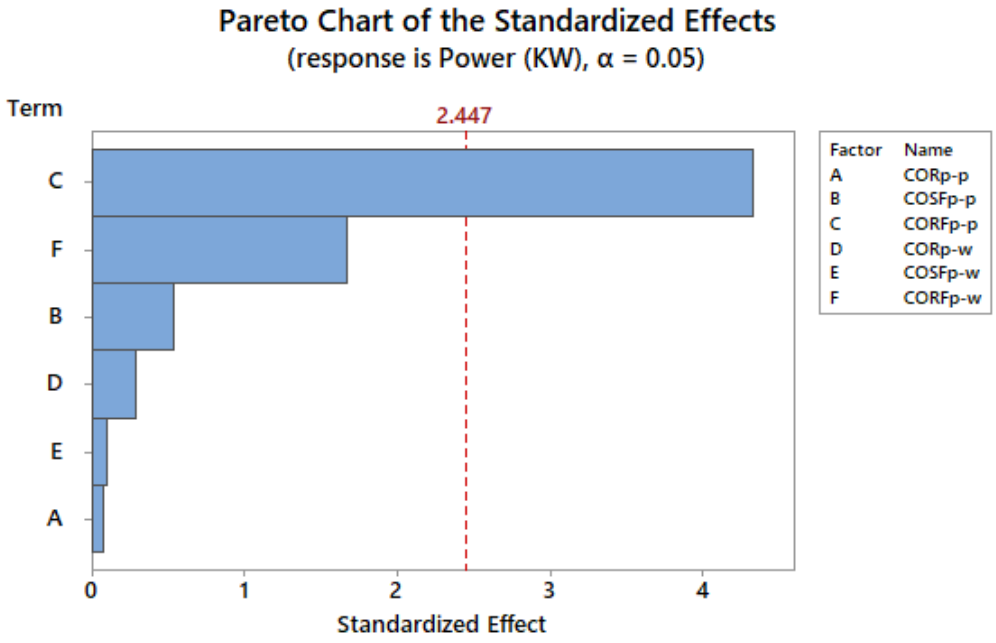

Analysis of Variance

Source	DF	Adj SS	Adj MS	F-Value	P-Value
Model	6	2128.88	354.81	3.67	0.069
Linear	6	2128.88	354.81	3.67	0.069
CORp-p	1	0.51	0.51	0.01	0.944
COSFp-p	1	28.31	28.31	0.29	0.608
CORFp-p	1	1820.73	1820.73	18.82	0.005
CORp-w	1	7.86	7.86	0.08	0.785
COSFp-w	1	1.07	1.07	0.01	0.920
CORFp-w	1	270.40	270.40	2.79	0.146
Error	6	580.62	96.77		
Total	12	2709.49			

Pearson's correlations

Pearson correlation r measures **linear agreement** between DEM and experimental results:

$$r = \frac{\sum_{i=1}^{n}(x_i - \bar{x})(y_i - \bar{y})}{\sqrt{\sum_{i=1}^{n}(x_i - \bar{x})^2}\,\sqrt{\sum_{i=1}^{n}(y_i - \bar{y})^2}}$$

- x_i = DEM prediction for a given operating condition
- y_i = Experimental measurement for the same condition
- n = number of experimental conditions tested

Appendix V: Cross-Sectional Area of Mill Profiles

Profile	Parameter	Value (mm)	Angle	
Hexagonal	Side length (a)	183.63923	60°	$\frac{3\sqrt{3}}{2} \times s^2$
Octagonal	Side length (a)	134.70650	45°	$2\left(1+\sqrt{2}\right)a^2$
Dodecagon 12-sided Polygon	Side length (a)	88.46205	30°	$A = 3\cot\left(\frac{\pi}{12}\right)a^2 = 3\left(2+\sqrt{3}\right)a^2 \simeq 11.19615242\,a^2$
16-sided hexadecagon	Side length (a)	66.00735	22.5°	$4t^2\left(1+\sqrt{2}+\sqrt{4+2\sqrt{2}}\right)$
Cylindrical	Radius (r)	167	0°	$A = \pi r^2$

Appendix VI: Conversions of Critical Speed to RPM and Frequency

Critical speed	55%	65%	70%	75%	80%	85%	90%	95%	100 %	105 %	115 %
Revs per min	40.25	47.57	51.23	54.89	58.55	62.21	65.87	65.53	73.19	76.85	84.16
rad/s	4.21	4.98	5.36	5.75	6.13	6.51	6.80	7.28	7.66	7.98	
Freq (Hz)		16		18.4		20.8		23.3			

Appendix VII: Sample Optimization Plot for Composite Desirability